MST RADAR TECHNIQUE FOR REMOTE SENSING OF THE MIDDLE ATMOSPHERE

BY

KOICHIRO WAKASUGI

MAY, 1981

KYOTO INSTITUTE OF TECHNOLOGY

KYOTO, JAPAN

MST RADAR TECHNIQUE FOR REMOTE SENSING OF THE MIDDLE ATMOSPHERE

BY

KOICHIRO WAKASUGI

MAY, 1981

KYOTO INSTITUTE OF TECHNOLOGY

KYOTO, JAPAN

ACKNOWLEDGMENTS

The author would like to acknowledge gratefully the guidance and support of Professor Susumu Kato throughout the present work.

Many constructive comments by Professors Masaru Matsuo and Hisanao Ogura of Kyoto Institute of Technology, and by Professors Iwane Kimura and Toru Ogawa are gratefully acknowledged.

The author is deeply indebted to Dr. Shoichiro Fukao for stimulating discussions and encouragements throughout the author's research career.

He also appreciates Dr. Takehiko Aso and Messrs. Toshitaka Tsuda, Toru Sato and Ken-ichi Aoki for interesting suggestions.

Acknowledgement is due to Professor William E. Gordon of Rice University and Dr. Alberto A. Giesecke, Director General of Geophysical Institute of Peru for their helpful supports of radar observations at Jicamarca, Peru.

Thanks are due to Messrs. Naoki Okamura and Shujiro Suzuki for helping the numerical calculations, which were performed at the Data Processing Center of Kyoto University.

ABSTRACT

An intense study of the middle atmosphere (10-100 km) has been required for understanding the long-term climatic changes which might affect our life environments. This work concerns the MST (Mesosphere-Stratosphere-Troposphere) radar technique which is relevant to the remote-sensing of the middle atmosphere with high-power sensitive radars.

MST radar signal processing is discussed. Backscattered signals from weak refractive index fluctuations in the middle atmosphsre are formulated with the radar ambiguity function which provides a consistent description of radar resolution properties. A multiple compressed-pulse method is studied and the relation between time and range resolutions is established. Beside analyzing the echo power spectra from anisotropic fluctuations, parameter estimation and errors are also discussed.

In order to investigate radio-wave scattering mechanisms and atmopheric oscillation properties in the middle atmosphere, radar observations are performed at Jicamarca, Peru (12.0°S, 76.9°W). Depolarization of radar echoes measured suggests strong echoes originating in stable atmospheric structures. The dominant short-period atmospheric waves observed are largely buoyancy or Brunt-Väisälä oscillations. Tidal oscillations with diurnal and semidiurnal periods are also observed.

TABLE OF CONTENTS

LIST OF FIGURES

Chapter 1.

GENERAL INTRODUCTION

An intense study of the middle atmosphere (10-100 km) has been required, since it seems to play an important role for understanding long-term climatic changes. A wide range of measurements in both time and space are needed to investigate the middle atmosphere but it is yet very difficult to probe this region. For this reason, the Middle Atmosphere Project (MAP), an internationally coordinated study, is scheduled between 1982 and 1985. MST (Mesosphere, Stratosphere and Troposphere) radar technique involves remote-sensing of the middle atmosphere with high-power sensitive Doppler radars. Radar echoes provide information on the dymanic properties of the atmosphere.

In this chapter, some properties of the middle atmosphere are surveyed first. The MST radar systems and some observational results are also discussed.

1.1 MIDDLE ATMOSPHERE

The middle atmosphere is defined as the region between the tropopause and 100 km. This region consists of the stratosphere

(10-50 km), the mesosphere (50-80 km) and the lower part of the thermosphere (80-100 km).

The solar radiation is the main energy source of the earth's atmosphere and only small part of this radiation is absorbed directly by water vapor, carbon dioxide and ozone within the middle atmosphere. This part of the solar energy, however, contributes most to the generation of atmospheric tidal waves. The greater part of the solar radiation is absorbed by the earth's surface which, in turn, reradiates the solar energy in the infrared acting as a secondary heat source for the lower atmosphere.

Figure 1.1 shows the temperature structure of the earth's atmosphere. The temperature falls with increasing height due to the adiabatic expansion of the convecting atmosphere in the troposphere. In the stratosphere the temperature increases due to the radiative heating by ozone and becomes maximum at about 50 km. The variation of temperature with height is due to the heat balance between ultraviolet absorption of ozone and infrared radiation from water vapor, carbon dioxide and ozone. In the mesosphere the temperature is determined by the balance between radiative heating due to molecular oxyzen and infrared radiative cooling due to carbon dioxide. The temperature minimum appears at about 80 km where there is little absorption of solar radiation. The solar ultraviolet radiation is strongly absorbed by molecular

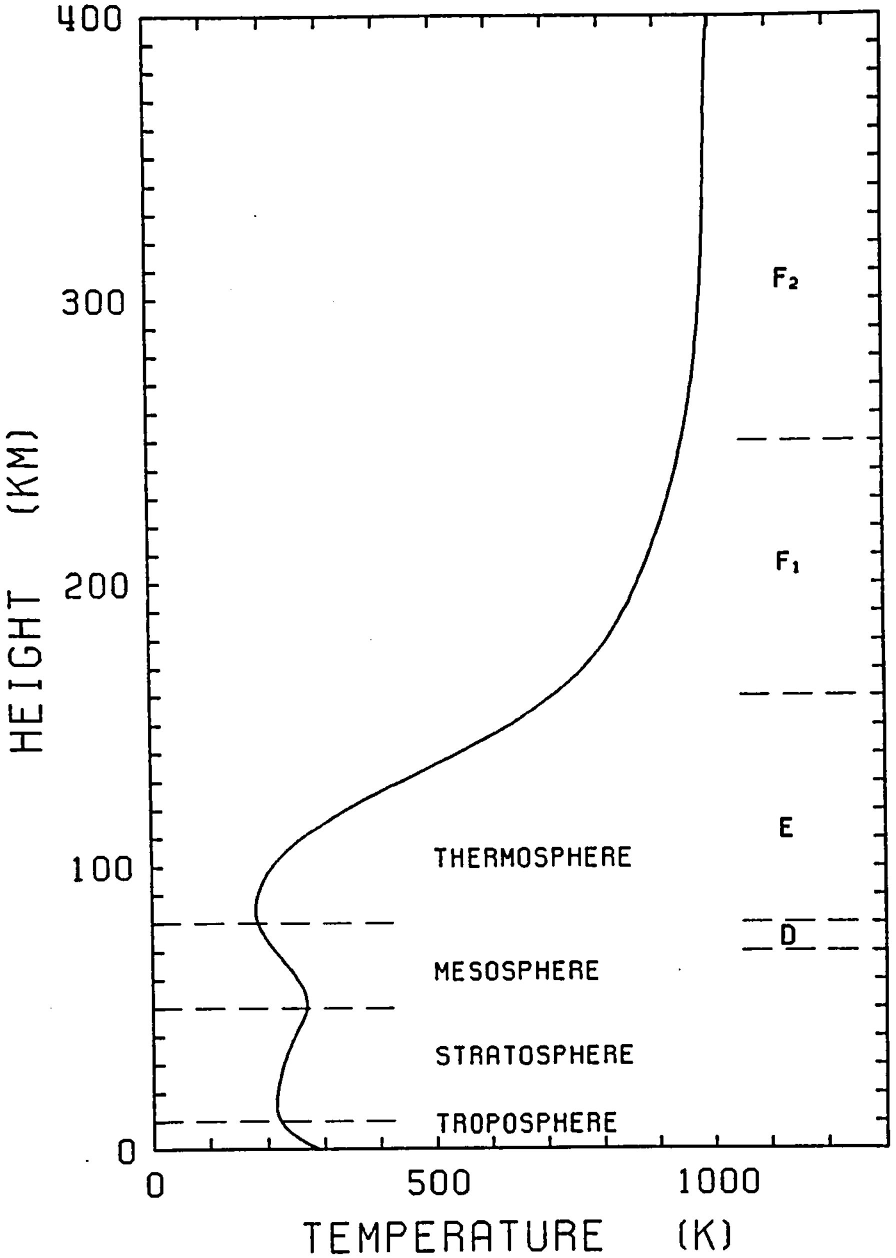

Figure 1.1. Temperature distribution of the earth's atmosphere (U.S. Standard Atmosphere, 1966).

and atomic oxyzen and the temperature rises in the lower thermosphere.

The hydrodynamic and thermodynamic equations determine the atmospheric properties. They are the momentum equation, continuity equation, energy equation and gas equation (e.g., Kato, 1980).

$$D\vec{W}/Dt + 2(\vec{\Omega}x\vec{W}) = -\nabla p/\rho + \vec{g} + \vec{j}x\vec{B}/\rho + \vec{F} \qquad (1.1)$$

$$D\rho/Dt + \rho\nabla\cdot\vec{W} = 0 \qquad (1.2)$$

$$Dp/Dt - C^2 D\rho/Dt = (\kappa-1)Q\rho \qquad (1.3)$$

$$p = \rho RT \qquad (1.4)$$

where $D/Dt=\partial/\partial t+(\vec{W}\cdot\nabla)$, $\vec{W}$ is the velocity vector of the neutral air, $\vec{\Omega}$ the earth's angular velocity, p the pressure, ρ the density, $\vec{g}$ the apparent acceleration of the earth's gravity, $\vec{j}$ the electric current density, $\vec{B}$ the geomagnetic field, $\vec{F}$ the frictional force per unit mass, κ=Cp/Cv (Cp and Cv are the specific heats at constant pressure and volume, respectively), Q the net heating per unit mass, T the temperature, R the gass constant. C is the sound speed and it is related by the expression $C^2=\kappa RT$.

These equations are nonlinear, and are related to each other in a complicated manner. Though there are solutions in elementary functions for a few cases, huge computer simulations are playing an important role to solve more realistic problems. A simplified solution, however, has the advantage of providing a physical insight of the problem. States of the earth's atmosphere can be expressed by the averaged state and the superposed deviation. The corresponding equations for small perturbations are linear, resulting in various types of atmospheric waves (Kato, 1980; Gossard and Hooke, 1975).

The average state of the atmosphere is safely approximated to be static, thus (1.1) reduces to

$$d\rho^0/dz = -\rho^0 g \tag{1.5}$$

where superscript $(^0)$ denotes static part. With the equation of state $p^0=\rho^0 RT^0$, (1.5) can be integrated as

$$p^0 = p^0(0)\ \exp[-\int dz/H] \tag{1.6}$$

where $H=RT^0/g$ is known as the scale height.

The atmosphere in hydrostatic equilibrium is, in general, inhomogeneous in the vertical direction. The stability of the equilibrium can be examined by considering a small displacement from the equilibrium. The air parcel experiences the buoyancy force when it is displaced downwards. If the external force is removed, the parcel will oscillate with an angular frequency Nb (e.g., Yeh and Liu, 1974) which is expressed as

$$Nb^2 = (\kappa-1)g^2/C^2 + (g/C^2)dC^2/dz \qquad (1.7)$$

The characteristic frequency Nb is called the buoyancy or Brunt-Väisälä frequency. There is a situatuion, however, when Nb^2 given in (1.7) is negative. As the initial perturbation will grow exponentially with time, the atmosphere is unstable. The critical condition $Nb^2=0$ corresponds to $-dT^0/dz=g(\kappa-1)/(\kappa R)$. The atmosphere is stable if the gradient of the temperature is smaller than the adiabatic lapse rate $g(\kappa-1)/(\kappa R)$.

1.2 RADAR EQUATIONS AND SCATTERING MECHANISMS

VHF and UHF radars have been used to detect weak echoes backscattered from refractive index fluctuations of the atmosphere. The fundamental tool of radar system design is the radar equation which relates the received power to the parameters of a particular radar system. The radar cross section is a measure to describe the size of radar targets. For MST measurements, it is related to the volume reflectivity η, or reflection coefficient $|\rho|$, dependent on the particular atmospheric process concerned.

Probert-Jones (1962) first derived the classical radar equation for scattering from distributed targets with dish antennas. The received power Pr can be expressed in a generalized form

$$Pr = Pt\ Ae\ \Delta h\ \eta/(9\pi r^2) \qquad (1.8)$$

where Pt is the peak transmitter power, Ae the effective antenna aperture, Δh the range resolution, r the range and η the volume reflectivity. For radars with array antenna, Ae should be replaced by Ae$\cdot\cos\psi$ where ψ is the zenith angle (VanZandt et al., 1978).

For Fresnel reflection by a horizontal layer extended over a Fresnel zone, Friend (1949) derived the radar equation as follows;

$$Pr = Pt\ Ae^2\ |\rho|^2/(4\lambda^2 r^2) \qquad (1.9)$$

where $|\rho|^2$ is the power reflection coefficient and λ is the radar wavelength.

Radar echoes originate from scattering or reflection caused by atmospheric inhomogeneities which are expressed macroscopically by the index of refraction n. n-1 is called as the radio index of refraction and is given by

$$n-1 = 3.73\times10^{-1}e/T^2$$

$$+\ 77.6\times10^{-6}p/T - Ne/2Nc \quad (1.10)$$

where p is the atmospheric pressure, e the partial pressure of water vapor, T the temperature, Ne the number density of electrons and Nc the critical plasma density (Balsley and Gage, 1980). The first term is important in the troposphere because of high humidity. The second term dominates in the stratosphere. Since the electron density increases rapidly with altitude, the third term becomes dominant above 50 km.

Thermal scatter, turbulent scatter and Fresnel reflection are the fundamental echoing mechanisms to interpret the signals observed by MST radars.

For thermal scatter, fluctuations of the refractive index are caused by the thermal motion of electrons under the influence of ions. The volume reflectivity is approximated to (e.g., Evans, 1969,1974)

$$\eta_{thermal} = Ne\ \sigma e/2 \qquad (1.11)$$

where σe is the cross-section of an electron. With (1.8), the altitude profile of electron density can be derived by the received power at each altitude. Furthermore ion and/or electron temperatures and ion composition at a certain pertinant altitude can be estimated by comparing the echo power spectrum with spectrum based on the theoretical calculations (e.g., Dougherty and Farley, 1960). Thus thermal scatter is useful for exploring the ionized region of the atmosphere.

The refractive index of the atmosphere fluctuate with random motions of turbulent flow. Turbulent scattered signals thus provide information about the turbulence structures and background mean flow. Turbulence is characterized by several parameters; the eddy diffusion rate ε_d, the outer scale Lo and inner scale $\ell o = (\nu^3/\varepsilon_d)^{1/4}$, where ν is the kinematic viscosity (Monin and Yaglom, 1971; Tennekes and Lumley, 1972). Radio wave is backscattered by fluctuations whose length scale is equal to one-half the radar wavelength (Tatarskii, 1971). If the condition $\ell o < \lambda/2 < Lo$ is satisfied, the radar wavelength λ is in the inertial subrange of the turbulence spectrum. This is a necessary condition for turbulent scatter measurements. The volume reflectivity of turbulent scatter is given by (Tatarskii, 1971),

$$\eta_{turb.} = (\pi^2/2) K_B{}^4 \Phi_3 (K_B) \qquad (1.12)$$

where K_B is the Bragg wavenumber (=2k, k is the radar wavenumber) and Φ_3 is the three-dimensional spectral density of refractive index fluctuations. If the turbulence is assumed to be locally homogeneous and isotropic and the radar wavelength is in the inertial subrange, the volume refrectivity is directly related to the radar wavelength λ as follows (Tatarskii, 1971);

$$\eta_{turb.} = 0.38\ Cn^2\ \lambda^{-1/3} \qquad (1.13)$$

where Cn^2 is the refractive index structure parameter. Cn^2 is the fundamental parameter of turbulence (e.g., Crane, 1980).

Fresnel reflection has been originally studied through the partial reflection in the ionosphere (Belrose, 1970). The power reflection coefficient $|\rho|^2$ of an infinite layer is given by

$$|\rho|^2 = (1/4)\left|\int_{-\ell/2}^{+\ell/2} dn/dz\ \exp[-4\pi jz/\lambda]dz\right|^2 \quad (1.14)$$

where ℓ is the thickness of the layer. Discontinuities of refractive index with altitude cause the radio wave reflections. For a rectangular layer with weak fluctuations, significant Fresnel reflections occur even if the thickness is of many wavelengths (Valley, 1975). Recent observational results with VHF radars also suggest the importance of Fresnel reflections in the middle atmosphere (e.g., Harper and Gordon, 1980).

A measure of radar system sensitivity is the average power-aperture product which is defined as the average transmitter power capability multiplied by the effective antenna area. In order to detect weak echoes, the requisite average power-aperture product for MST radars is suggested to be at least 10^9 Wm^2 (Balsley and Gage, 1980). Another important requirement is that the radar wavelength, which determines the scattering scale size, must be within the inertial subrange of turbulence at all altitudes. This limits the operating frequency of an MST radar to values below at least 100 MHz, preferably below 50 MHz (Balsley and Gage, 1980). Radars operating at higher frequencies or having smaller average power-aperture products have been termed ST(Stratosphere-Troposphere) radars.

1.3 OBSERVATION BY MST RADARS

Since the pioneering work of Woodman and Guillén (1974) demonstrated the capability of MST radar probing, enormous progress has been made in the middle atmosphere observation. Many of the recent developments have been thoroughly reviewed by Harper and Gordon (1980). Some observational results, which are closely related to the observation to be represented in Chapter 4, are discussed in this section.

A. Scattering properties

Hydrostatic stability is important for determining the dynamics of the atmosphere. A stable atmospheric region suppresses the vertical motion and permits the development of large vertical gradients of wind (e.g., Gossard and Hooke, 1975). If the atmosphere is stable and forms layers, the Fresnel reflection is considered to dominate over the turbulence scatter. Echo properties are closely related to the atmospheric stability. A comparison of the vertical and oblique power profiles gives a clue of the atmospheric stability. With the Sunset radar (40.5 MHz) at Boulder, Colorado, Gage and Green (1978) reported that the signal received on the vertical antenna is enhanced compared to that of the antennas pointed 30 degrees off the zenith. They further showed the correlation between the vertical power profiles and the vertical profiles of the potential temperature gradient and attributed the sharp increase in echo power to partial specular reflection from stable atmospheric layers. Similar observations have been made using the SOUSY radar (53.5 MHz) in West Germany (Röttger and Liu, 1978).

Strong echoes should have long correlation times if they are due to stable atmospheric structures. Fukao et al. (1980b) showed that the correlation coefficient between the echo power and the signal correlation time reversed its sign from positive to negative at an altitude around 75 km. This altitude just coincides with the altitude below where a marked aspect sensitivity of the scattering is noticed.

Vincent and Röttger (1980) used radar interferometric techniques to investigate the angular spectrum of reflecting/scattering structures. Measurements of the angular width and spatial coherence showed the reflecting regions to be thin and quasi-horizontal in structure.

These observational results strongly suggest the existence of Fresnel or specular type reflection and provide information for studying atmospheric stability in the middle atmosphere.

B. Short-period oscillation

The major advantage of the MST radar technique over other technique lies in the continuous procurement of the data in both time and altitude. This property is ideal for observing stratospheric waves whose periods range from seconds to years.

Internal gravity waves of a few minutes period have been observed by the Jicamarca radar (Rüster _et al._, 1978) and by the Sunset radar (VanZandt _et al._, 1979). Rüster and Klostermeyer (1980) presented the short-period gravity waves observed during a jet stream passage and concluded that shear instability was the source of the waves.

Generation and propagation of short-period oscillations should be closely related to the pertinent atmospheric structures which, in turn, characterize pertinent echo properties. Czechowsky _et al._ (1979) observed descending scattering regions in the mesosphere and suggested the posibility that gravity waves are creating turbulence. However, a strong correlation between the velocity oscillation and the echo power has not been observed, while it is expected if a wave were breaking into turbulence.

Dynamic property of short-period oscillations and its relation to the scattered echoes have not been fully studied and much work has to be done by MST radar measurements.

C. Atmospheric tides

Evans (1978) has reviewed the radar observation of the lower thermosphere. In this region, the fundamental propagating diurnal mode is regularly observed and it agrees with the theoretical predictions (e.g., Kato, 1980).

This diurnal tide, however, has not yet fully been understood below 80 km. There is an evidence from rawinsonde data that the diurnal wind oscillation observed at the troposphere and stratosphere is not the wave number 1 tide predicted by classical tidal theory (Wallace and Tadd, 1974). They inferred that the oscillation was linked to local, regional or continental topography.

Fukao et al. (1978) analyzed a full day's stratospheric data obtained by the Jicamarca radar. Diurnal wind oscillations with an amplitude of several meters per second, downward phase progression and a wavelength less than 10 km were observed, similar to those inferred from the averaged rawinsonde data

(Wallace and Tadd, 1974). Similar results were obtained by using the Arecibo radar (430 MHz) at Puerto Rico (Fukao et al., 1981b).

Long-time measurements are desirable and the relation between the radar-inferred wind oscillation and the regional and/or meteorological variables should be developed in future MST radar measurements.

1.4 OBJECTIVES AND SCOPE OF THIS STUDY

The purpose of the present study concerns the remote-sensing of the middle atmosphere by radar technique.

In order to extract atmospheric information from the radar echoes, typical analysis procedures involve obtaining the echo power spectrum or the autocorrelation function. Accuracy and resolutions of the estimated parameters are very important and should be intensely studied. However, observation studies or atmospheric properties have been much emphasized and little attention has been focused on the signal processing.

Signal processing pertinent to the MST radar technique is discussed in Chapter 2. The Born approximation is the fundamental mathematical model for weak refractive index fluctuations. On this approximation, backscattered signals are formulated with the radar ambiguity function in Section 2.2. In order to attain a better range resolution, phase-coding pulse compression technique by Barker and complementary codes are also discussed. In Section 2.3, the resolution properties of thermal scatter observations is discussed and the performance of the multiple compressed-pulse method is estimated. Section 2.4 concerns parameter estimation for turbulent scatter observation. Widely-used periodogram is related to a four-dimensional spectral density of fluctuations with anisotropic structure. This treatment is intended to give another explanation of the aspect sensitivity which has been observed by MST radars.

Chapter 3 is devoted to the discussion of the observational results using the Jicamarca VHF radar in Peru. Results of practical radar signal processing are demonstrated. The objectives of the observations are to investigate the scattering mechanisms, short-period atmospheric oscillations and tidal waves. Section 3.2 surveys the Jicamarca radar facility to show the capability and limitation of the observation. Frequency and polarization of radar waves are the fundamental variables which characterize the radar echoes. First measurement of the polarization properties of MST radar echoes is presented in Section 3.3. In Section 3.4, an observation of short-period atmospheric oscillation is discussed. As atmospheric structures are closely related to the echo power and correlation time, the relation between the short-period oscillations and the scattering properties is also presented. In Section 3.5, two sets of

48-hours continuous observation of the tropical stratospheric heights are analyzed in order to infer properties of long-period atmospheric waves and mean winds.

In Chapter 4, we summarize the results of the present work .

Chapter 2.

RADAR SIGNAL PROCESSING FOR MIDDLE ATMOSPHERE OBSERVATION

2.1 INTRODUCTION

The MST radar technique involves radar backscattering from atmospheric fluctuations. The echo power spectrum or auto-correlation function is generally estimated in order to extract information from radar signals. These estimates provide information about the atmospheric motions and constituents. The way of signal processing is dependent on the characteristics of pertinent fluctuations.

In this chapter, we concern some of the procedures involved in the signal processing for middle atmosphere observations. In Section 2.2, the backscattered signal from weak fluctuations is formulated. Section 2.3 and 2.4 describe signal processings in thermal and turbulent scatter, respectively.

2.2 GENERAL FORMULATION

As a complete theory for electromagnetic propagation in turbulent media is not available, appropriate models which can be applied under restrictive conditions have been proposed (e.g., Ishimaru, 1978; Fante, 1975,1980). The Born approximation is applicable to radiowave backscattering by atmospheric dielectric constant fluctuations (Booker and Gordon, 1950; Tatarskii, 1971; de Wolf, 1975).

In this section, the Born approximation is adopted. We formulate backscattered signals with the radar ambiguity function which provides a coherent aspect of radar resolution properties.

2.2.1 Backscattered signal

Spatial and/or temporal variations of dielectric constant, $\varepsilon(\vec{r},t)$, affect the propagation of electromagnetic waves. $\varepsilon(\vec{r},t)$ can be expressed as follows;

$$\varepsilon(\vec{r},t) = \langle\varepsilon(\vec{r},t)\rangle + \Delta\varepsilon(\vec{r},t) \qquad (2.1)$$

where the brackets denote an ensemble average (t: time). The changes in $\langle\varepsilon\rangle$ cause refraction effects. In the following, only the case where $\langle\varepsilon\rangle$=const. is considered. $\Delta\varepsilon$ is the fluctuation about the mean. Assuming the fluctuations are small enough as $\langle|\Delta\varepsilon|\rangle \ll \langle\varepsilon\rangle$, the Born approximation is applicable to the echo backscattered from those fluctuations. This backscattered echo $s(\vec{Ro},t)$ is given by

$$s(\vec{R}o,t) = k^2 \int E(\vec{R},t)\ \varepsilon(\vec{r},t)\ G(\vec{R})\ d\vec{r} \qquad (2.2)$$

where k is the radar wavenumber. $\vec{R}o$ is the position of radar transmitter-receiver systems from the origin and $\vec{R}$ a vector from the radar to a scattering region (i.e., $\vec{R} = \vec{R}o-\vec{r}$). Assuming that the fluctuations are located in the Fraunhofer region of the radar antenna, the incident wave $E(\vec{R},t)$ and the Green's function $G(\vec{R})$ are given respectively by

$$E(\vec{R},t) = Ag(\vec{R},\vec{n})u(t-2R/c)\exp[-jkR]/R \qquad (2.3)$$

$$G(\vec{R}) = g(\vec{R},\vec{n})\exp[-jkR]/4\pi R \qquad (2.4)$$

where A is a constant which is proportional to the radar sensitivity, g the antenna directivity centered about the boresight $\vec{n}$, u the complex envelope of transmitted waveforms, c the light speed and $R=|\vec{R}|$. G is the product of the free-space Green's function $\exp[-jkR]/4\pi R$ and the antenna directivity $g(\vec{R},\vec{n})$ to account for the preferential sensitivity of the receiving antenna.

The receiver output is given by the convolution of the backscatter echo $s(\vec{R}o,t)$ with the receiver impulse response v(t). Combining (2.2) - (2.4), we have the signal backscattered from weak dielectric fluctuations;

$$q(\vec{R}o,t) = A/4\pi \iint |g(\vec{R},\vec{n})|^2 \chi_{vu}^*(t-2R/c,\omega)h(\vec{r},t)$$

$$\cdot \exp j[\vec{K}\cdot\vec{r}+\omega t+2kR] /R^2 \ d\vec{r}d\varepsilon(\vec{K},\omega) \quad (2.5)$$

where $\chi(t,\omega)$ is the radar ambiguity function, whose properties are discussed in the next subsection (ω: angular frequency). The intensity scaling function $h(\vec{r},t)$ describes smooth variations of mean characteristics. $d\varepsilon(\vec{K},\omega)$ is the spectral representation of $\Delta\varepsilon(\vec{r},t)$;

$$\Delta\varepsilon(\vec{r},t) = h(\vec{r},t) \int \exp j[\vec{K}\cdot\vec{r}+\omega t] \ d\varepsilon(\vec{K},\omega) \quad (2.6)$$

If $d\varepsilon(\vec{K},\omega)$ is stationary in time and homogeneous in space, it satisfies the conditions;

$$\langle\varepsilon(\vec{K},\omega)\rangle = 0 \quad (2.7)$$

$$\langle d\varepsilon(\vec{K},\omega)d\varepsilon^*(\vec{K}',\omega')\rangle$$

$$= \delta(\vec{K}-\vec{K}')\delta(\omega-\omega')\Phi(\vec{K},\omega)d\vec{K}d\vec{K}'d\omega d\omega' \quad (2.8)$$

(2.7) can be readily obtained from the definition $\Delta\varepsilon(\vec{r},t)$

$=\varepsilon(\vec{r},t)-\langle\varepsilon(\vec{r},t)\rangle$. $\Phi(\vec{K},\omega) \geq 0$ is a four-dimensional (space-time) spectral density.

(2.5) is a general expression for backscattered signal by weak fluctuations. A microscopic difference of atmospheric constituents determines the fluctuation properties. Discussions on the microscopic properties are beyond our scope here. However these differences should be taken into consideration in processing radar signals. In the following sections, (2.5) is applied to thermal and turbulent scatter.

2.2.2 Radar ambiguity function

Pulse compression techniques have been used to improve range resolution and to increase effective peak power of radar systems. The ambiguity function describes the measurement precision and it is extremely useful in the design and study of radar signals (Cook and Bernfeld, 1967; Rihaczek, 1969). This function is defined as follows;

$$\chi_{uv}(t,\omega) = \int u(s)v^*(s+t)\exp[-j\omega s]\, ds \qquad (2.9)$$

By difinition, $\chi(t,0)$ represents the cross correlation of $u(t)$ and $v(t)$, and it corresponds to the range resolution for zero Doppler shift. Thus, $\chi(t,\omega)$ can be interpreted as the cross correlation between the Doppler-shifted transmit waveform and the receiver impulse response.

Straight integration of $|\chi(t,\omega)|^2$ yields the well-known volume constraint for ambiguity surfaces. This constraint is an expression of the uncertainty relation between time and frequency. Rihaczek (1965) gives the strict expressions of this constraint as follows;

$$\int |\chi(t,\omega)|^2 \, dt = \int |\chi(t,0)|^2 \exp[-j\omega t] dt \quad (2.10)$$

$$\int |\chi(t,\omega)|^2 \, d\omega = \int |\chi(0,\omega)|^2 \exp[-j\omega t] d\omega \quad (2.11)$$

(2.10) states that the volume distribution of the ambiguity function in the Doppler domain is completely determined by the value of the ambiguity function on the zero Doppler axis. (2.11) is the dual relation of (2.10). Thus an ideal radar waveform for all applications does not exist. The selection of a waveform is hence required for a given situation (Deley, 1970; Rihaczek, 1971).

Ioannidis and Farley (1972) first applied Barker phase-coded pulses to the incoherent scatter measurement for D- and E-region. A binary phase-coded pulse is easy to generate and has been used for middle atmosphere observations (Röttger _et al._, 1979; Fukao _et al._, 1981). A long pulse is subdivided into N subpulses, which are of equal time duration. The phase of each subpulse alternates between 0°and 180° in accordance with pertinent code.

By compressing the pulse, the range resolution is improved while range sidelobes generally appear. The pulse compression ratio γ, and the sidelobe suppression factor Γ are measures of compression. γ is defined as the ratio of the uncompressed pulse width to the compressed pulse width. For distributed targets as in the atmosphere, echoes are continuously received with respect to range. One should pay attention to the echo power from these range sidelobes. Assuming that targets are distributed uniformly with range, the sidelobe suppression factor Γ is defined as the ratio of the power from mainlobe to that from sidelobes.

Barker codes with elements N=2,3,4,5,7,11 and 13 have been found and it is unlikely that there are Barker codes with N>13 (Cook and Bernfeld, 1965). Thus, maximum values of γ and Γ are 13 and 14.1 (11.5 dB), respectively, for these Barker codes. Figure 2.1 shows a plot of $|\chi(t,\omega)|$ of the 13-element Barker code. Time and frequency are normalized by the subpulse duration and the reciprocal of the subpulse duration, respectively. For example, the frequency is normalized by 1 MHz, if a subpulse duration Tb is assumed to be 1 μs. Barker codes are optimum in the sence that the sidelobes for zero Doppler shift are uniform (22.3 dB below the mainlobe), i.e., $|\chi(t,0)| \leq 1/N$ for $|t| \geq Tb$ (N=13). These figures are fairly large for middle atmosphere observation, and technique in suppressing the sidelobes is needed. For example,

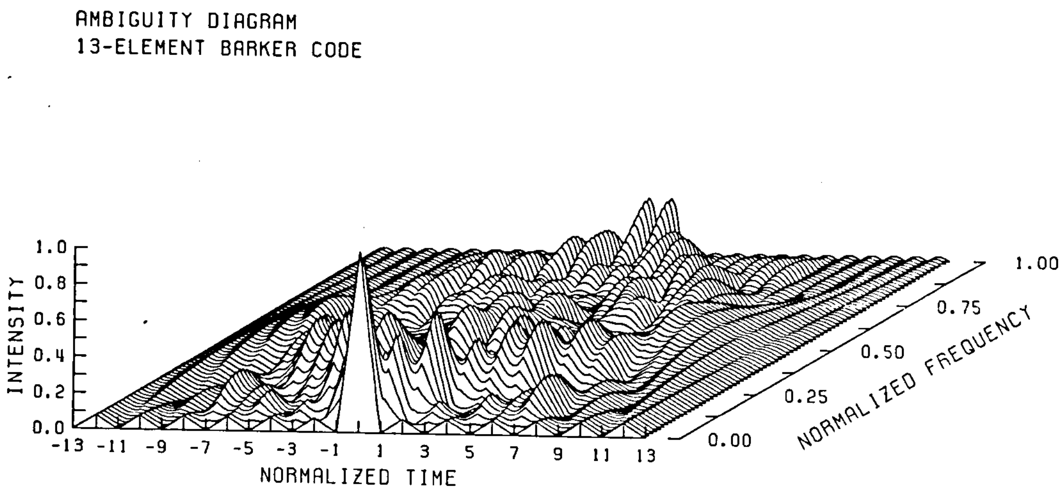

Figure 2.1. A plot of $|\chi(t,\omega)|$ of the 13-element Barker code. Time and frequency are normalized by the subpulse duration and the reciprocal of the subpulse duration, respectively.

Rihaczek and Golden (1971) designed a sidelobe suppression filter in digital form, and obtained the peak sidelobes of -43.8 dB.

For middle atmosphere observation, the spectral width in ω of fluctuations $d\varepsilon(K,\omega)$ is extremely narrower than that of radar waveforms $\chi(t,\omega)$. (2.7) suggests that a zero sidelobe waveform only around the zero Doppler axis is optimum for our application. These waveforms are realizable even under the restriction of volume invariance of (2.11).

A complementary code consists of a pair of two equal-lengh (even and odd) codes. It has the property that the sum of the autocorrelation functions of even and odd codes is zero everywhere except for the central peak (Golay, 1961). Complementary codes with elements $N=2^n$ (n=1,2,3,4,5....) are available.

For practical radar observations, two codes are sequentially transmitted with the interpulse period T, and decoded independently. The ambiguity function of the complementary code is readily obtained as follows;

$$\chi(t,\omega) = \chi_{even}(t,\omega)\exp[-j\omega T/2]$$

$$+ \chi_{odd}(t,\omega)\exp[j\omega T/2] \qquad (2.12)$$

where χ_{even} and χ_{odd} denote the ambiguity functions of even and odd codes, respectively. The cross terms of even and odd codes, which correspond to the second round-trip echoes, are neglected for deriving (2.12).

Because of complementary nature of even and odd codes, χ_{even} and χ_{odd} have the following properties;

$$\chi_{even}(t,0) = -\chi_{odd}(t,0) \quad \text{for } |t| \geq Tb \qquad (2.13)$$

$$\chi_{even}(t,\omega) = -\chi_{odd}(t,\omega) \quad \text{for } |t| \geq NTb/2 \quad (2.14)$$

where Tb is the subpulse duration. (2.13) means the sidelobes of one code are the negative of the other on the zero Doppler axis. Thus, no sidelobe appears and Γ tends to infinity (∞ dB), if a coherent summation of even and odd codes is possible.

Figure 2.2(a) shows a plot of $|\chi_{even}(t,\omega)|$ of the 16-element even code. Frequency is normalized by the reciprocal of subpulse duration, thus 0.06 in the figure corresponds to 60 kHz for the 1 μs subpulse duration. Peak sidelobes are only 10.1 dB below the mainlobe. The sidelobe suppression factor Γ is 5.4 dB (4.8 dB for odd code) for $\omega=0$, a value lower than that of the 13-element Barker code.

The ambiguity function of the complementary code changes as a function of the interpulse period T. For T = 0 (this is not a practical situation), χ in (2.12) is a mere summation of χ_{even} and χ_{odd}. (2.14) states $\chi(t,\omega)$ is absolutely zero for $|t| \geq NTb/2$ (N=16), as is shown in Figure 2.2(b).

Figure 2.2(c) shows a plot of $|\chi(t,\omega)|$ of the 16-element complementary code for IPP=50, where IPP is a normalized unit based on a subpulse duration (T=50 μs for the 1 μs subpulse duration). For finite IPP ($T \neq 0$), exponential terms in (2.12) rotate the phase of complex values $\chi_{even}(t,\omega)$ and $\chi_{odd}(t,\omega)$ for given values of t and ω. Thus the relative phase between the first and second terms varies as a function of ω (and, of course, T). The resultant $\chi(t,\omega)$ shows an oscillation with a frequency of $2\pi(2/T)$ in the Doppler frequency direction. Especially for $|t| \geq NTb/2$, the ambiguity function of complementary code turns out to be $2\chi_{even}(t,\omega)\sin(\omega T/2)$. Sidelobes for $\omega=n\pi/T$ (n=1,2,3...)

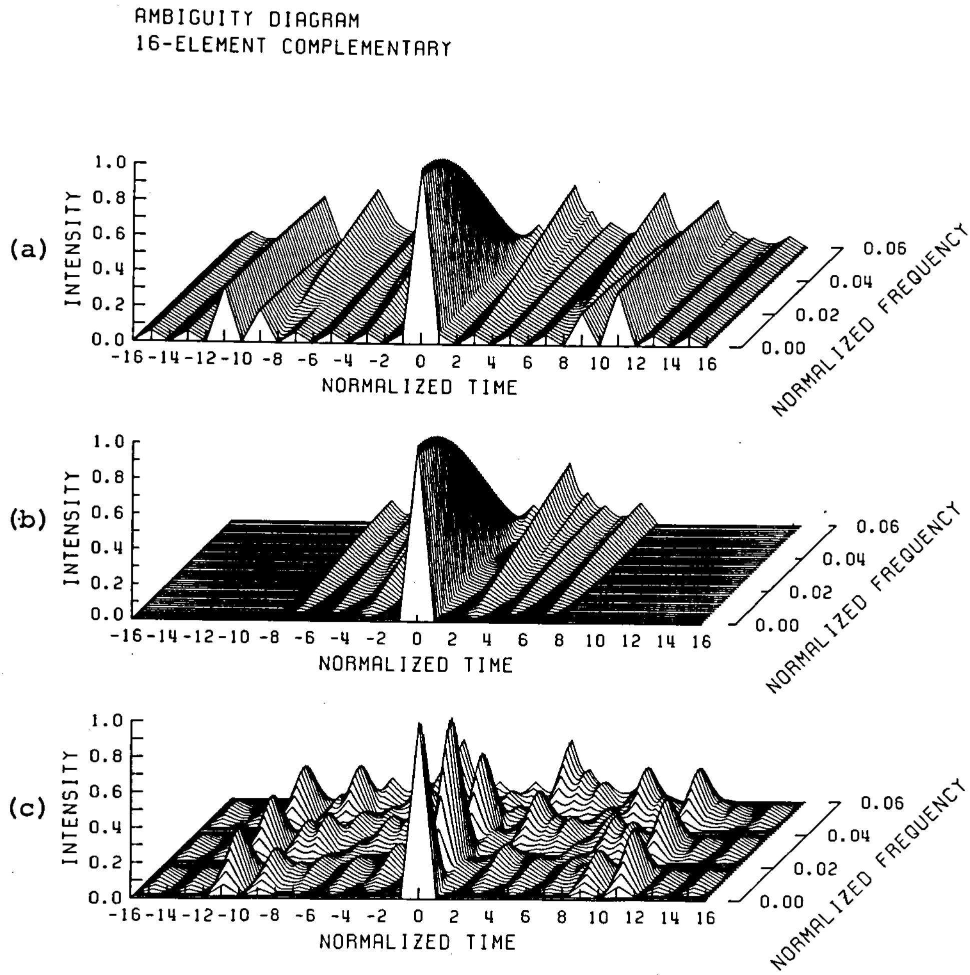

Figure 2.2. A plot of $|\chi(t,\omega)|$ of the 16-element complementary code for (a) even code, (b) even and odd codes with interpulse period (IPP)=0 and (c) even and odd codes with IPP=50. Time and frequency are in normalized units based on a subpulse duration as in Figure 2.1.

are equal to those of even (or odd) code, the sidelobe suppression factor Γ becoming poorer than that of the Barker codes. Therefore, the use of the complementary code implies that the maximum Doppler frequency of radar targets should be smaller than $\omega=\pi/T$.

The sidelobe suppression factor depends on the target Doppler frequency and the interpulse period of radar transmitter as shown in Figure 2.3. Assuming a 1 μs subpulse duration, the frequency range from 0.1 to 100 Hz is illustrated. Γ for 13-element Barker code, which is constant throughout the pertinent frequency range, is also given (dotted line). It is concluded from Figure 2.3 that the sidelobe suppression factor Γ is inversely proportional to the square of Doppler frequency. Figure 2.3 also represents that Γ is higher than that of the Barker code for $\omega_d < 0.071(2\pi/T)$.

When the radar is operated for a distributed target such as atmospheric fluctuations and ocean surfaces, the spectral width in Doppler frequency should be taken into consideration. Figure 2.4 shows a sidelobe suppression factor Γ against the spectral width with zero mean Doppler frequency where a distributed target with Gaussian frequency distribution is assumed. The abscissa is a half power width (-3 dB) of spectral distribution function. Figure 2.4 shows the similar characteristics to Figure 2.3. Γ decreases two order in magnitude if the spectral width increases by a factor of 10. Γ is higher than that of the Barker code for a

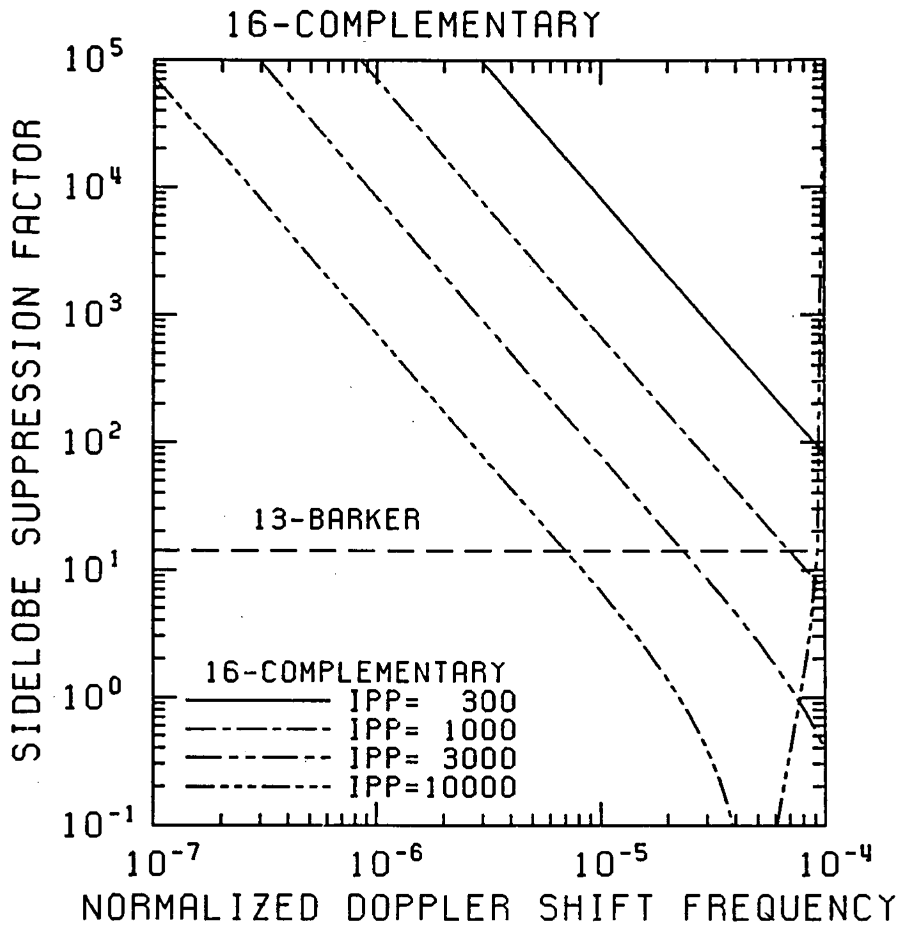

Figure 2.3. Sidelobe suppression factors versus Doppler shift frequency for interpulse period IPP=300,1000,3000, 10000. Time and frequency are in normalized units based on a subpulse duration. The dotted line is for a 13-element Barker code.

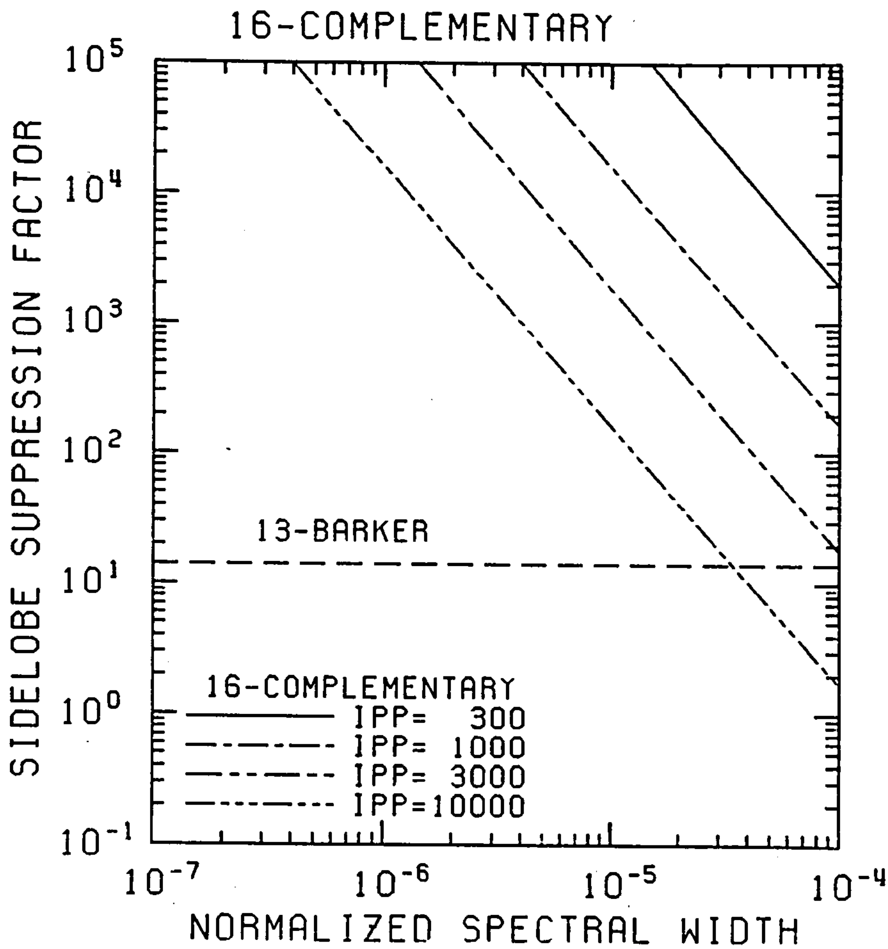

Figure 2.4. Sidelobe suppression factors versus spectral width for interpulse period IPP=300,1000,3000,10000. Time and frequency are in normalized units based on a subpulse duration. The mean Doppler shift is assumed to be zero. The dotted line is for a 13-element Barker code.

spectral width $\omega_H < 0.034(2\pi/T)$.

For VHF MST radars, typical values of the Doppler shift and the spectral width are of 1 Hz order, while the interpulse period is about 1 ms. Thus, Γ for the complementary code is a few tens of decibels higher than that of the Barker codes. It could be concluded that the complementary code is optimum for middle atmosphere observation with VHF radars. The Doppler frequency and spectral width for UHF radars are one order in magnitude larger than those for VHF radars, Γ being 40 dB lower in UHF than in VHF. Then, the performance of the Barker code may become higher than the complementary code for upper mesosphere observations. It should be noticed, however, that the nature of the ambiguity function of the phase-coded pulse, especially for Barker code, has the narrow mainlobe with wide plateau of sidelobes. This means that the resolution performance will be poor when a weak target is to be detected in the presence of much stronger ones.

Use of frequency-modulated (FM) pulses is another compression technique. The ambiguity function of FM pulses does not have a wide plateau, but it possesses a sharp ridge, which is suitable for our application. Thus, FM pulses may be an alternative of the Barker phase-coded pulse. There is a possibility to use FM pulses for UHF radar observations of the mesosphere and thermosphere, if an extremely high range resolution is required as was used for the troposphere observation (Noonkester and Richter, 1980).

2.3 RESOLUTIONS IN THERMAL SCATTER OBSERVATION

For thermal scatter observations, the power spectrum or autocorrelation function (ACF) of radar echoes is first calculated. The estimates are compared with a set of theoretical curves to obtain the atmospheric parameters (Evans, 1969, 1975). The accuracy of the measurements is defined by resolutions in frequency ($\Delta\omega$), altitude range (Δh) and time (Δt). Since the correlation time of echoes is much shorter than the interpulse period (IPP) of radar system, the correlation function method (CFM) is generally employed (Farley, 1969). In CFM, the resolutions are independently determined in frequency and altitude. Echoes scattered by the thermal fluctuations are so weak that many samples are averaged to effectively improve the signal-to-noise ratio (SNR). The time resolution is defined as the time required to make a measurement to a specified precision. The SNR is proportional to the transmitted pulse duration. Thus, the resolutions in time and altitude are inseparably related.

In this section, we discuss the resolution properties for CFM with the radar ambiguity function. The relation between Δh and Δt is formulated and applied to the multiple phase-coded pulse technique to improve the resolutions (Fukao and Wakasugi, 1976, 1977).

2.3.1 Correlation function method

As the length scale of correlation for thermally scattered signals is negligibly shorter than the Fresnel radius at pertinent altitude, a plane wave approximation is applicable to (2.5) and the discussions in the following are restricted only to the altitude coordinate z. $R(t+\tau,t)=\langle q(\vec{R}o,t+\tau)q^*(\vec{R}o,t)\rangle$ represents the autocorrelation function (ACF) of backscattered signals at times $t+\tau$ and t. Using (2.5) and (2.8), $R(t+\tau,t)$ is readily obtained as follows;

$$R(t+\tau,t) = Ao^2 \iint \Phi(0,0,2k,\omega) \exp[j\omega\tau]$$

$$\cdot \chi^*_{vu}(t+\tau-2z/c,\omega)\chi_{vu}(t+2z/c,\omega)\, dz d\omega \quad (2.15)$$

where $Ao=AD^2h/(4\pi Zo^2)$ (D: the antenna beam extent at altitude Zo, $h=h(\vec{r},t)$ is a constant, assuming a homogeneous scattering volume). 2k is the Bragg wavenumber and τ is the time lag of ACF.

(2.15) shows the four-dimensional spectrum simply multiplied by the ambiguity function in the ω domain. This is the advantage of the CFM over the filter-bank method (FBM) which directly measures the spectrum using a bank of filters, i.e., Φ is convolved with χ in FBM, resulting in poor resolutions for altitude and frequency.

Letting $\tau=0$ in (2.15), we obtain the signal power as

$$A_o^2 \iint \Phi(0,0,2k,\omega) \left|\chi_{vu}(t-2z/c,\omega)\right|^2 \, dz d\omega \qquad (2.16)$$

There are three schemes of measurements as shown in Figure 2.5 (Farley, 1969). The altitude range from which a signal is received at a given time is represented by the hatched areas. Echoes for length scales larger than one Debye length exhibit no correlation (e.g., Evans, 1975). Thus, signals are assumed to be uncorrelated from different altitudes while contribution from the darkly shaded areas in the figure is correlated. Uncorrelated signals from different altitudes add to noise, being called self-clutter. The pulse duration uniquely determines the resolution in altitude. The resolution in frequency is determined by the measurable maximum time lag of the ACF, which is proportional to the effective duration of transmitted pulse.

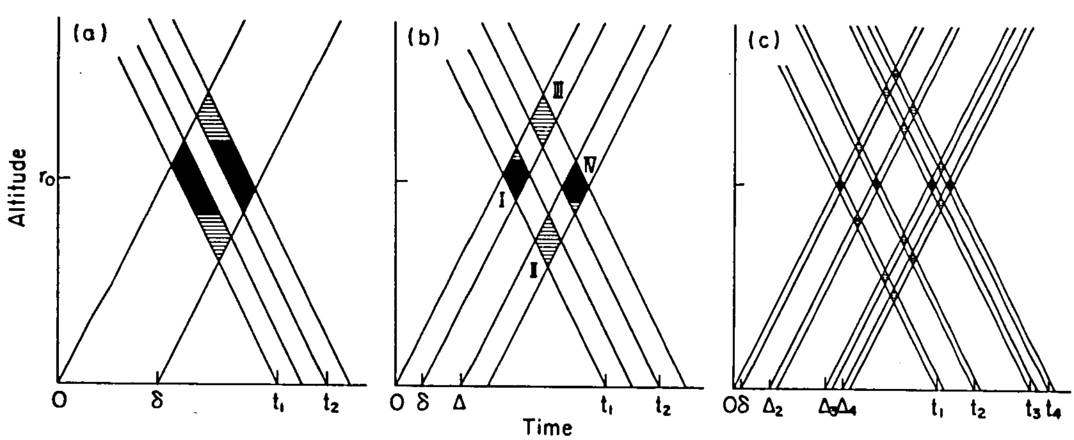

Figure 2.5. Altitude-time diagram for (a) single, (b) double and (c) multiple pulse transmissions.

In the single-pulse method, only one pulse with a long duration is transmitted (Figure 2.5(a)). In this method, the pulse duration limits the measurable maximum time lag. The altitude resolution and the SNR are proportional to the value of time lag, and the SNR becomes extremely poor as the time lag increases.

Two or more pulses having the same duration are transmitted in the double- and multiple-pulse methods as shown in Figures 2.5(b) and (c). In these methods, it is possible to compute the ACF for long time lags without losing altitude resolution. The waveform of transmitted pulses u(t) is expressed as $u(t)=\sum_{i=1}^{p} b(t-\Delta_i)$ where b(t) is the waveform of an individual pulse with a duration of δ. $\Delta_1(=0), \Delta_2, \ldots, \Delta_p$ are the spacings at which a sequence of p pulses are transmitted. The ambiguity function χ_{vu} is the superposition of χ_{vb}'s if we omit the negligibly small N-th round-trip echoes.

$$\chi_{vu}(t,\omega) = \sum_{i=1}^{p} \chi_{vb}(t-\Delta_i,\omega) \tag{2.17}$$

Since χ_{vb} is zero for $\delta<|t-\Delta_i|$, $\chi_{vu}^*\chi_{vu}$ in (2.15) will lead to simpler expression under appropriate conditions.

(i) If $|\tau-\Delta_i| < \delta$, $\min.(\Delta_i) > 3\delta$, and $\tau > 2\delta$,

$$\chi_{vu}^*\chi_{vu} = \chi_{vb}^*(t+\tau-\Delta_i-2z/c,\omega)\chi_{vb}(t-2z/c,\omega) \tag{2.18}$$

(ii) If $\tau=\Delta_i$ and $\min.(\Delta_i) > 2\delta$,

$$\chi^*_{vu}\chi_{vu} = |\chi_{vb}(t-2z/c,\omega)|^2 \qquad (2.19)$$

The scheme of (ii) is preferred, for the size of correlated areas (i.e., the altitude resolution) does not change with the values of τ and Δ_i.

Substituting (2.19) into (2.15),

$$R(t+\tau,t) = Ao^2\iint \Phi(0,0,2k,\omega)$$

$$\cdot|\chi_{vb}(t-2z/c,\omega)|^2\exp[j\omega\tau]\ dzd\omega \qquad (2.20)$$

Thus, the estimated autocorrelation function is shown to be a Fourier transform of $\Phi(0,0,2k,\omega)$ smeared by $|\chi(t-2z/c,\omega)|^2$. If the bandwidth of χ in the ω domain is sufficiently wider than that of $\Phi(0,0,2k,\omega)$, the estimates in CFM are freed from the systematic distortions due to the radar system.

2.3.2 Statistical error estimation

The estimates of ACFs, free from the systematic distortions, always suffer from random statistical errors. The variance $\varepsilon^2(\tau)$ of the estimated ACF can be expressed as follows (Farley, 1969);

$$\varepsilon^2(\tau) = [(S+C+N)/S]^2[1+Rs^2(\tau)]/Ks$$

$$+ (N/S)^2[1+Rn^2(\tau)]/Kn \qquad (2.21)$$

where S, C and N are the powers of thermally scattered signal, self-clutter and noise, respectively. $Rs(\tau)$ and $Rn(\tau)$ are the ACFs of the backscattered signals and noise, and Ks and Kn the numbers of samples, respectively.

(2.21) shows that the power from self-clutters also contaminate the estimates of ACF in the similar way as the noise. For practical measurements, Kn is considerably larger than Ks (i.e., $Kn >> Ks$), and only the first term in (2.21) is retained. Assuming further that all computed lags of the ACF are equally useful in determining the atmospheric parameters (Farley, 1972), the variance of ACF estimation can be written as follows;

$$\varepsilon^2 = [(S+C+N)/S]^2/Ks \qquad (2.22)$$

2.3.3 Multiple compressed-pulse method

It is expected that the combination of the multiple pulse method and the pulse compression technique improves the resolutions in altitude and time. However, range sidelobes, which generally appear by compression, produce uncorrelated signals from the neighboring altitudes. These signals, in addtion to noise, contaminate the estimates of the ACF.

$\Delta H = c\delta/2$ is the altitude range illuminated by a single (uncompressed) pulse with a duration δ. ΔH and the effective resolution Δh are related by $\gamma\Delta h = \Delta H$, where γ is the pulse compression ratio defined in Section 2.2. For multiple compressed-pulse measurement, (2.20) with $\tau=0$ represents the signal power, So, for the range $Zo \pm \Delta h/2$, which can be written as follows;

$$So = \gamma Ao^2 \iint_{Zo-\Delta h/2}^{Zo+\Delta h/2} \Phi(0,0,2k,\omega)$$

$$\cdot \left|\chi_{vb}(2(Zo-z)/c,\omega)\right|^2 \, dz d\omega \qquad (2.23)$$

The power from range sidelobes, Co, which contributes to the self-clutter, is given by

$$Co = \gamma Ao^2 \left[\iint_{Zo-\Delta H/2}^{Zo-\Delta h/2} + \iint_{Zo+\Delta h/2}^{Zo+\Delta H/2} \right]$$

$$\cdot \Phi(0,0,2k,\omega) \left|\chi_{vb}(2(Zo-z)/c,\omega)\right|^2 \, dz d\omega \qquad (2.24)$$

For a p-pulse scheme, the total returned power is composed of So+Co from the desired altitude and $\sum_{i=1}^{p-1}(Si+Ci)$ from other undesired altitudes. Assuming a uniform target, Si=So and Ci=Co (i=1, 2,....,p-1). The total self-clutter power contained in each sample becomes $Co+\sum_{i=0}^{p-1}(Si+Ci)$ for measurement with p compressed-pulses.

With a sequence of p pulses, it is possible to calculate simultaneously ${}_pC_2$ different time lags. The resolution in time (Δt) and the number of samples Ks are related to $TKs = {}_pC_2\Delta t$, where T is the interpulse period of the p-pulse train. Combining (2.22)-(2.24), the following exprssion is obtained.

$$\varepsilon^2 = (T/{}_pC_2\Delta t)\left[\sum_{i=0}^{p-1}(Si + Ci) + N\right]^2/So^2 \qquad (2.25)$$

The measurement precision of the ACF, ε^2, varies as a function of γ, p, Δt and Δh. The relation between these parameters with simplified models of $\Phi(0,0,2k,\omega)$ and $|\chi|^2$ is discussed below. (2.23) and (2.24) suggest that the multiplication of $\Phi(0,0,2k,\omega)$ by $|\chi|$ gives So and Co. In Figure 2.6, Φ is supposed to have a uniform spectral density with a bandwidth of Bo (shaded region). Assuming a phase-coded pulse, a thumbtack ambiguity diagram $|\chi|^2$ is adequate (Skolnik, 1980). The widths of the mainlobe are Tb and $1/\delta$ along the range and frequency directions, respectively ($Tb=\delta/\gamma$ is the compressed pulse duration). While the wide plateau surrounding the mainlobe is complicated, the average density of plateau is $\gamma/(\gamma+1)$ (Rihazeck, 1965). Using the models in Figure 2.6, So and Co are readily obtained as follows;

$$So = \gamma Ao^2 Bo\Delta h \qquad (2.26)$$

$$Co = \gamma Ao^2 Bo\Delta h(\gamma-1)/(\gamma+1) \qquad (2.27)$$

Thus,

$$So/Co = (\gamma-1)/(\gamma+1) \qquad (2.28)$$

So/Co is considered as the sidelobe suppression factor Γ, which is

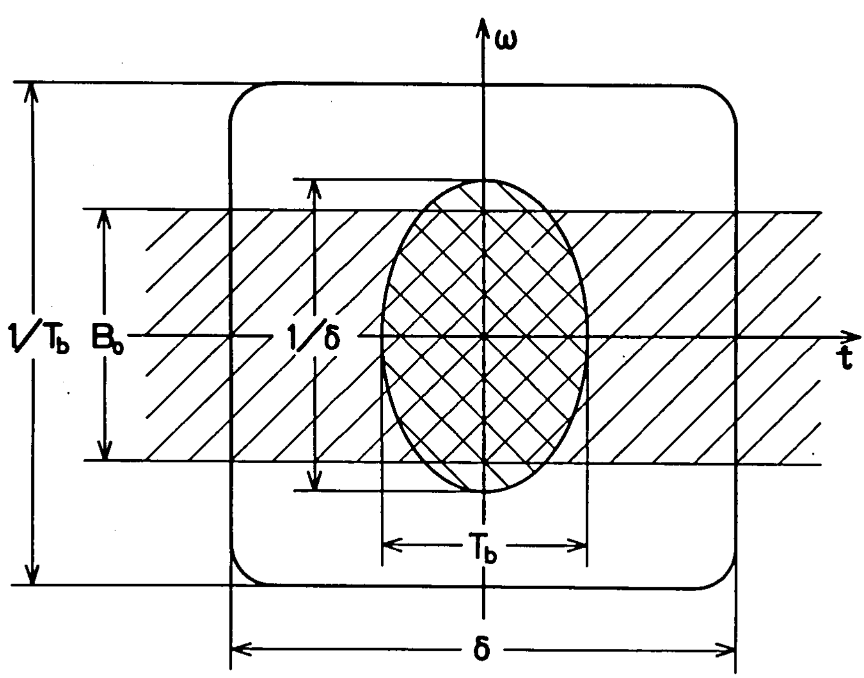

Figure 2.6. A schematic relation of power spectrum and ambiguity function. δ and Tb are the transmitted and compressed pulse durations, respectively. A thumbtack ambiguity function is asummed.

discussed in Section 2.2. For a uniformly distributed target, (2.28) implies that So/Co approaches unity as the compression ratio γ increases to infinity.

The noise power is inversely proportional to a range resolution Δh, if the bandwidth of the receiver is matched to the transmitted pulse. Thus N in (2.25) can be written as $(N/S)o/\gamma\Delta h^2$, where $(N/S)o$ is a constant dependent upon the target cross-section and the radar sensitivity. Combining (2.25)-(2.27), the measurement precision ε^2 is related to γ, p, Δh and Δt as follows;

$$\varepsilon^2 = \frac{2T}{\Delta t p(p-1)} [\frac{2p\gamma}{\gamma+1} + (\frac{N}{S})^2 \frac{1}{\gamma\Delta h^2}]^2 \qquad (2.29)$$

The resolutions in altitude and time are directly related to the given values of ε^2 and IPP.

$$R\Delta t = \frac{2}{p(p-1)} [\frac{2p\gamma}{\gamma+1} + (\frac{N}{S})^2 \frac{1}{\gamma\Delta h^2}]^2 \qquad (2.30)$$

where $R = \varepsilon^2/T$. For MST radar measurements, the altitude resolution is essentially determined by the phenomena to be observed. Thus the design of an experiment is how to minimize $R\Delta t$ by choosing the variables, p and γ.

(2.30) is approximated to $8p\gamma^2/(p-1)(\gamma+1)^2$ for a large signal power ($S/N >> 1$), Δt becoming independent of Δh. $R\Delta t$ become 8 for $\gamma=\infty, p=\infty$, while the minimum value of $R\Delta t=2$ is obtained for $\gamma=1, p=\infty$. This implies that the time resolution is not improved by compression when $(S/N) \gg 1$ (So/Co reaches unity as $\gamma \to \infty$). A simple CW pulse is optimum for the phenomena where strong echoes are expected.

By (2.30), the following criteria are obtained; (i) If $\gamma_1=\gamma_2$ and $p_1 > p_2$, $(R\Delta t)_{\gamma_1 p_1} < (R\Delta t)_{\gamma_2 p_2}$. A larger number of pulses always improves Δt if other practical conditions permit. (ii) Pulse compression is effective only when the condition $(\Delta h)^2 < (N/S)o\ (\gamma+1)/(p\gamma)$ is satisfied.

Figure 2.7 shows an example of the $R\Delta t$-Δh curves. The compression ratio of unity and 13 corresponds to a simple CW pulse and a 13-element Barker-coded pulse, respectively. A double- and seven-pulse scheme is assumed (p=2,7). The dotted lines and chains in the figure are for the cases of $R\Delta t=2$ and 8, respectively. Figure 2.7 obviously indicates that the poorer the signal-to-noise ratio is, the greater the improvement in $R\Delta t$ by multiple compressed-pulse method is. With a high signal-to-noise ratio, the multiple pulse scheme still gives a slight improvement, however, the use of pulse compression is proved to worsen the resolution.

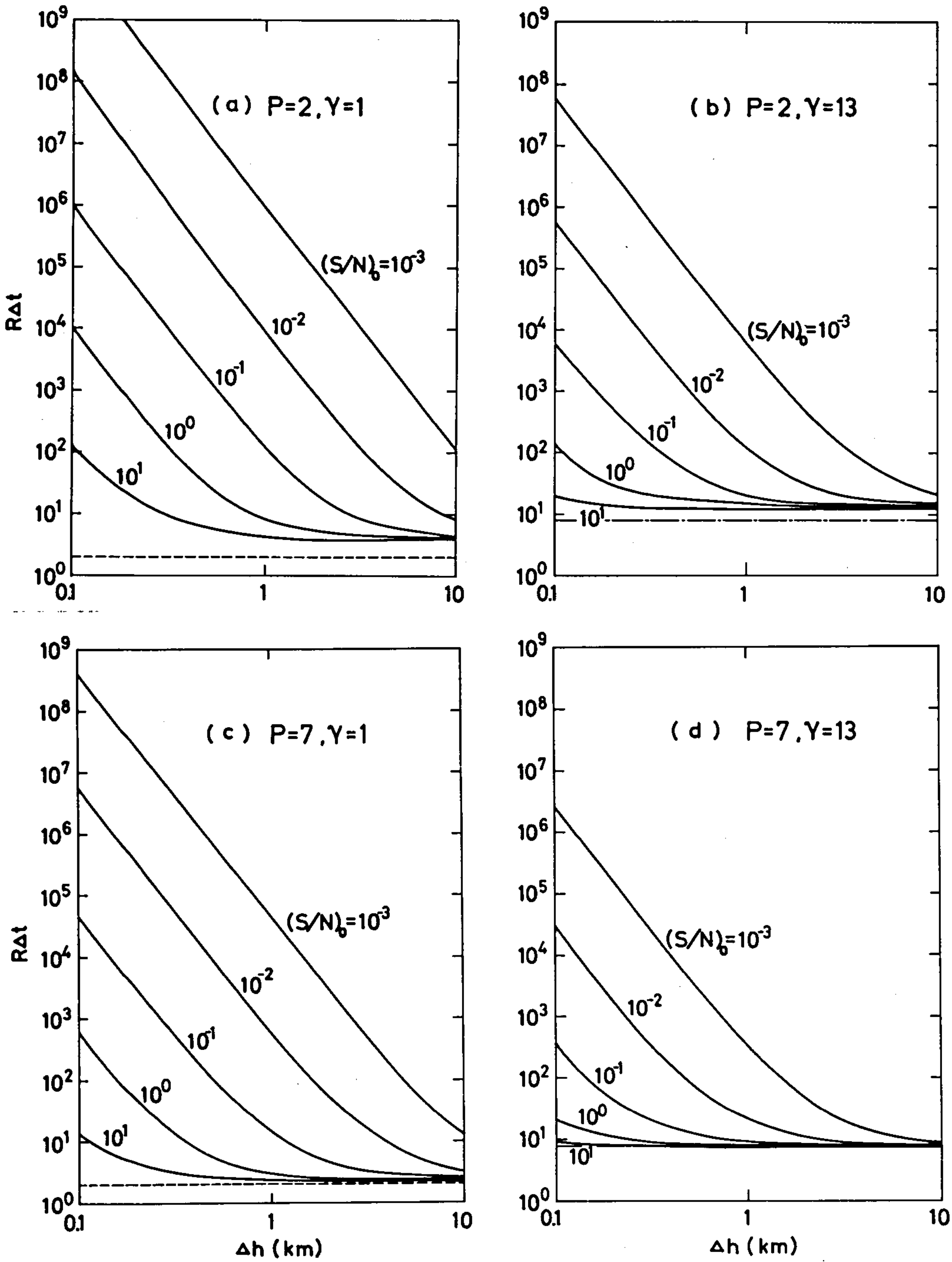

Figure 2.7. RΔt-Δh diagrams for multiple compressed-pulse measurements. Number of pulses (p) and pulse compression ratio (γ) are for (a) p=2, γ=1, (b) p=2, γ=13, (c) p=7, γ=1 and (d) p=7, γ=13. The dotted lines and the chains correspond to RΔt=2 and 8, respectively.

2.4 PARAMETER ESTIMATION IN TURBULENT SCATTER OBSERVATION

Turbulent scatter and Fresnel reflection are two fundamental models which have been used to explain the echoing mechanisms from the middle atmosphere. It is thought that the turbulent scatter holds the dominant roles for MST radar measurements. Fresnel reflection has been suggested in explaining the strong aspect sensitivity of scattering, which has been observed in the troposphere and stratosphere (Gage and Green, 1978; Röttger and Liu, 1978; Fukao _et al._, 1978) and in the mesosphere (Fukao _et al._, 1979, 1980b). Fresnel reflection is due to the infinite dielectric gradient at the edges of a scattering layer. This condition has been excluded in deriving the backscattered signals in (2.5). However, it is still possible to include the aspect sensitivity by assuming an anisotropic structure of dielectric fluctuations.

In this section, radar wave scattering from anisotropic fluctuations is discussed. Temporal power spectra of backscattered signals are first estimated. Then filtering effects of the radar system are discussed. Parameters such as echo power, Doppler shift and spectral width are also estimated.

2.4.1 Periodogram estimation

The MST radar transmits a train of RF pulses with interpulse period (IPP) T and the echo signal is range-gated and sampled for every IPP. For turbulent scatter observations, the signal correlation time To is longer than IPP. Sampled data at pertinent range are considered as discrete time series with a complex value. Furthermore these data are assumed to be a stationary time series in a limitted time duration so that the theory of stochastic processes is applicable. In order to estimate atmospheric parameters, spectral analysis appropriate to radar signals is employed.

The spectral estimates by maximum entropy method (MEM), which concerns the prediction theory of a stationary process, have spiky structure (e.g., Ulrych and Bishop, 1975; Kaveh and Cooper, 1976). This property proves to be inconvenient in our application. Ogura and Yoshida (1981) recently proposed a revision of MEM and have successfully applied the revised method to the data of Jicamarca and Arecibo radar observations.

Spectral estimates by the classical periodogram method have a disadvantage in that a spiky spectral structure appears. This is because each spectral point is chi-squared random variable with two degrees of freedom (Bartlett, 1978). Therefore some averaging procedures are needed but this will restrict the resolutions in time and/or frequency. Barrick (1980) discussed the relation between the accuracy of estimates and the numbers in averaging.

Despite such disadvantage, however, the periodogram method by the fast Fourier transform (FFT) algorithms is widely employed because of the computational advantage of the FFT. The MEM needs correlation functions, which can be calculated from the inverse FFT of periodogram much faster than the conventional correlation algorithms. Thus the Fourier transform of backscattered signal and the estimates of the periodogram is discussed below.

The Fourier transform of backscattered signal in (2.5) is defined as follows;

$$Q(\Omega) = \int w(t)q(t)\exp[-j\Omega t]\, dt \qquad (2.31)$$

where $q(t) \equiv q(\vec{0},t)$, which means that the radar is at the origin. Amplitude weight function $w(t)$ which reduces the undesirable effects related to spectral leackage by finite-duration data. The properties of $w(t)$ has been thoroughly reviewed by Harris (1978).

Because of the discrete nature of the sampled radar signals, the 'aliasing' effect occurs (e.g., Papoulis, 1977). $Q'(\Omega)$ calculated by the FFT and $Q(\Omega)$ in (2.31) are related by the expression,

$$Q'(\Omega) = \sum_{n=-\infty}^{\infty} Q(\Omega+2\pi n/Ts), \quad |\Omega| < 2\pi/2Ts \qquad (2.32)$$

where Ts is the effective sampling period. If samples at every IPP at the pertinent altitude are used for the FFT, Ts is equal to T(=IPP). The difference between Ts and T originates from the so-called coherent integration which digitally adds the N successive samples for compressing the data. Thus Ts is equal to NT. As the adding procedure is regarded as a coherent processing of N-pulse train, the ambiguity function in (2.5) should be replaced by χ which has the following expression (Rihaczeck, 1964).

$$|\chi(t,\omega)|^2 = \sum_{n=N-1}^{N-1} |\chi_{vu}(t-nT,\omega)|^2$$

$$\cdot [\sin^2\omega(N-|n|)T/2]/[\sin^2\omega T/2] \qquad (2.33)$$

Since the terms for $n \neq 0$, i.e. the n-th round-trip echoes, are generally neglected in the MST radar measurements, (2.33) is reduced to $|\chi_{vu}(t,\omega)|^2 [\sin^2\omega NT/2]/[\sin^2\omega T/2]$. Thus the coherent integration restricts the effective bandwidth in the Doppler frequency. A simple addition of the samples yields sidelobes in the ω direction, which, in turn, contaminate the estimates of $Q'(\Omega)$. This is because of the aliasing effect caused by the discrete sampling. Interpulse coding such as pulse-to-pulse phase shift and/or the weighted addition of samples lessens the sidelobe level enabling a reliable estimation of $Q'(\Omega)$. These should be noted in the practical signal processing of MST radars.

For turbulent scatter, the length scale of scattering Lo is called the outer scale. Liu and Yeh (1980) showed the classical

Booker-Gordon formula is valid if the condition

$$D/\lambda_F << \lambda /Lo \tag{2.34}$$

is satisfied, where D is the antenna beam width and $\lambda_F=\sqrt{\lambda z}$ the Fresnel radius at altitude z. The length scale Lo was reported to be in the order of 100 m (Woodman and Guillén, 1974; Cunnold, 1975), while the Fresnel radius is a few to ten times larger than Lo for a radio wave of 50 MHz. If an isotropic turbulence is observed with a narrow antenna beam, the Booker-Gordon formula is still applicable, i.e. a simple plane-wave approximation is valid (Tatarskii, 1971).

The condition (2.34) may be unacceptable for anisotropic fluctuation measurements because the effective horizontal scale αLo is comparable to λ_F (α: anisotropy factor of the horizontal to the vertical length scales). Thus the distance from the radar to the scattering point, R in (2.5), should be developed as follows;

$$R \simeq z + (x^2 + y^2)/2z \tag{2.35}$$

Combining (2.5) with (2.35) and substituting into (2.31), $Q(\Omega)$ can be expressed as follows;

$$Q(\Omega) = Ao\iiint w(t)\left|g'(x,y)\right|^2$$

$$\cdot \chi^*(2[Zo-z-(x^2+y^2)/2z]/c,\omega)$$

$$\cdot \exp j[\omega t-k(x^2+y^2)/z-\Omega t]dtd\vec{r}d\varepsilon(\vec{K},\omega) \quad (2.36)$$

where Zo corresponds to the range-gated altitude. For deriving (2.36), the antenna beam is assumed to point parallel to the z direction. Variables x and y in g'(x,y) are distances from the z axis.

The square of $Q(\Omega)$ gives an estimate of the periodogram. The ensemble averaged properties are expressed as follows;

$$<|Q(\Omega)|^2> = <|\int w(t)q(t)\exp[-j\Omega t]dt|^2> \quad (2.37)$$

With (2.8), (2.37) can be approximated to

$$<|Q(\Omega)|^2> = Ao^2\iint \Phi(\vec{K},\omega)\,|H(\vec{K},\omega)|^2\; W^2(\omega-\Omega)\; d\vec{K}d\omega \quad (2.38)$$

where

$$H(\vec{K},\omega) = \int Go(Kx,Ky,z)\chi^*(2(Zo-z)/c,\omega)$$

$$\cdot \exp j[z(Kz-2k)]dz \quad (2.39)$$

$$Go(Kx,Ky,z) = \int \left|g'(x,y)\right|^2$$

$$\cdot \exp j[-k(x^2+y^2)+xKx+yKy]dxdy \quad (2.40)$$

W is a Fourier transform of the amplitude weight function in (2.31). The bandwidth of $W(\omega)$ determines the frequency resolution of the estimated periodogram which is inversely proportional to the time duration of samples effectively used for calculation. $H(\vec{K},\omega)$, which is a four-dimensional filtering function, represents the effects of the radar used in the measurements. Radar frequency, antenna beamwidth and pulse waveform determine the properties of the filtering function $H(\vec{K},\omega)$. In the next subsection, these properties are discussed in detail.

2.4.2 Radar filtering function

The finite extents of scattering volume distort the echo properties. This effect has been discussed on many occasions. Valley (1975) concluded that at the edges of the rectangular layer there was Fresnel reflection even in cases where the layer was of many wavelengths thick. Liu and Yeh (1980) showed that the Doppler shift and the correlation time were both modified due to the finite thickness of the layer. However, they restricted the treatment only to the one-dimensional case, and it is necessary to investigate the effect of the horizontal extents to complement their discussion. This is especially important for the anisotropic fluctuation measurements. In the following the effect of three-dimensional finite scattering volume, which is relevant to the antenna beamwidth and pulse duration, is discussed.

In order to provide concrete calculations, a uniformly-excited antenna aperture is assumed. $g'(x,y)$ in (2.40) then becomes

$$g'(x,y) = \mathrm{sinc}[(kLx/Zo)x]\,\mathrm{sinc}[(kLy/Zo)y] \quad (2.41)$$

where $\mathrm{sinc}[ax]=2\sin(ax)/(\pi x)$. Lx is the length of antenna aperture in x direction. We define the beamwidth at Zo as follows

$$Dx = \lambda Zo/Lx \quad (2.42)$$

The same condition holds for the y component.

If the beamwidth D is much smaller than the Fresnel radius λ_F at a pertinent altitude, radar wave can be approximated to a plane wave, a condition necessary for the approximation of the Booker-Gordon theory as shown in (2.34). Figure 2.8 shows the ratio of the beamwidth D to the Fresnel radius λ_F for 50 MHz MST measurements. L=10, 30, 100, 300 m are sizes of the antenna. The ratio is about a few to ten for typical MST radars. A plane wave approximation is not always valid, and thus a careful treatment should be made. Range, where the ratio is smaller than unity, corresponds to the Fresnel and/or near-field region of the antenna. This particular region is beyond our formulation.

(2.40) includes the effects of the finite beam extent and the spherical surface of the radar wave. If we use the antenna pattern of (2.41), Go(Kx,Ky,z) is expressed as a product of G(Kx,z) and G(Ky,z), horizontal filtering functions in x and y

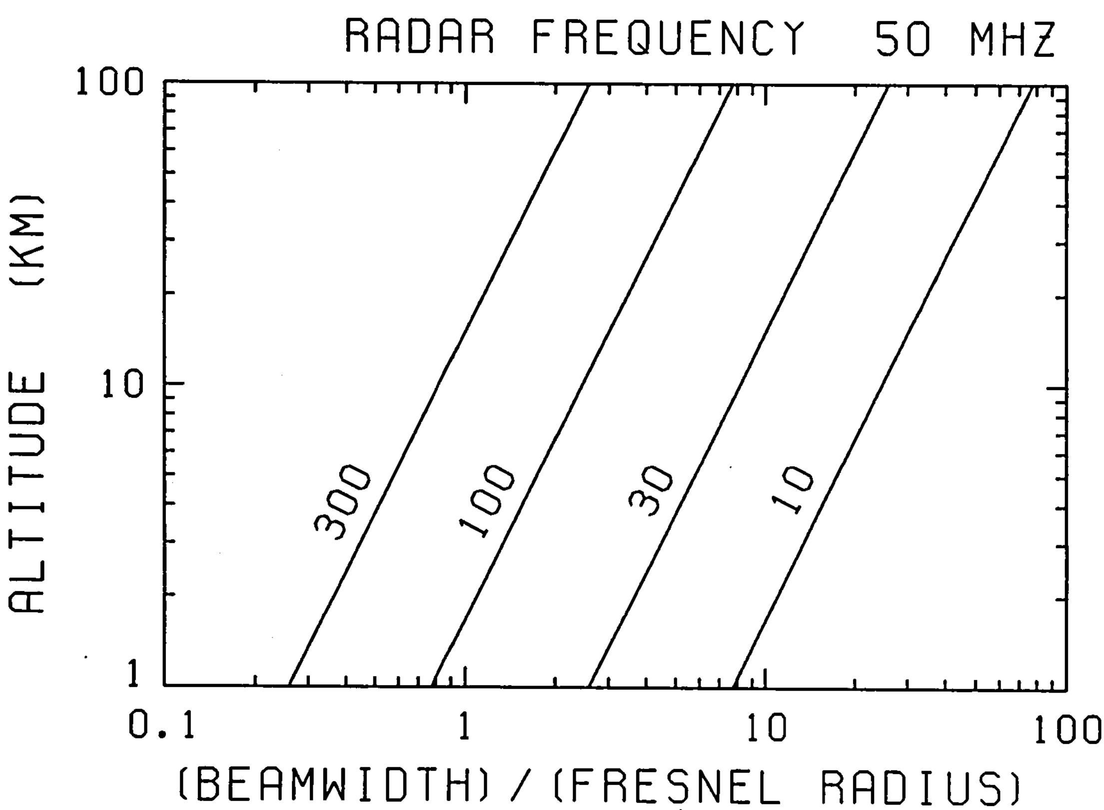

Figure 2.8. Ratio of the antenna beamwidth to the Fresnel radius for MST measurements. Radar frequency of 50 MHz is assumed. L=10,30,100,300 m are sizes of the antenna.

directions, respectively.

$$Go(Kx,Ky,z) = G(Kx,z)\ G(Ky,z) \tag{2.43}$$

where

$$G(Kx,z)=\int sinc^2[(kLx/z)x]expj[xKx-kx^2/z]dx \tag{2.44}$$

$$G(Ky,z)=\int sinc^2[(kLy/z)y]expj[yKy-ky^2/z]dy \tag{2.45}$$

The sinc terms define the extent of the antenna beam, while the quadratic phase terms are due to the spherical nature of radar waves.

Amplitude and bandwidth (-3 dB) characterize the properties of G(K,z) as is shown in Figure 2.9. The antenna beamwidth is normalized by Fresnel radius at pertinent range, thus G(K,z) is independent of the range. The dotted lines in the figure are the results by plane-wave approximation, i.e.,only the effect of finite beam extent is considered. Figure 2.9(a) shows the amplitude of G(K,z) at K=0. The amplitude is proportional to the beamwidth for a plane wave approximation. This results in the increase of scattering volume which means the increase of a scattered power for a plane wave case. The amplitudes of (2.44) and (2.45) converge to a finite value because the phase varies rapidly with beam extent and the echo power are not added coherently. Figure 2.9(b) shows the normalized bandwidth of

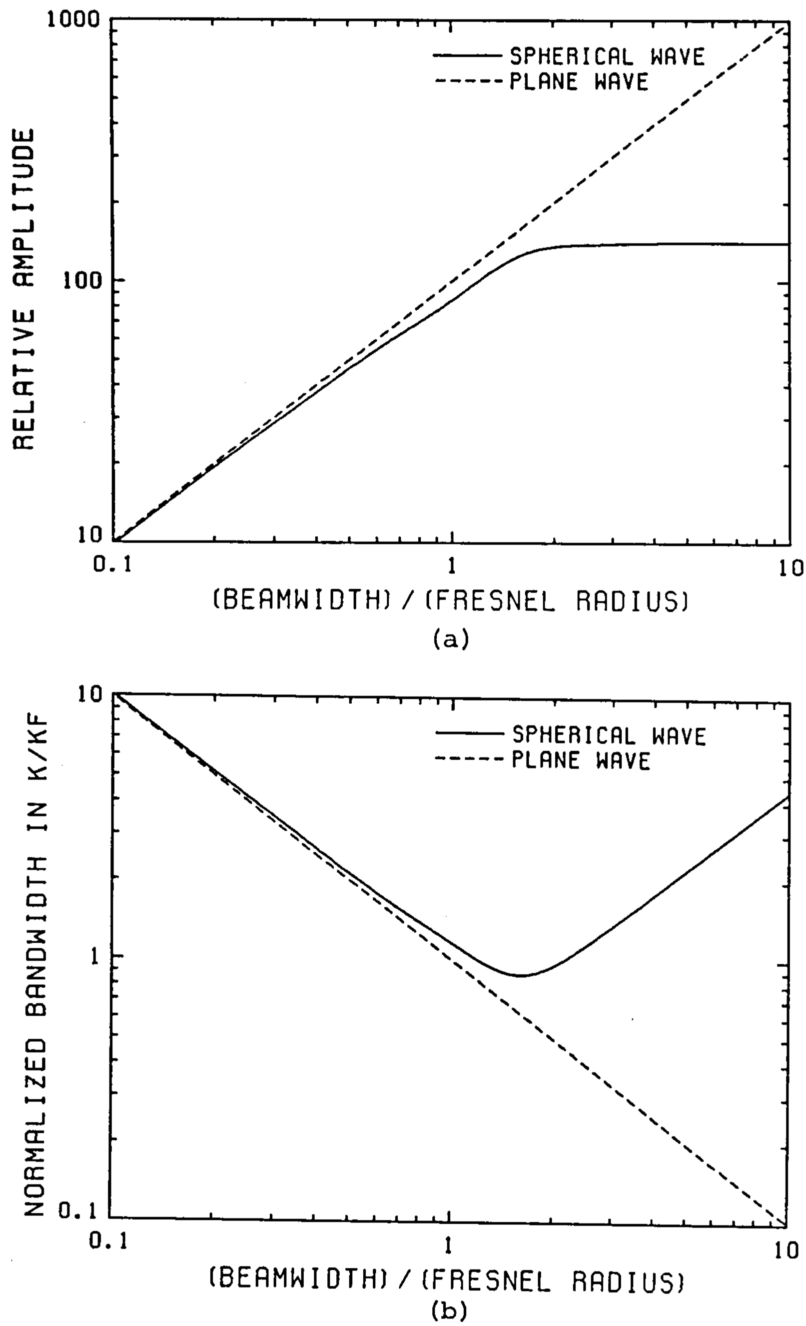

Figure 2.9. (a) Amplitude and (b) bandwidth of the horizontal filtering function. The abscissa is a beamwidth normalized by the Fresnel radius at pertinent range. Dotted lines correspond to the results based on a plane wave approximation.

$G(K,z)$ by the Fresnel wavenumber K_F. For the plane wave approximation the bandwidth converges to zero as the beamwidth increases because the effect of finite beamwidth disappears. In the case of the spherical wave approximation, the results asymptotically approaches to that of the plane-wave approximation for small values of D/λ_F. The beamwidth increases, however, if D/λ_F becomes greater than 1.5, a value realizable for MST radar measurements (see Figure 2.8).

In order to calculate $H(\vec{K},\omega)$ strictly, we should take the integral of χ^*Go. For the typical MST measurements, however, the range resolution is better than 1 km, thus the change of $G(K,z)$ with z is negliginblly small. (2.39) can be approximated thus,

$$H(\vec{K},\omega) = G(Kx,Zo)G(Ky,Zo)G(Kz,\omega) \qquad (2.46)$$

where

$$G(Kz,\omega)=\int\chi^*(2(Zo-z)/c,\omega)\exp j[z(Kz-2k)]dz \quad (2.47)$$

$G(Kz,\omega)$ is a radial filtering function in the z direction. (2.47) is a Fourier transform of $\chi^*\exp j[-2kz]$, which implies that the pulse duration defines the bandwidth in Kz while the center of the filter is shifted by a radar Bragg wavenumber of 2k. In the following, we assume a simple CW pulse without range sidelobes. If the fluctuations are illuminated by a long CW plane wave pulse with an infinite beamwidth, H in (2.38) reduces to $H(0,0,2k,\omega)$.

This coincides with the result of a cross-section approximation (Wheelon, 1972). The effect of the finite pulse duration and/or the finite thickness of scattering layer has been fully discussed (Wheelon, 1972; Valley, 1975; Liu and Yeh, 1980). As such, the relation between the anisotropic structure of fluctuations and the effect of finite beamwidth is discussed in detail here.

As a complete theory for space-time spectrum of fluctuations is not available, the traditional treatment based on the locally frozen hypothsis is considered. If the fluctuation is locally frozen, the space-time spectral density $\Phi(\vec{K},\omega)$ can be expressed as follows (Tatarskii, 1971).

$$\Phi(\vec{K},\omega) = \Phi_3(\vec{K})$$

$$\cdot(2\pi K^2\sigma^2/3)^{-1/2}\exp[-(\omega-\vec{K}\cdot\vec{v})^2/(2K^2\sigma_v^2/3)] \quad (2.48)$$

where $\Phi_3(\vec{K})$ is the spatial spectrum, $\vec{v}$ the mean wind velocity and σ_v^2 the variance of the turbulent velocity. The locally frozen hypothesis implies the condition $|\vec{v}| >> \sigma_v$. If σ_v^2 reduces to zero, (2.48) approaches to (2.49).

$$\Phi(\vec{K},\omega) = \Phi_3(\vec{K})\ \delta(\omega-\vec{K}\cdot\vec{v}) \quad (2.49)$$

which is the space-time spectrum of a frozen condition.

Gaussian spectrum has been used for $\Phi_3(\vec{K})$, because the integration can be easily performed. For realistic modeling of fluctuations, a power law spectrum is more desirable. For anisotropic fluctuations, a power-law spatial spectrum with an index ν is given by

$$\Phi_3(\vec{K})=\alpha Lo^3\Gamma(\nu/2)/[2\pi\Gamma(3/2)\Gamma(\nu-3/2)]$$

$$\cdot[1+(Lo/2\pi)^2(\alpha^2Kx^2+\alpha^2Ky^2+Kz^2)]^{-\nu/2} \quad (2.50)$$

where Lo is the outer scale of fluctuations in the z direction, α anisotropic factor of the x-y to the z directions. The power-law form in (2.50) is the typical spectrum for geomagnetic-field aligned anisotropic irregularities (Crane, 1976,1977). (2.50) reduces to the classical Kolmogorov spectrum of inertial subrange turbulence by assuming $\alpha=1$ and $\nu=11/3$. To simplify the following calculations, ν is assumed to be 4 which is very close to the Kolmogorov case $\nu=11/3\simeq3.67$.

In order to estimate the horizontal wind velocity, the antenna beam is usually tilted from the zenith in the MST radar measurements. The effect of the tilted beam can be easily compromised by rotating the spatial-frequency coordinate by ψ. If the beam is tilted in the x-z plane, ψ is regarded as the antenna zenith angle.

$$Kx' = Kx \cos\psi - Kz \sin\psi \tag{2.51}$$

$$Kz' = Kx \sin\psi + Kz \cos\psi \tag{2.52}$$

In the calculations, when the radar coordinate is fixed, Kx and Kz in (2.50) are now replaced by the transformed wavenumbers Kx' and Kz'.

Combining the foregoing expressions into (2.40), the periodogram for radar signals backscattered by anisotropic fluctuations is obtained. Figure 2.10 shows an example of the calculated periodograms. It is not essential to discuss the effects of the amplitude weight function $W(\omega)$. The spectral leakadge problem has been neglected by assuming $W^2(\omega)=\delta(\omega)$. Parameters for the calculation are given in the figure. Dotted lines represent the estimates based on the Booker-Gordon approximation. Each spectral density functions are normalized by the respective maximum levels. Figure 2.10 shows that the mean Doppler shift and the spectral width do not always agree with those predicted by the Booker-Gordon approximation. In the next subsection, spectral moments are estimated and the relation between the anisotropic fluctuations and the finite beamwidth is discussed.

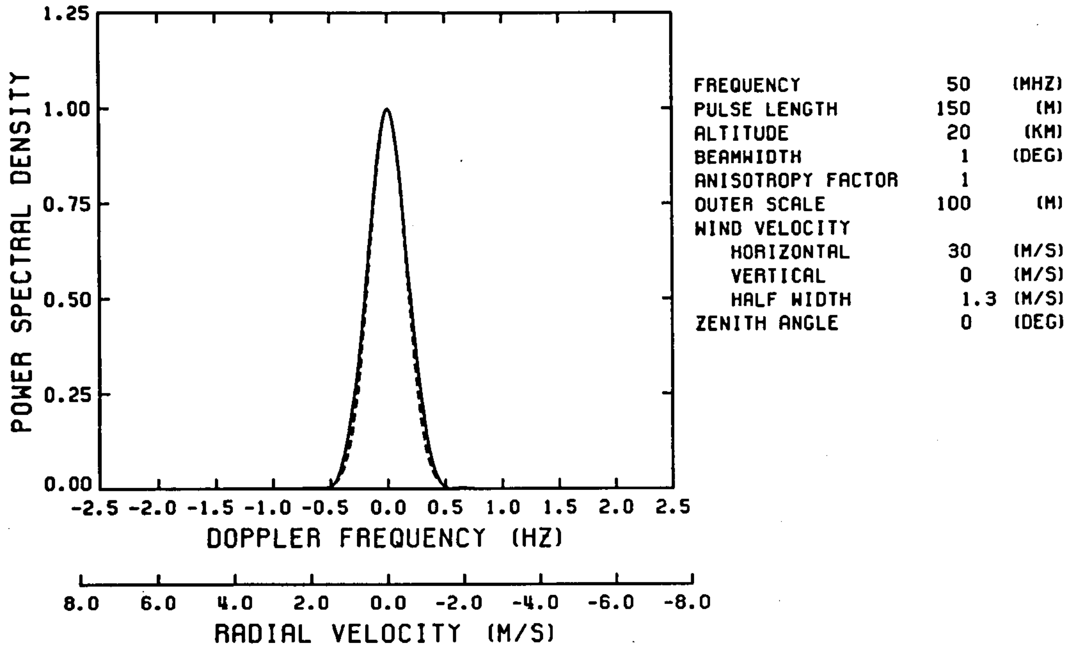

(a)

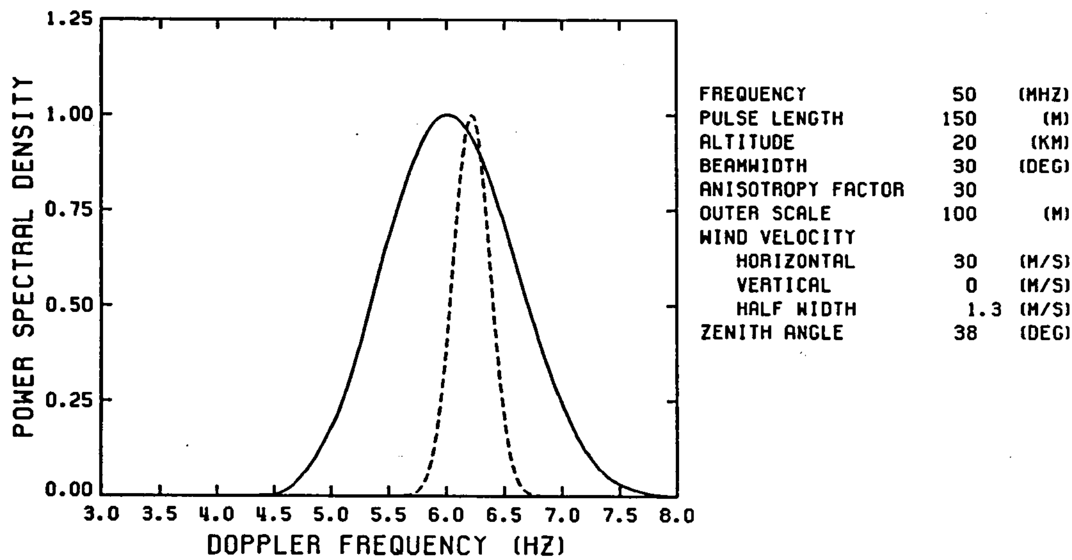

(b)

Figure 2.10. Examples of estimated periodograms with (a) beamwidth 1°, anisotropy factor 1, and (b) beamwidth 30°, anisotropy factor 30. Dotted lines correspond to the plane-wave approximation (Pulse length of 150 m corresponds to the 1-μs pulse duration).

2.4.3 Parameter estimation

Spectral moments are the fundamental parameters which characterize the estimated periodograms. Zeroth, first and second moments correspond to the echo power (P), mean Doppler shift (ω_d) and spectral width (σ), respectively.

$$P = \int <|Q(\Omega)|^2> d\Omega \tag{2.53}$$

$$\omega_d = \int \Omega <|Q(\Omega)|^2> d\Omega/P \tag{2.54}$$

$$\sigma = (\int \Omega^2 <|Q(\Omega)|^2> d\Omega - \omega_d^{\,2})^{1/2} \tag{2.55}$$

These moments provide atmospheric information, however they also depend on the radar parameters such as antenna beamwidth and beam direction. Moment dependence on the beamwidth, zenith angle and anisotropy factor is discussed below. Other parameters such as radar frequency, pulse duration and outer scale length are fixed as practical values which are indicated in Figure 2.10(a). Furthermore, the discussion is restricted to the altitude of 20 km. Calculations at the 80 km altitude are also performed. The results show that the moments at these two different altitudes have similar properties. This is because the ratio of the antenna beamwidth and the Fresnel radius differs by a factor of only 2 at these two altitudes.

A. Echo power

Figure 2.11 shows the echo power against the anisotropy factor for several antenna beamwidth directing to the zenith (ψ=0). The ordinates is a relative power normalized by the echo power predicted by the Booker-Gordon approximation (isotropic fluctuations illuminated by a plane wave). The dotted line shows the echo power obtained by the plane wave approximation. The figure shows that the echo power is linearly proportional to the anisotropy factor for narrow antenna beams. The echo power tends to decrease as the anisotropy factor increases in cases where wide beams are used. For the cases with the anisotropy factor greater than unity, only the echo powers scattered near the zenith contribute to the received power, while all echo powers contribute to the received echo power for the isotropic case.

These properties are represented clearly in Figure 2.12 which shows the echo power dependence on the antenna beamwidth. For the isotropic case, the echo power is identically equal to the value predicted by the Booker-Gordon approximation. This coincides with the results obtained by Liu and Yeh (1980). The Booker-Gordon approximation is applicable when the antenna beamwidth is smaller than the angle of coherence cone of the backscattered waves which is determined by the effective horizontal scale (anisotropy factor times by Lo). The results shown in Figure 2.11 and 2.12 conclude

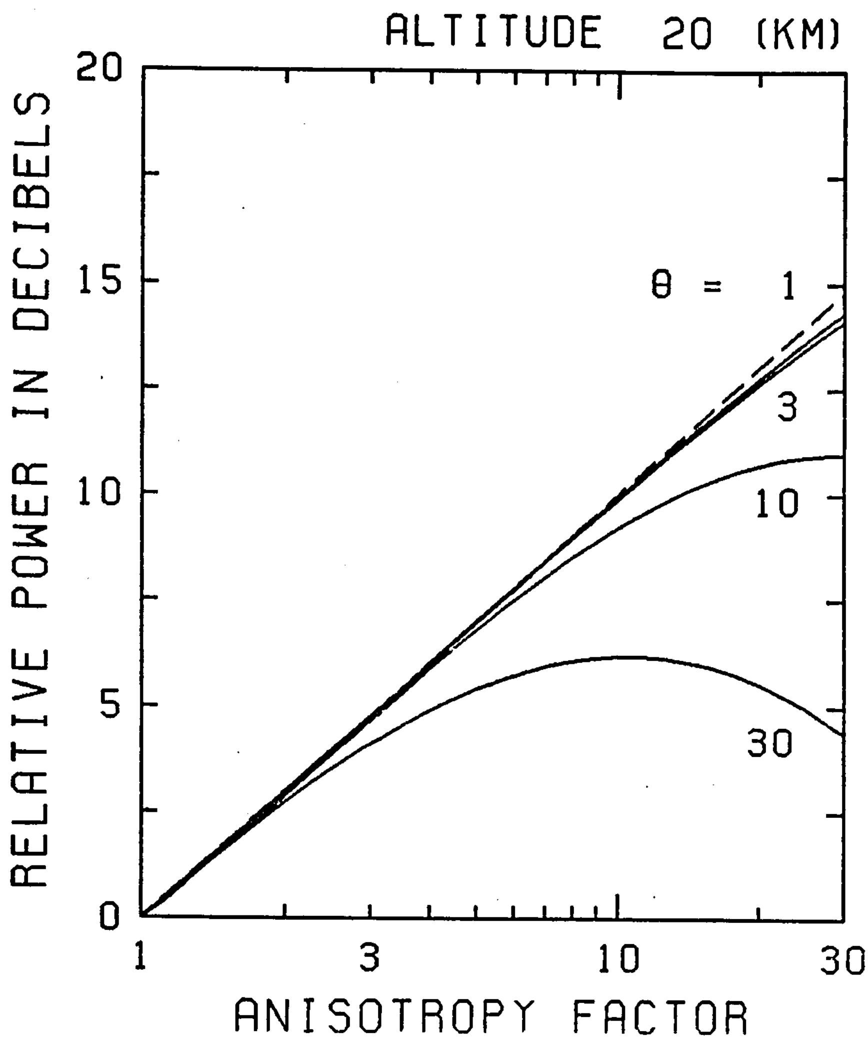

Figure 2.11. Echo power versus anisotropy factor. θ = 1,3,10,30 are the antenna beamwidths in degrees. Echo power is normalized by the value for the isotropic scattering of plane waves. Radar frequency of 50 MHz are assumed.

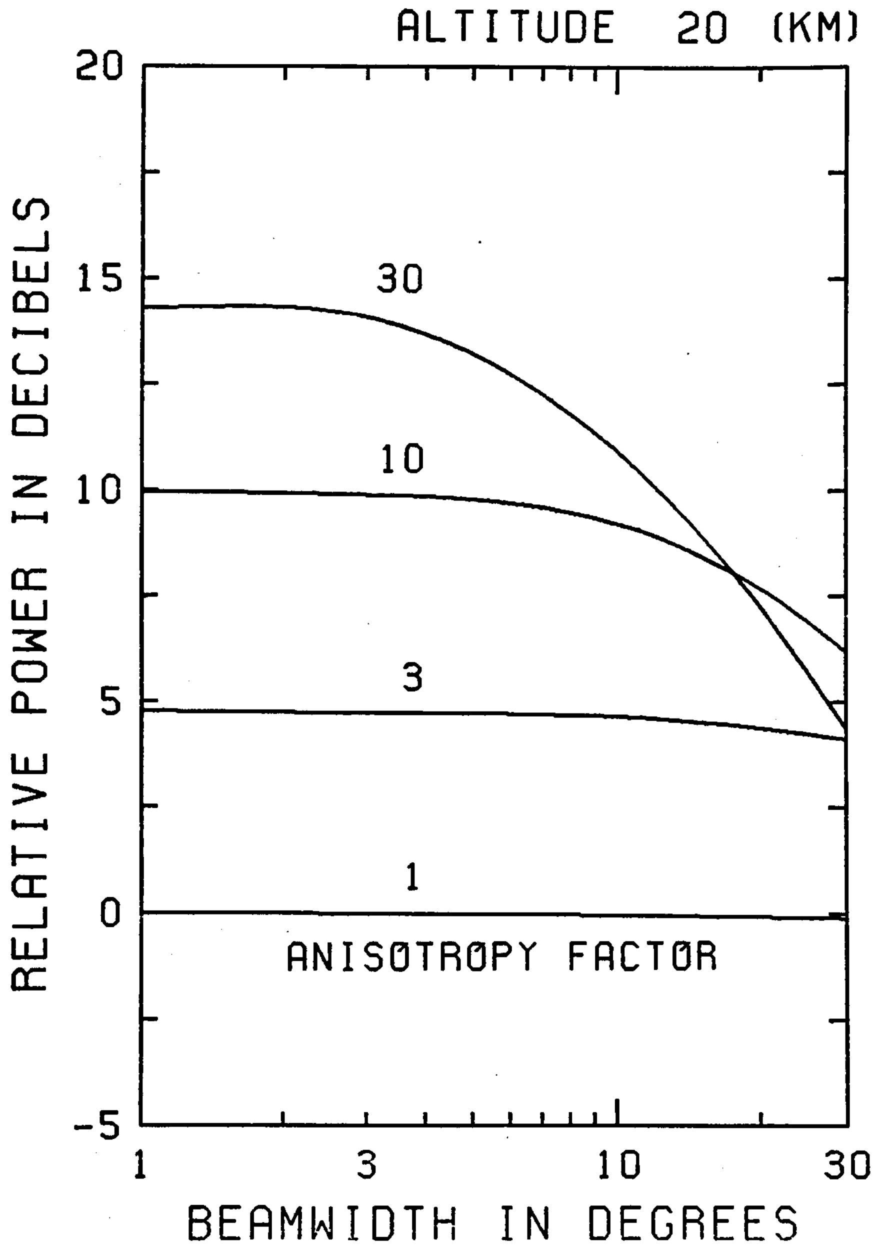

Figure 2.12. Echo power versus antenna beamwidth. $\alpha = 1,3,10,30$ are the anisotropy factors. Echo power is normalized by the value for the isotropic scattering of plane waves. Radar frequency of 50 MHz are assumed.

that the condition in (2.34) becomes invalid for wide antenna beams and/or large anisotropy.

Figure 2.13 shows the echo power dependence on the zenith angle. In the isotropic case, which is not shown in the figure, the echo power is constant and independent of the zenith angle. For a small value of the anisotropy factor the angle of coherence cone is much wider than the beamwidth of radar, resulting in the echo power slightly dependent on the zenith angle. When the anisotropy of fluctuations increases, scattered power is coherently added only in a limitted direction. Thus, the zenith angle dependence is clearly seen. Results observed by Jicamarca radar (beamwidth of 1 degree) conclude that the difference of echo power between the vertical and the off-vertical (3 degrees from the zenith) beams is about several decibels (Fukao et al., 1979). Figure 2.13 suggests that the horizontal length scale of fluctuations is about a few tens times larger than that of the vertical direction.

B. Mean Doppler shift

The relative error between the estimated Doppler shift and the theoretically predicted values determines the accuracy of Doppler shift measurements. Figure 2.14 shows the dependence of the relative error on the zenith angle for the mean Doppler shift estimation. The error is negligibly small and is virtually

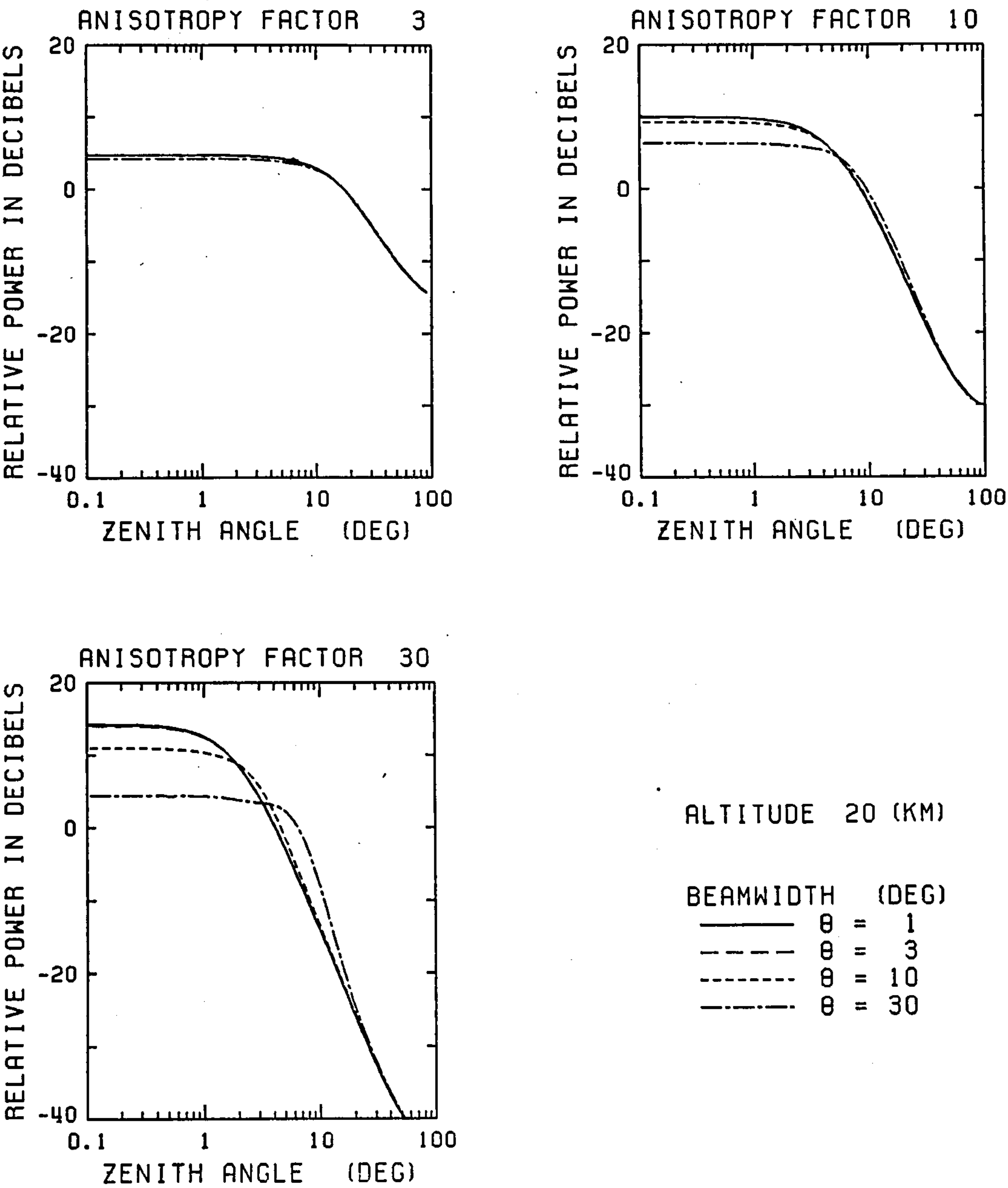

Figure 2.13. Echo power versus antenna zenith angle. Echo power is normalized by the value for the isotropic scattering of plane waves. Radar frequency of 50 MHz are assumed.

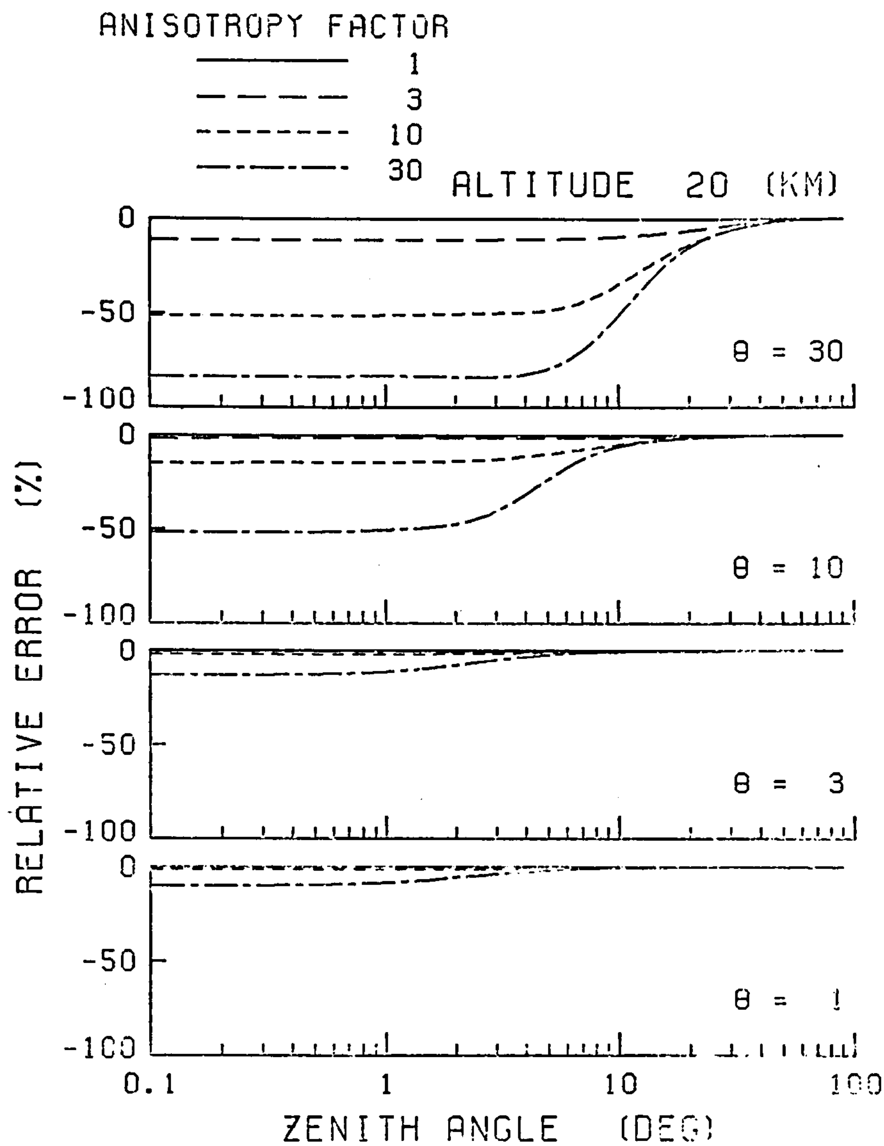

Figure 2.14. Doppler shift estimation error versus zenith angle of antenna beams. θ = 1,3,10,30 are the antenna beamwidths in degrees.

independent of the zenith angle ψ and the anisotropy factor α for the beamwidth smaller than a few degrees. The error increases for larger values of anisotropy with wider antenna beams. It should be noticed that the sign of the relative error is always negative and that the estimated Doppler shift is smaller than the theoretically predicted value. The projected component of the mean wind velocity at a pertinent zenith angle ψ is proportional to $\sin\psi$, the echo scattered near the zenith direction always having a smaller Doppler shift. This reduces the estimated Doppler shift because the echo scattered from the zenith is generally stronger than that from the oblique direction. This effect, however, is emphasized for the cases with larger anisotropy factors and/or wider antenna beams as shown in Figure 2.14.

C. Spectral width

Figure 2.15 shows the relative error for spectral width estimation against the anisotropy factor for a beam directed to the zenith direction (ψ=0). The error is small for the narrow antenna beam, the situation being identically the same for the Doppler shift estimation. In the case where the wide beam is used, the error decreases as the anisotropy factor increases for the wide beams. This is also due to the stronger echo power scattered near the zenith direction.

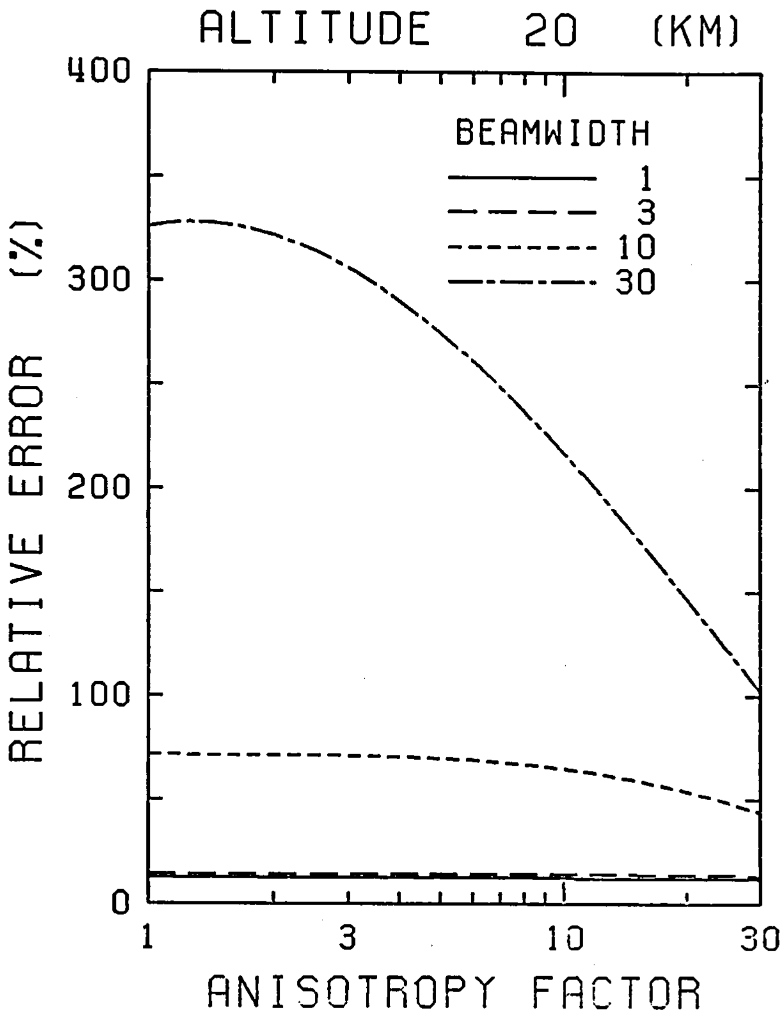

Figure 2.15. Spectral width estimation error versus anisotropy factor.

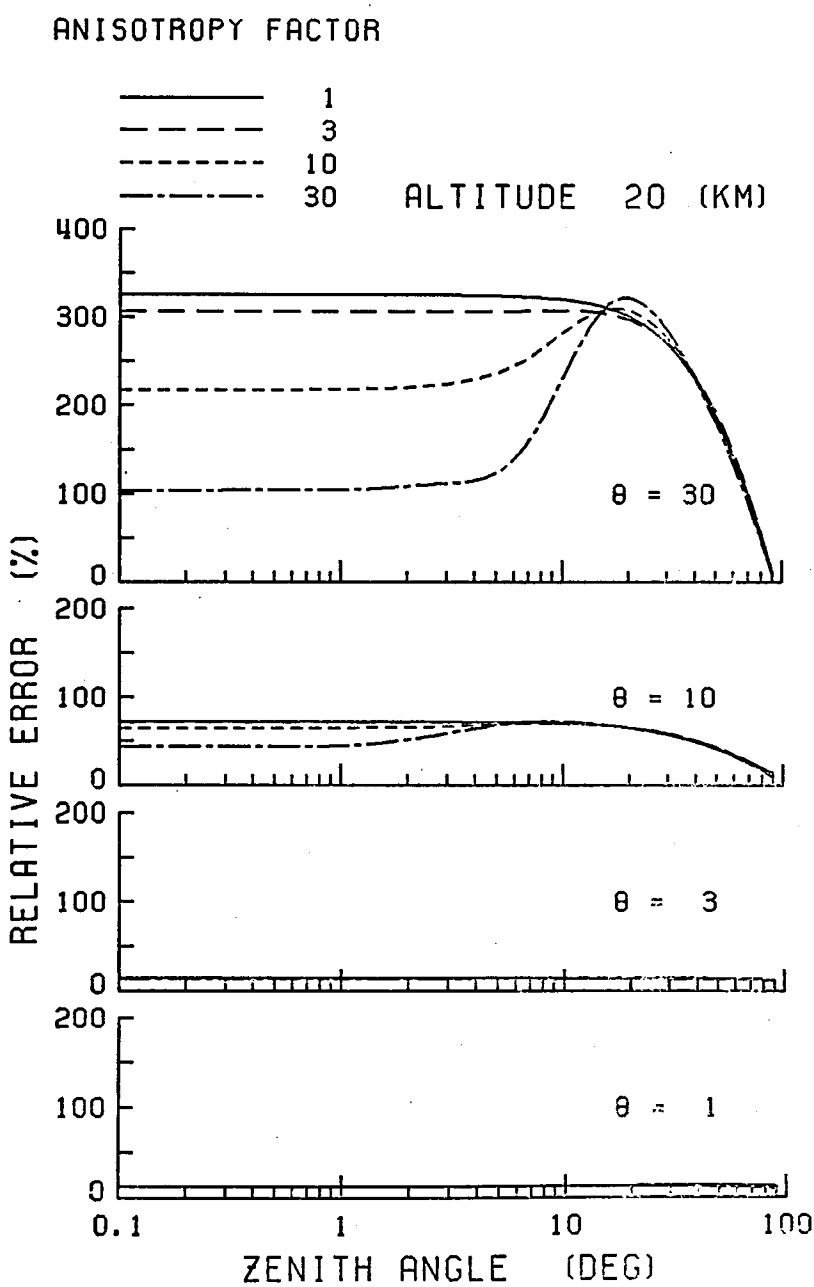

Figure 2.16. Spectral width estimation error versus zenith angle of antenna beams. θ = 1,3,10,30 are the antenna beamwidths in degrees.

Figure 2.16 shows the dependence of the relative error on the zenith angle for spectral width estimation. The humps, which is clearly seen for beamwidth 10° and 30°, are due to the first sidelobe echoes which are scattered from the zenith direction, thus widening the spectrum.

Chapter 3

JICAMARCA RADAR OBSERVATION OF THE MIDDLE ATMOSPHERE

3.1 INRTODUCTION

MST radar technique has made it possible to observe motions of the middle atmosphere. The equatorial region is abundant in various atmospheric waves, which behave very distinctly from those in other latitudes (Beer, 1978; Wallace, 1973). In this chapter, we present the observational results of the equatorial middle atmosphere using the Jicamarca VHF radar in Peru. The observations were made during September 1977 - January 1978. The objectives of the observations are to investigate 1) the scattering mechanisms, 2) the short period gravity waves and 3) the mean wind and long-period atmospheric waves.

3.2 JICAMARCA RADAR FACILITY

The Jicamarca Radio Observatory is located at latitude 12.0° south, longitude 76.9° west, about 30 km northeast of Lima, Peru. The radar was originally constructed by the National Bureau of

Standards, Boulder, Colorado, around 1960 in order to detect the incoherently scattered weak echoes by the ionospheric thermal electrons. The Geophysical Institute of Peru later acquired the radar.

Woodman and Guillén (1974) made the first sounding of the stratosphere and mesosphere, and showed a new application of the Jicamarca radar. It is one of the most powerful VHF radar in the world, however, some equipment-supply difficulties restrict system effectiveness. In this section we briefly describe the radar systems to show the observational capabilities and limitations.

3.2.1 Antenna system

The antenna consists of two superimposed arrays of 9216 half-wave (3 m) dipoles. The crossed-dipoles of the two arrays are arranged in the northwest and northeast directions. A group of 144 crossed-dipoles is called "module". The entire antenna is thus made up of 64 modules, forming a square of 290 meters. The beams may be pointed in various directions through the insertion of phasing cables between modules (Ochs, 1965).

Figure 3.1 shows an example of the switchyard connection. The outputs of two transmitter are split to feed quarters. The switchyard permits maximum flexibility in antenna utilization. It allows independent excitation of four quarters with each polarization. The antenna is thus capable of any desired

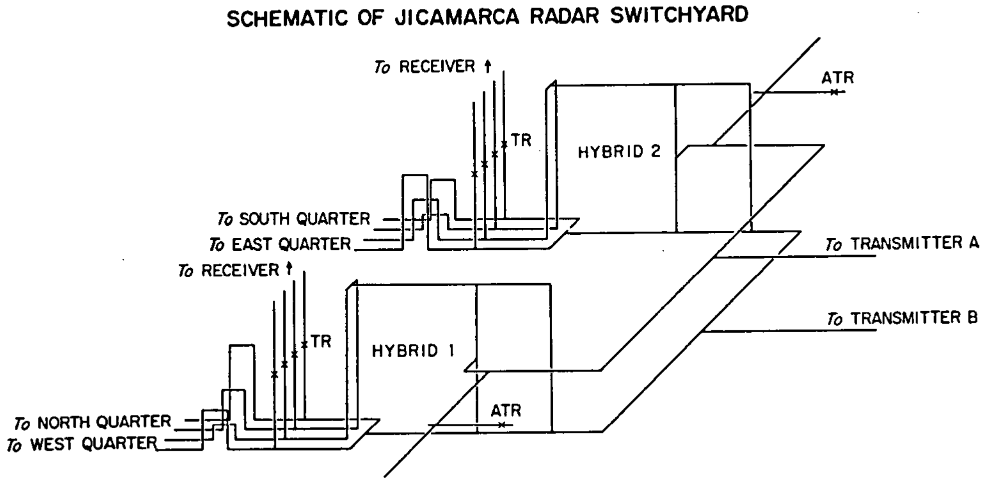

Figure 3.1. Schematic of Jicamarca radar switchyard.

polarizations. A set of spark gap TR-ATR switches isolates receivers from transmitters.

3.2.2 Transmitter and receiver systems

The transmitter system consists of four independent transmitters. Figure 3.2 shows a block diagram of the transmitter. A master oscillator generates a 0.9984 MHz signal. A 49.920 MHz RF signal (multiplied by 50) is amplified up to 1 MW peak power (nominal). A flip amplifier shifts the transmitted phase by 180°.

Figure 3.3 shows a block diagram of the receiver. A low-noise front-end circuit amplifies signals from the antenna. The receiver is dual conversion with a first intermediate

JICAMARCA TRANSMITTER SYSTEM

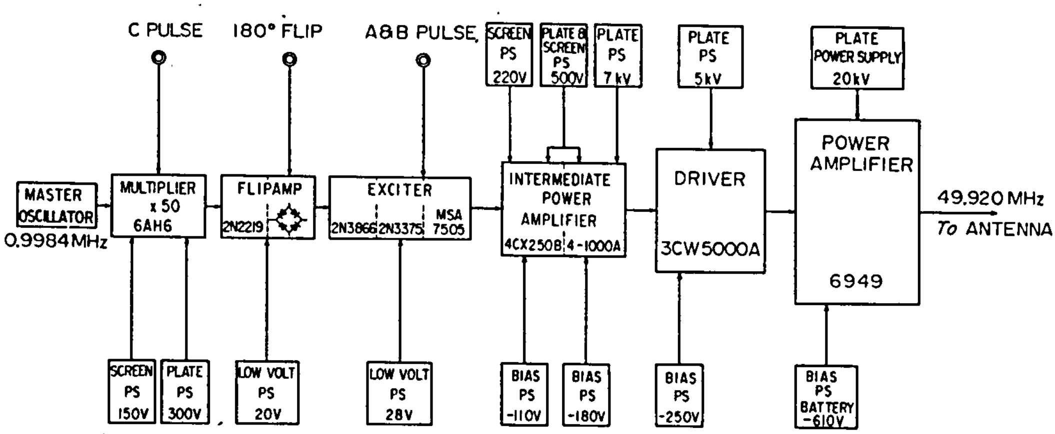

Figure 3.2. Block diagram of Jicamarca transmitter syetem.

JICAMARCA RECEIVER SYSTEM

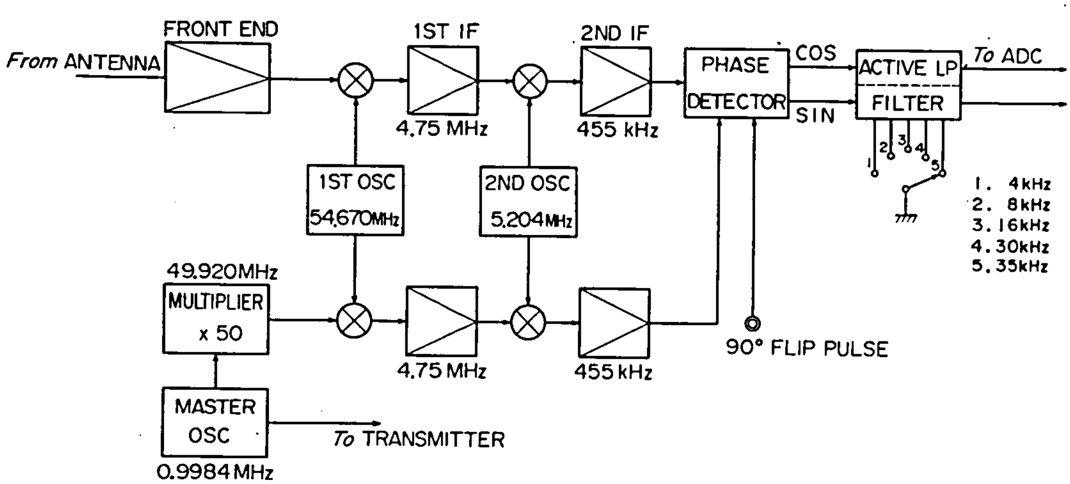

Figure 3.3. Block diagram of Jicamarca receiver syetem.

frequency (IF) of 4.75 MHz and a second IF of 455 kHz. With a 455 kHz reference signal, a phase detector produces in-phase and quadrature components. Low-pass active-filter circuits limit bandwidth of the receiver system. A 90° flip pulse rotates the phase of the reference signal by 90°.

3.2.3 Radar control system

Figure 3.4 shows a block diagram of the radar control and signal processing systems. The analog outputs of the phase detectors are fed into the sample-hold circuits. Through an

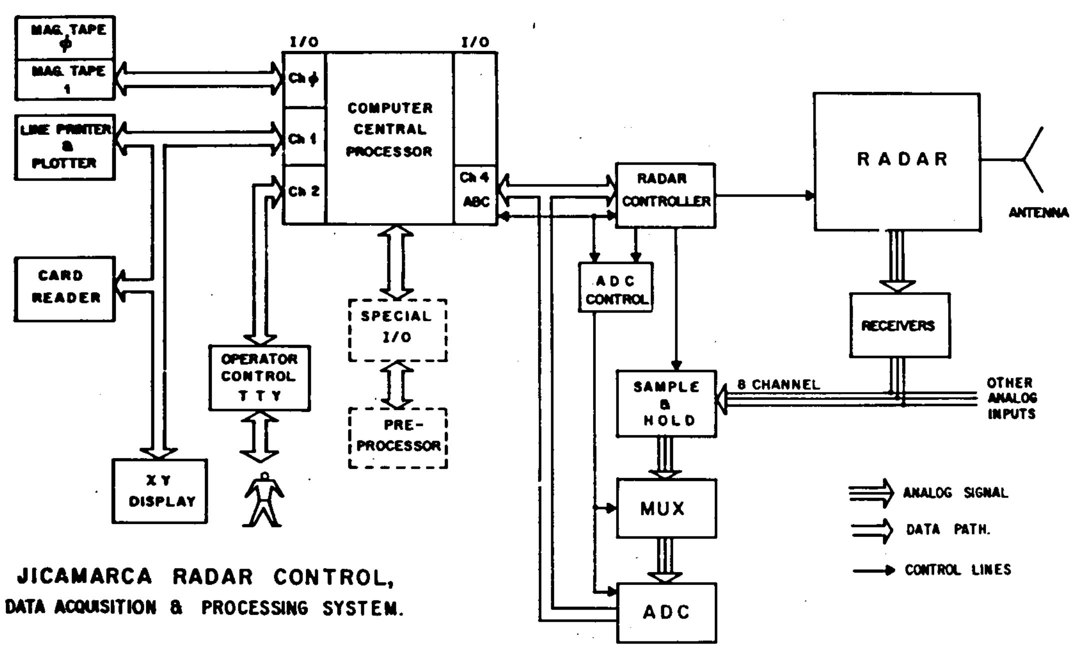

Figure 3.4. Block diagram of Jicamarca radar control system (Courtesy of Jicamarca Radio Observatory).

8-channel multiplexer, the signals are A/D converted and transferred to memory by the direct memory access I/O ports. During the September 1977 - January 1978 period, only four multiplexer channels were available, permitting simultaneous processing of only two receiver outputs. Data on memory are pre-processed (e.g., coherently integrated) and then stored on magnetic tape for later analysis. To real-time monitor the observation, estimates of echo power are sent to an X-Y display device.

The radar controller is a programable pulse generator, which produces the control pulses of the transmitter and the A/D converter. This controller consists of pulse-generate and rate-control sections, each of which contains 1024 shift registers (8 bits). The outputs of the pulse-generate shift register remains fixed for the period which is defined by the output of the rate-control shift register. The minimum period of transition is 5/3 microseconds, corresponding to the 600 kHz clock rate. Figure 3.5 shows an example of the radar controller outputs. Prepulse and TX pulse (A and B) turn on the multiplexer and the transmitter amplifier, respectively. The length of prepulse is about ten times longer than TX pulses to stabilize the 49.920 MHz RF signal. In order to minimize the systematic difference of phase detector outputs and to eliminate any system d.c. offset, 90° and 180° flip pulses are used respectively (Farley, 1965). Sample

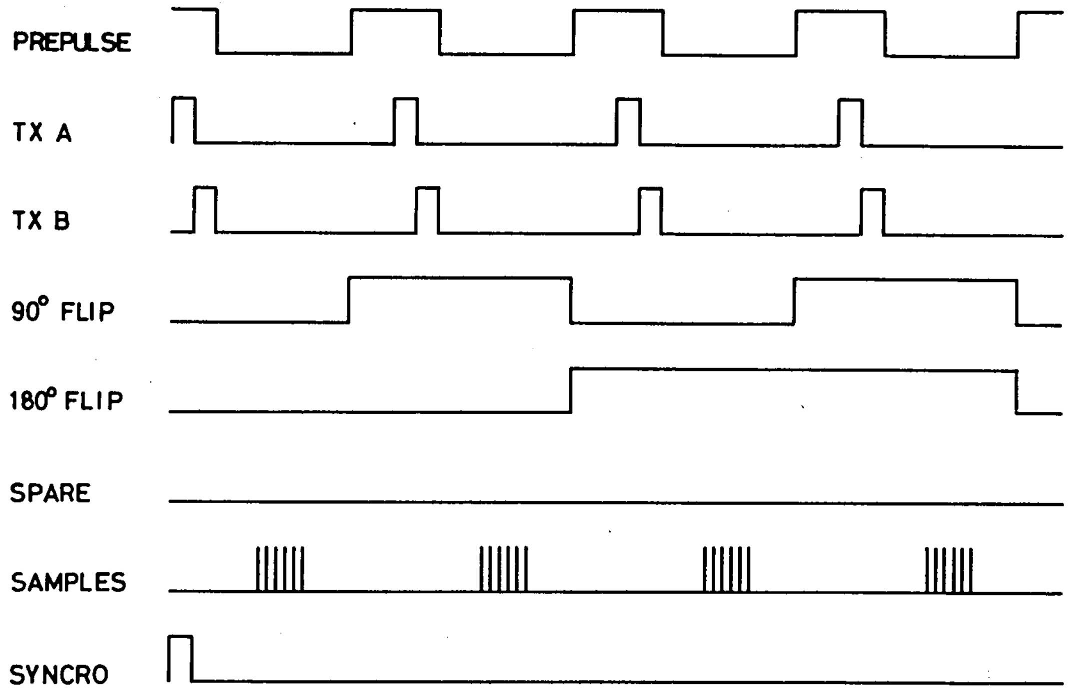

Figure 3.5. Schematic of Jicamarca radar controller outputs.

pulse controls the timing of the A/D conversion and syncro-pulse periodically restarts the controller to maintain computer syncronization.

3.3 SCATTERING POLARIZATION OBSERVATION

Turbulent scatter and Fresnel reflection have been generally used to explain radar echoes from the middle atmosphere. It is expected that the Fresnel reflection becomes more dominant with increasing wavelength (Balsley and Gage, 1980). Gage and Green (1978) reported some evidence of Fresnel (specular) reflection obtained with the 40 MHz radar at Sunset, concluding that the intensities of the vertical and oblique echo power were well correlated with atmospheric stabilities. Röttger and Vincent (1978) showed the difference between the two echoing mechanisms using spatial correlation measurements.

These results are based on the conventional monostatic VHF radar observation. Both radar frequency and polarization determine echo characteristics which, in turn, provide more direct means of studying atmospheric properties. Simultaneous multi-frequency radar measurements were made for the identification of clear radar echoes in the troposphere (Hardy and Katz, 1969). This technique may not, however, be practical for the middle atmosphere observation where high powers with large antenna apertures are needed. The study of echo polarization provides another way of investigating atmospheric properties.

In this chapter, we present a study of the echo characteristics of circular polarizations in the mesosphere and stratosphere (Wakasugi et al., 1980; Fukao et al., 1980d).

3.3.1 Scattering polarization properties

We first introduce the measures to describe the observation and summerize the characteristics of depolarization (Bickel, 1965; Long, 1975). Suppose that R and L distinguish the two orthogonal circular polarizations. Cmn (m,n = R or L) denotes the ratio of received to transmitted electric field strength. The first subscript denotes the transmitted polarization, and the second the received one. The circular polarization has the advantage in that the magnitude of the Cmn's is invariant to relative rotation about the radar line of sight. The radar cross section is proportional to the square of the field strength, i.e., $|Cmn|^2$. The total echo power P is defined as the sum of the amounts of power which are scattered back for any pair of pertinent polarizations. Thus

$$P = |C_{RR}|^2+|C_{RL}|^2+|C_{LR}|^2+|C_{LL}|^2 \qquad (3.1)$$

P is the trace of the polarization power scattering matrix (Graves, 1956). It is invariant with respect to the effects of Faraday rotation (Bickel and Bates, 1965) and to certain antenna errors (Bickel and Ormsby, 1965).

RR and LL components correspond to the depolarized echoes for circular polarization. Then the depolarization is defined as the ratio of the depolarized powers to the total echo power P,

$$D = (|C_{RR}|^2+|C_{LL}|^2)\ /P \qquad (3.2)$$

Each component in (3.1) and (3.2) can be expressed in terms of Aij's, which are the ratios of received and transmitted waves for linear polarizations (i,j = x or y; x and y designate two orthogonal linear polarizations):

$$|C_{RR}|^2 = |(Axx-Ayy)/2 + jAxy|^2 \qquad (3.3)$$

$$|C_{RL}|^2 = |(Axx+Ayy)/2|^2 \qquad (3.4)$$

$$|C_{LL}|^2 = |(Axx-Ayy)/2 - jAxy|^2 \qquad (3.5)$$

If reciprocity is assumed, Axy = Ayx and $C_{RL} = C_{LR}$. This assumption is adequate for monostatic backscatter radar (Berkowitz, 1965).

Bickel (1965) showed that the depolarization D gives an indication of the multiplicity of scattering centers, while the relative amplitude and phase of C_{RR} and C_{LL} implies a measure of target symmetry. The depolarization becomes zero (or $-\infty$ dB) for a target with a single symmetric scattering center such as a sphere, because RR and LL components are zero. For a long, thin dipole where the scattering region comprises a line, the depolarization becomes 1/2 (or -3 dB), i.e., $|C_{RR}|^2=|C_{RL}|^2=|C_{LR}|^2=|C_{LL}|^2$. The depolarization is, in general, less than 1/2 for an isolated scattering center. Long (1975) has discussed the relationships between linear and circular polarizations. Equations (3.3) and (3.5) imply that $|C_{RR}|^2$, $|C_{LL}|^2 \neq 0$ if $Axx \neq Ayy$ and/or $Axy \neq 0$. Then, the depolarization is expected to become larger than zero for targets having sharp edges (surfaces with radii compared with radar wavelength). For a large but smooth target compared with radar wavelength, Axx is nearly equal to Ayy, and the magnitude of Axy (or Ayx) is smaller than that of Axx (or Ayy). Then, $|C_{RR}|^2 \simeq |Axy|^2$, $|C_{RL}|^2 \simeq |Axx|^2$, and $|C_{LL}|^2 \simeq |Axy|^2$ are established. Therefore those targets should exhibit a smaller depolarization than those having sharp edges. It should be noted that the observed Aij's and Cmn's are random variables, and these models explain only the average structures of the targets.

A direct explanation of depolarization is to assume multiple scattering of radar waves. The circularity is reversed for each bounce, and any targets can produce significant depolarization if they cause the radar waves to be reflected twice or more (even numbered) times. This property has been used to reject weather clutter. But it is unlikely that VHF radar waves, which are scattered more than once, can be detected from the clear atmosphere (de Wolf,1975). Therefore, we exclude the effects of multiple scattering in the following.

3.3.2 Observational technique

The observation was made by using two independent transmit-receive systems for right and left circular polarizations. Various systematic errors as well as random noise, on which the accuracy of the experiment strongly depends, need to be carefully taken into consideration.

The antenna width is about 1°, and the beam was directed to the antenna on-axis position (tilted by an angle 1° from the zenith toward southwest). This minimizes the coupling of the two polarizations of the antenna and the effects of antenna sidelobe echoes. The coupling between the two polarizations is estimated to be the order of -25 dB (Farley, 1965).

The transmitted power, receiver gain, and antenna loss were not generally identical to each polarization. In order to estimate and compensate these differences, a pulse and sample scheme shown in Figure 3.6 was employed in the present experiment. Two separate transmitting systems, corresponding to the right and left polarization, excited the common array of the cross-dipoles. Echoes corresponding to each polarization were received and detected separately. The phase of transmitted pulses was alternately flipped by 180° for every pulses in order to eliminate the d.c. offset of the receiving systems. No pulses ,was transmitted at the fifth interpulse period (IPP). The sample during this interval was used to estimate the gain difference of the two receiving systems which then served to estimate the difference of the two transmitted powers. Because of the limitted data acquisition capability of the Jicamarca radar, the measurements of the mesosphere and the stratosphere were done

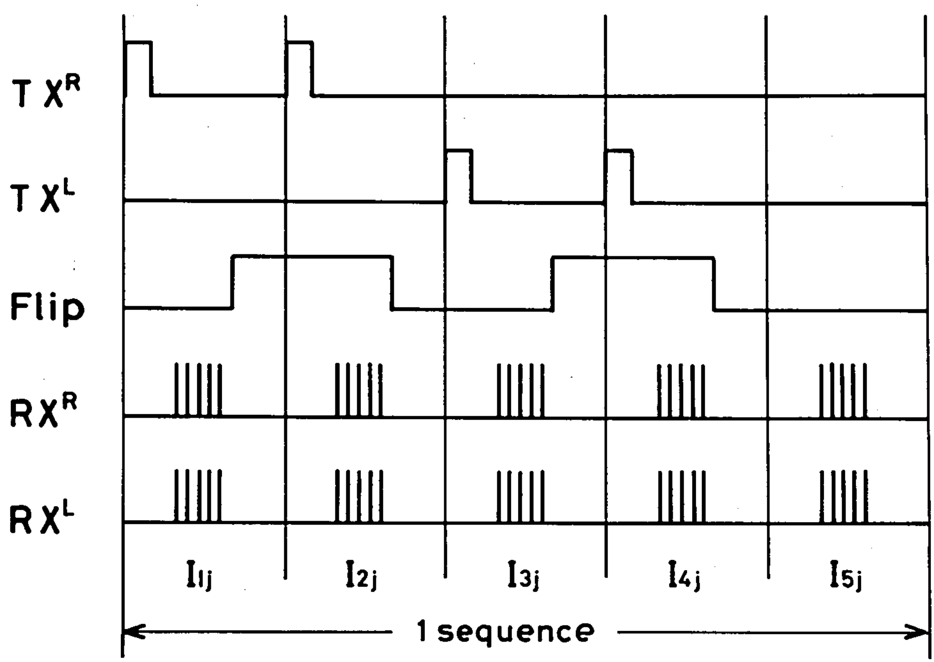

Figure 3.6. A sequence of pulses and samples. R (L) corresponds to the right (left) circular polarization. No TX pulse is transmitted at the fifth IPP for noise measurements. The pulse phase is flipped by 180° after every TX pulse.

Table 3.1. Parameters of polarization property measurement

Date and time	1210-1640 LT 27 December 1977	1710-2140 LT 27 December 1977
Height range	65.0-90.0 km	20.5-27.5 km
Height interval	2.5 km	1.75 km
Pulse duration	25 μs	20 μs

separately. Table 3.1 gives altitude and time parameters of these measurements. The pulse widths were 25, and 20 μs for the mesosphere and the stratosphere, respectively. The IPP was 893 μs for both measurements. At each altitudes the sampled signal was coherently integrated over 16 sequences (or 71.44 ms). Power, mean Doppler shift, and spectral width of echo signals were estimated every 15 s by using the revised maximum entropy method (Ogura and Yoshida, 1981). Data of echoes, of which the signal-to-noise ratios larger than 0.02 in the mesosphere and 0.2 in the stratosphere, were used; the bandwidth of the digital filter used was ±3.3 Hz.

The echo power was carefully examined in order to remove undesired non-atmospheric echoes from aircrafts and meteors, for which the Doppler shift, spectral width, and noise level show a very different behavior from those of atmospheric echoes. The transmitted power of right circular polarization is larger than that of the left circular polarization by 0.1 and 0.2 dB at the altitudes of 65.0-90.0 km and 20.5-27.5 km, respectively. Also, the corresponding receiver gain of right circular polarization is larger than that of left circular polarization by 1.0 and 0.1 dB for the respective altitudes. The differences of the transmitters and the receivers were compensated in the estimation of the total echo power P and the depolarization D. Noise was also estimated from the zero lag of the autocorrelation function of the echo signal and was compared with the noise estimated by the samples without the transmitter pulses. The gain difference of the two receiving systems was as large as 10 dB at altitudes below 20 km. This is due to the recovery effect of the spark gap TR-ATR switch of the radar.

3.3.3 Results and discussions

The statistical distribution of the echo power is of great importance for studying target properties (Nathanson, 1969). Figure 3.7 shows the histograms of the total echo power in the mesosphere and stratosphere. The abscissa is the normalized echo power, i.e., the ratio of the instantaneous echo power to the mean echo power. The ordinate is the relative frequency for every 0.2 increment of the normalized power. The smooth curves show the Ricean distribution matched in a least square sence. The curve is a function of q^2, which is the ratio of the constant echo power to

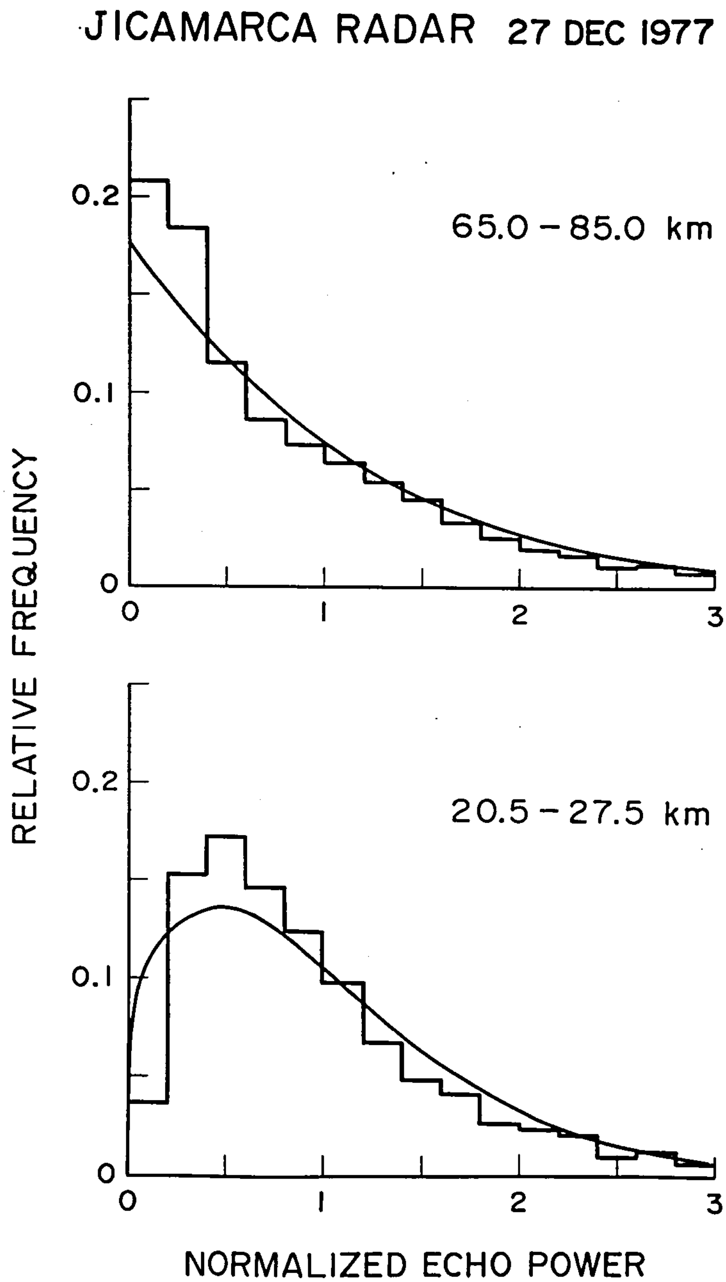

Figure 3.7. Histogram of the echo power. The echo power is normalized by the mean echo power at each altitude. The smooth curves show the Ricean distribution matched in a least mean square sence. The estimates of Ricean parameters are 2.0 and 0.5 in the stratosphere and mesosphere, respectively.

the fluctuating echo power. The large value of q^2 shows that the echoes are mainly due to steady targets. The estimates of q^2 in Figure 3.7 imply, on the average, 2.0 and 0.5 in the stratosphere and the mesosphere, respectively. The estimates of q^2 at each altitude vary from 2.0 to 3.0 in the stratosphere, decreasing with altitude from about 1.0 around 70 km to near zero around 85 km in the mesosphere.

Figure 3.8 shows the total echo power P and the depolarization D as a function of altitude. The depolarization is not plotted below 70 km in the mesosphere, where the average signal-to-noise ratio (SNR) of the RR and LL components falls below -10 dB. Above 80 km the SNR of the total echo power is smaller than that below 70 km, but the SNR of the RR and LL components becomes larger than -10 dB because the echoes are much more depolarized there. As is shown in Figure 3.8, the depolarization increases with altitude from -15 dB around 72.5 to about -8 dB at 85 km. A conspicuous difference is noticed between the altitudes above and below 80 km. The mean depolarization is -7.4 dB at the altitudes of 80-90 km, while it is -13.5 dB at the altitudes of 70-80 km. In the stratosphere the mean depolarization decreases to as small as -16.2 dB, a value which is smaller than that in the mesosphere.

The depolarization indicates a weak negative correlation with the total echo power. This correlation is more explicitly

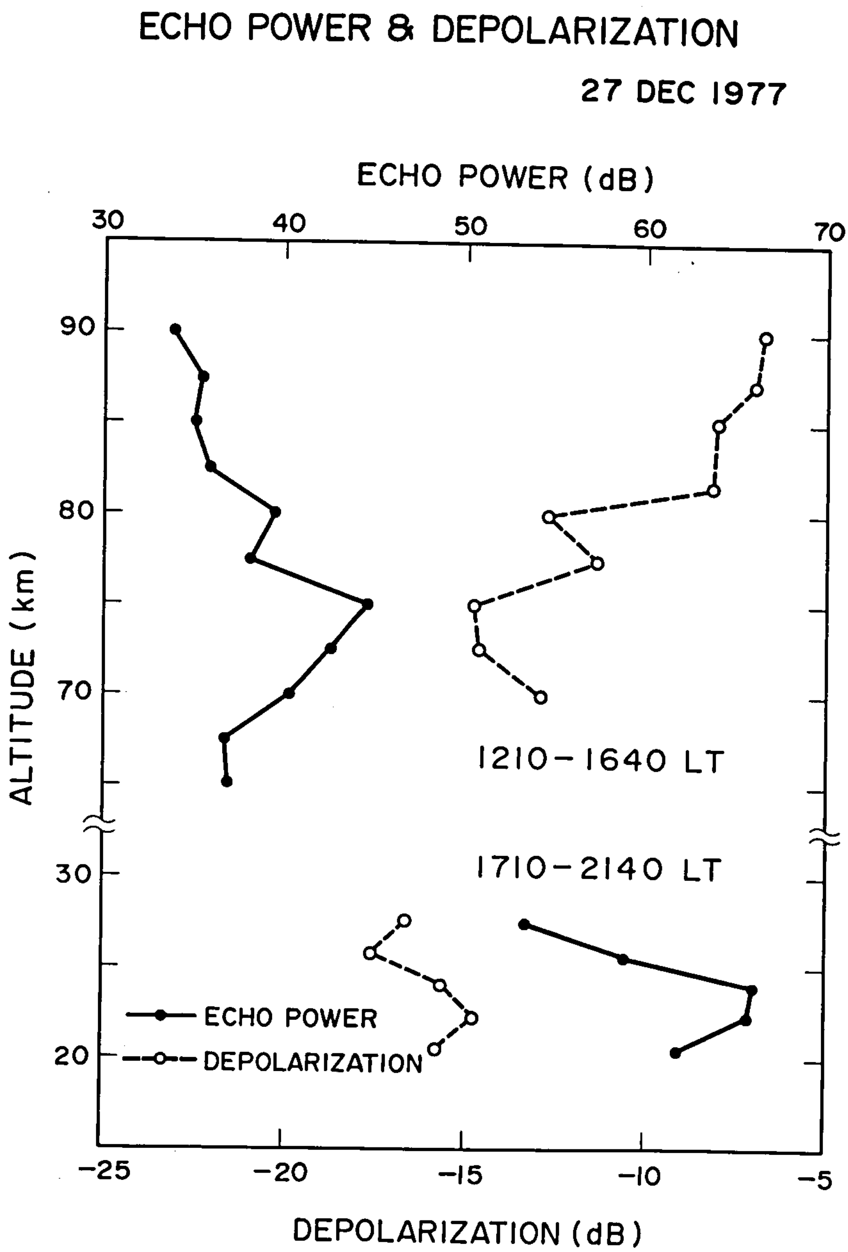

Figure 3.8. Mean total echo power and mean depolarization versus altitude. The echo power is relative power in decibels with an arbitrary reference level. The mean noise level is 38.1 dB. Values having the signal-to-noise ratio of each polarization component below -10 dB are omitted.

observed through a temporal variation at each altitude. There is a difference in the characteristic time of fluctuations between the echoes in the mesosphere and the stratosphere.

Figure 3.9 shows a diagram of the depolarization D against the total echo power P from 70 to 85 km. Each symbol indicates the data averaged over a 5-min period. No symbol is plotted if the number of data to be averaged is less than 30 % of the total number of data for the 5-min period. This figure shows a marked

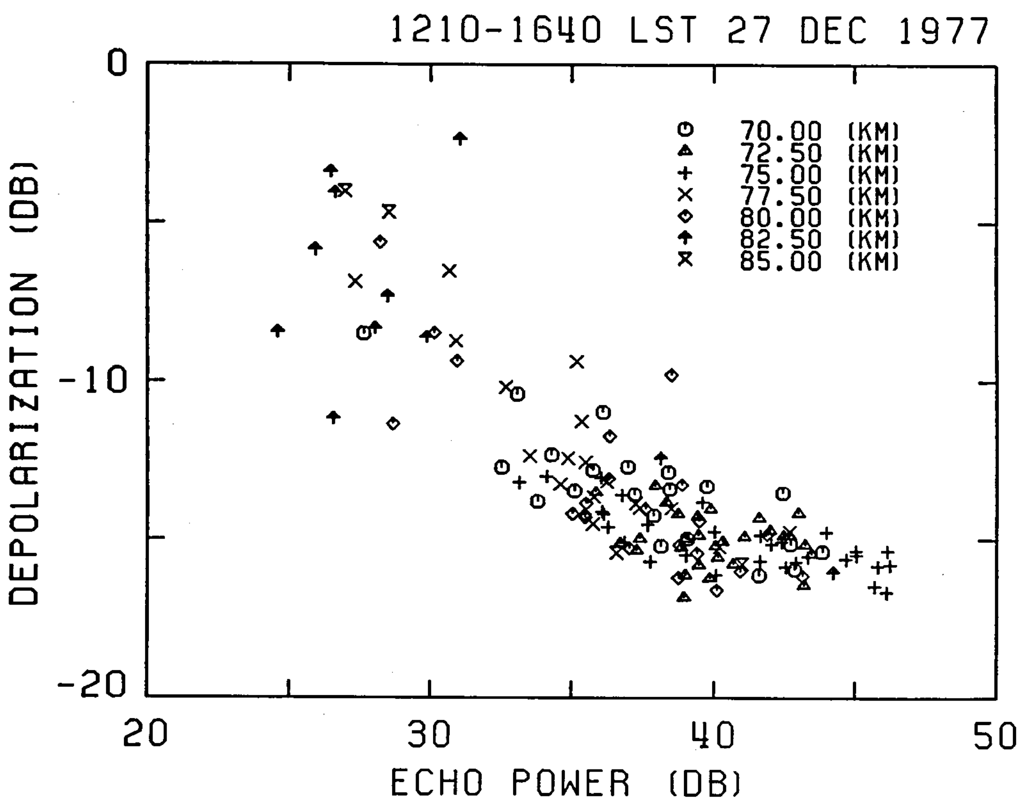

Figure 3.9. Diagram of the depolarization against the echo power in the mesosphere. The echo power is relative power in decibels with an arbitrary reference level. Each symbol shows the averaged value over 5 min.

negative correlation between the two parameters, especially in the altitude range of 70-80 km. The correlation weakens and the data tend to scatter in the altitudes above 80 km. The correlation of the echo power and the depolarization is found to have a life time of 10-30 min, which is consistent with the observation by Röttger et al. (1979).

Figure 3.10 shows the SNR of the echo power obtained at the altitude of 24 km as a function of time (5-min periods). Data are digitally smoothed by a low-pass filter with a bandwidth of ±1 Hz. This improves the SNR by a factor of 13 dB compared with the coherently integrated data. The temporal variations of the corresponding depolarization D is shown in the figure. The echo power of the RR and LL components are significantly larger than the noise level, even when the echo power tends to minimum. Thus since the weak echoes tend to occur with large depolarization, the SNR's of the RR and LL components become as large as the RL and LR components. On the average, the echo is stable in the stratosphere. The intermittent fluctuations of echo power have not occured with the period of about 10 min which is observed in the mesosphere. However, as shown in Figure 3.10, the echo power from the stratosphere varies by 10-30 dB within a period of several to several tens of seconds and shows a close negative correlation with the depolarization.

The antenna coupling between the right and the left circular polarizations seems to be a major systematic error that invalidates the results of the present observation. Because of the Jicamarca antenna configuration, no direct measurement of the coupling was made in our observation. The on-axis beam is expected to minimize the possible coupling. If the coupling were so large as to contaminate the RR and LL components, then a constant value of the depolarization might be expected, conforming to the antenna coupling. The results of the observation, however, show that the depolarization varied with both time and altitude. In addition to this, there is a difference in the period of the fluctuations between the mesosphere and the stratosphere. It could possibly be concluded that the coupling of -25 dB (Farley, 1965) may not be small enough for the derivation of the absolute

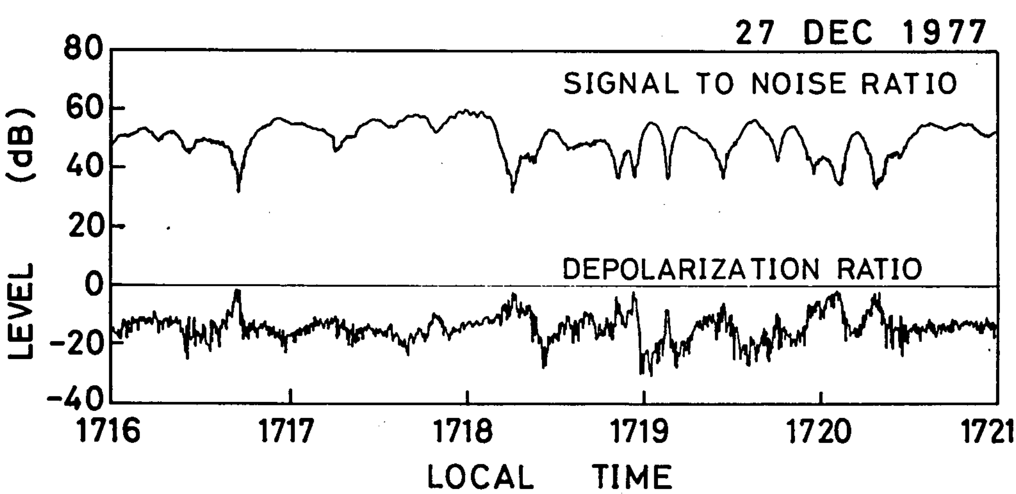

Figure 3.10. A typical temporal variation of the total echo power and the depolarization at the altitude of 24 km. Data are filtered with a bandwidth of 1.0 Hz.

value of the depolarization, but small enough in respect to the relative variation of the depolarization in the middle atmosphere.

The observational results suggest that two different mechanisms may contribute to scatterings from the mesosphere and the stratosphere. At the regions where strong echoes are received, the depolarization tends to become small. Stable structures with smooth surfaces are expected to have a small depolarization. The radar waves scattered by such structures are added coherently. Then the echo tends to become large and showsa strong aspect sensitivity. These targets seem to dominate the mesosphere of 70-80 km and the whole observed stratosphere as well. It is notable that the decrease of depolarization at the altitude of 80 km corresponds to a peak of the echo power at that altitude , suggesting the existence of a more stable structures. On the other hand, the large depolarization above 80 km suggests the existence of some small structures. In the regions of active turbulence the stable structures are destroyed by the turbulent motions, and the turbulent scatter is dominant there. The irregularities would become an ensemble of the small structures, producing a large depolarization. The echoes which are scattered from these diffusive and randomly distributed irregularities add less coherently to produce an echo power which is smaller than being added coherently.

Röttger et al. (1979) reported the difference of the turbulence structures between the altitudes above and below 70 km. Fukao et al. (1980b) also showed the scattering becomes more isotropic above 75 km in the tropical mesosphere, while Fresnel type reflection prevails below 75 km. The present finding, based on the depolarization observation, is consistent with these results. The transition height varies by 5-10 km. This is expected from day-to-day variations as seen from the echo power profiles (Fukao et al., 1980b).

We have discussed some properties of the received echo power corresponding to the zeroth-order spectral moment. Moments of the echo spectra with higher orders provide more information of the target properties. It has been shown that the depolarized echoes (RR and LL) are caused by turbulent scatter, while the polarized echoes (RL and LR) are expected to have the two components: the turbulent scatter component and the components reflected from stable structures. This suggests that there is a difference in the spectral width (or correlation time) between the depolarized and polarized echoes. If the echoes come mainly from a stable structure, a component having narrow spectral width (or long correlation time) dominates the polarized echoes. Then the ratio of the spectral width of the depolarized to the polarized echoes should become large. This ratio is found to decrease generally with increasing altitude. It varies from 9 around 70 km to about 2 at 85 km in the mesosphere. This suggests that the stable structures were broken into pieces by turbulence with increasing altitude. The ratio at the altitude of 80 km reaches a value as high as 9, where a small peak of the echo power and an abrupt decrease of the depolarization are observed. This also indicates the existence of a stable structure at the altitude of 80 km.

The extent of antenna beam and the wind shear broaden the spectral width of the echoes. These broadenings are different between the vertical and the oblique beams if echoes from turbulent and stable structures are separately obtained by using the two beams, which observe the different regions in case of a monostatic radar (e.g., Fukao et al., 1980b). In this respect, the present observation is better than observations using the vertical and oblique beams because the beams for both polarizations illuminate the same region, and the effect of the beam broadening and wind shear is identical for both polarizations.

The radar observation of the polarization characteristics provides a potentially useful means for studying the structures in the middle atmosphere. We have presented only the averaged properties of the echoes because of relatively poor altitude resolution attainable by the Jicamarca radar. Further improved observations are needed for understanding the detailed properties of the circular and/or linear polarization characteristics (Fukao et al., 1980e).

3.4 OBSERVATION OF SHORT PERIOD ATMOSPHERIC OSCILLATION

The MST radar technique is ideal for observing various dynamic processes, especially atmospheric waves on short time scales. A gravity wave with a period of a few minutes has been observed (Rüster et al., 1978; VanZandt et al., 1979; Fukao et al., 1979). These dynamic properties of the atmosphere are also concerned with scattering mechanisms of radio wave (e.g., Gossard and Hooke, 1975).

In this section, we concern the short-period atmospheric waves and related radio wave scattering observed at 13-25 km over Jicamarca. The observation was made at 1130-1540 LT on December 28, 1977. Attention is focused mainly on the tropopause that might demarcate the wave properties above and below it (Fukao et al., 1980c).

3.4.1 Observational technique

The Jicamarca antenna consists of the array of cross-dipoles, arranged in the northwest and northeast directions. For the present observation the whole antenna of the northwest dipoles is partitioned into four subarrays (Figure 3.11); the pair in the east (E) and west (W) quarters are used for transmission, while the other pair in the north (N) and south (S) quarters are for reception. Each antenna beam is about 1.7° wide at half-power width and tilted by an angle of 1.05° to the southwest (on-axis

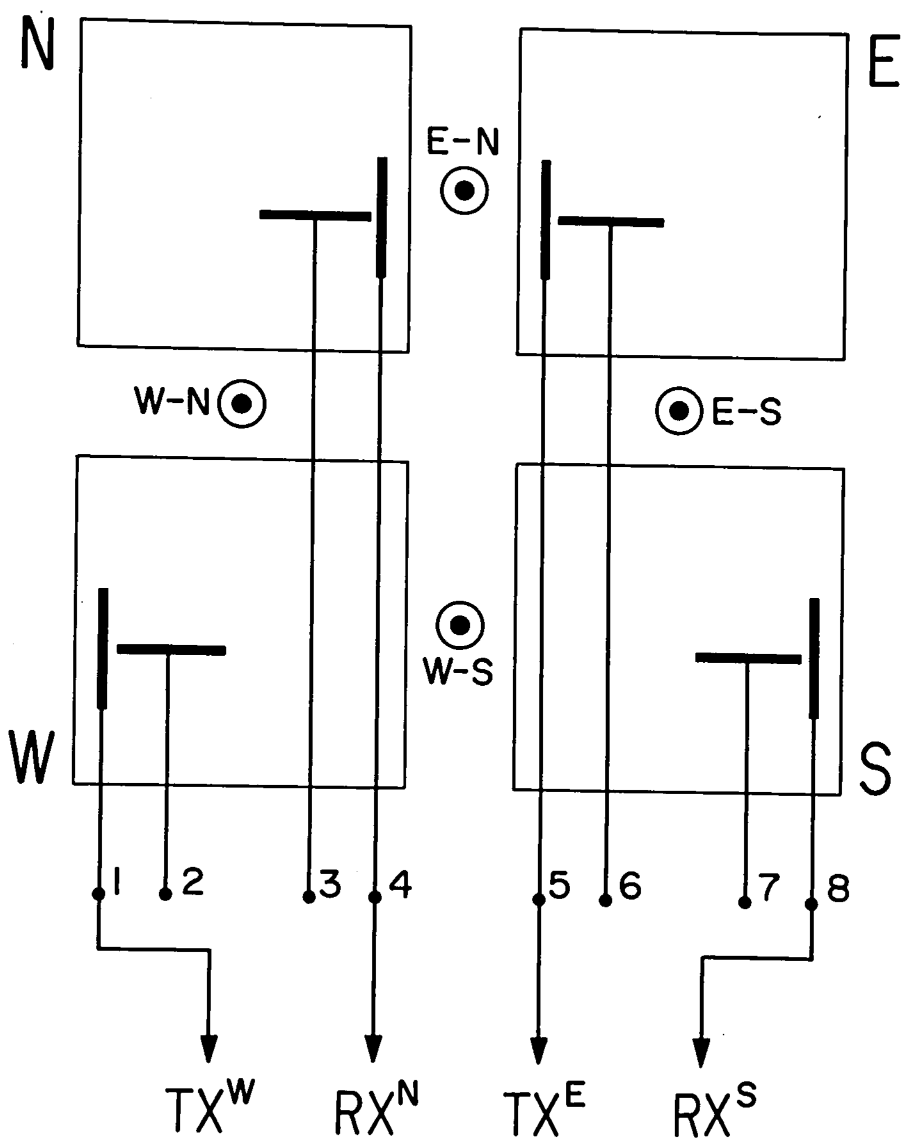

Figure 3.11. Observational setup of the Jicamarca antenna. Only the northwest dipiles are used. The east (E) and west (W) subarrays are connected to the transmitters (TX^E and TX^W), while the north (N) and south (S) subarrays are connected to the receivers (RX^N and RX^S). The location of the scattering centers is shown by solid dots inside circles.

antenna position, without phasing). A pair of transmitting and receiving beams form a scattering region; four scattering regions are generated in the present observational setup. The horizontal extent of each scattering region is about 500 m at the altitude of 20 km, while the separation between the adjacent scattering centers is 100 m irrespective of height. A similar observational setup is employed by Rüster and Woodman (1976), but in their case, only the west subarray is used for transmission, while the remaining three subarrays are used for reception.

Pulses of approximately 20-μs width at 1 MW peak power (nominal) are transmitted alternately on the east and west subarrays with an interpulse period of 893 μs. The returned signals, received simultaneously on both north and south subarrays, are range gated every 2 km at the 7 altitudes in the 13- to 25-km region. The equivalent altitude resolution (two-way) is about 2.5 km. It should be noted that the signals at adjacent altitudes are not completely independent of each other for the 20-μs pulses. No TR-ATR switch is used, since the isolation between adjacent subarrays is better than -70 dB (Ochs, 1965). By doing this the receiver recovery effect is avoided, enabling a more precise observation in the lower altitudes to be made.

The coherently detected signal is digitally filtered through 71.44 ms. The filtered samples are averaged over 15 s for the determination of the d.c. component that needs to be subtracted from each sample. The d.c. component seems to be fairly stable, since no appreciable change is noted, even if the average over the periods other than 15 s are used. The 210 samples thus obtained in 15 s are then used for calculating a complex autocorrelation function (ACF). Twenty-nine time lags (including the zero lag) are calculated, giving a maximum time lag of 2 s. Since the signal correlation time is relatively long, the signal power is readily estimated at the zero time lag by extrapolating the values at the neighboring time lags. Power spectra are then estimated from the calculated ACF's by an revised maximum entropy method (Ogura and Yoshida, 1981) so as to evaluate the Doppler shift and the spectral width. The length of the prediction filter chosen is unity, since it is shown from an analysis with the periodogram method that most of the spectra are singly peaked. In this case the inferred spectra become Lorentzian, and a signal correlation time defined as the time lag to 0.5 correlation τ_H(s) corresponds to the half-power width of f_H (Hz) via $\tau_H = \ln 2(\pi f_H)$.

3.4.2 Scattering characteristics

One possible way to identify types of scattering is to study the correlation between the echo power and signal correlation time (Röttger and Liu, 1978; Gage and Green, 1979; Fukao <u>et al.</u>, 1980b). If the echo is due to turbulent scatter, the stronger the echo power, the shorter the signal correlation time should be. On the other hand, if the echo comes from stable structures, the increase in signal correlation time should generally be observed to occur along with the increase in echo power.

To appreciate this, mean profiles of the echo power and signal correlation time observed by the west and south subarrays (west-south region; see Figure 3.11) are shown in Figure 3.12, together with their correlation at the respective altitudes. Each dot on the right of Figure 3.12 indicates the value inferred from an average of two of the 15-s spectra. No significant difference is noted even if any other pair of subarrays are used. As was mentioned above, the antenna beam is tilted by 1.05°, but the zenith direction falls within the main beam.

It is clear from the left of Figure 3.12 that there is a marked positive correlation between the mean echo power and the mean signal correlation time present; the larger echo power corresponds to the larger signal correlation time. On the right of Figure 3.12, there are trends of positive correlation between the instantaneous values of the two parameters in the altitude range considered except for 17 and 19 km. This suggests that the Fresnel type reflection from stable structures is relatively dominant over the turbulent scatter, both in the upper troposphere and in the lower stratosphere, i.e., the regions with high reflectivity are, on the average, horizontally stratified. On the other hand, no correlation is observed at the 17- to 19-km region,

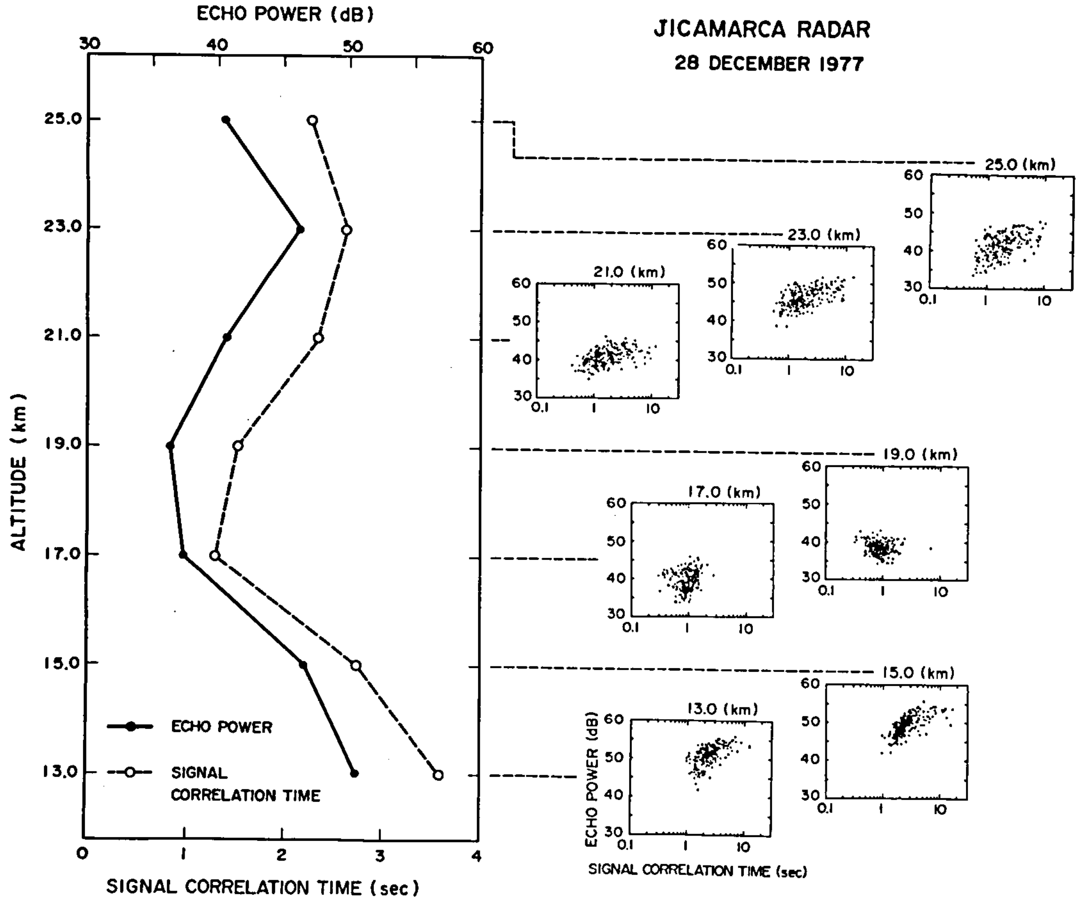

Figure 3.12. (Left) Mean profiles of the echo power (solid curve) and signal correlation time (broken curve) in the 13- to 25-km region. Data shown are averaged values over 1130-1540 LT on December 28, 1977. (Right) The correlation between the echo power and the signal correlation time at the respective altitudes. They are inferred from the average of two of the 15-s spectra observed in the period of 1400-1540 LT. The echo power is relative power in decibels with an arbitrary reference level.

and both the echo power and signal correlation time are relatively small there. As is shown later, there is a vertical shear of the horizontal wind in the 15- to 19-km region. It could be suggested that this shear might allow a turbulence to occur in the altitude range of 17-19 km, tending to destroy the stratified structures of high reflectivity to smaller patches. This may weaken the positive correlation between the echo power and the signal correlation time at these two altitudes as is shown in Figure 3.12.

However, it should also be noted that the partial reflection seems to be very highly aspect sensitive and that the beam direction is offset from the zenith by an angle of 1.05°. Thus we could not rule out the possibility that thin stratified structures with extremely enhanced reflectivity exist around the 17- to 19-km region. and these reflect the incident wave to the mirror direction partially, as noted at the mid-latitude troposphere (Gage and Green, 1978, 1979).

3.4.3 Short-period atmospheric oscillations

Dynamic properties of the atmosphere are partly determined by mean wind structures. Figure 3.13 shows the mean radial velocities averaged over four scattering regions. The observed radial velocities are much larger than the vertical velocities that are reported to be of the order of 1 cm s^{-1} by other

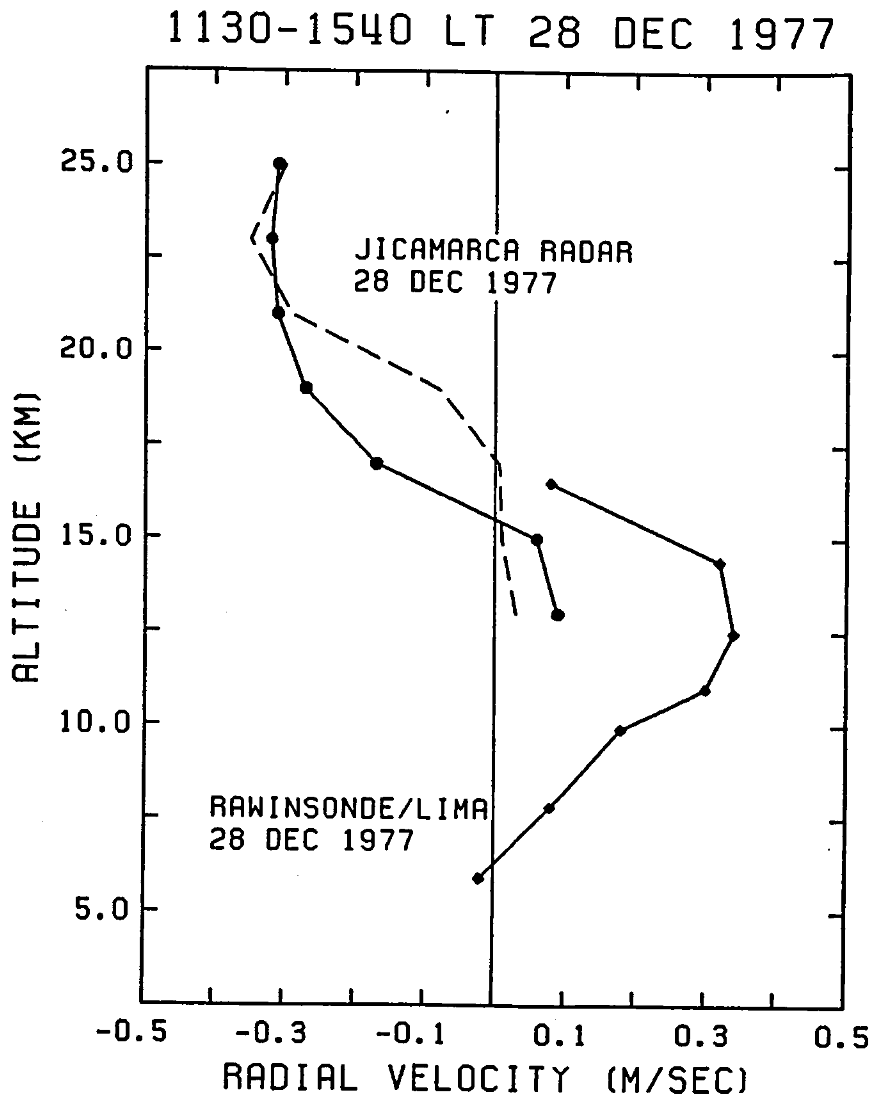

Figure 3.13. Mean radial velocities obtained by the Jicamarca radar (averaged values over the period of 1130-1540 LT) and by a rawinsonde launched at 1830 LT on December 28, 1977. The upward wind is chosen to be positive. Included in the figure is the radial velocity profiles (broken curve) inferred from the phase lag of radial velocities between adjacent scattering regions.

Jicamarca observations (e.g., Fukao et al., 1978). Hence they are assumed to be virtually the projected NE-SW component of the horizontal winds. Also included in the figure is a profile determined by the routine rawinsonde observation made at Lima/Callao at 1830 LT on the same day.

The profiles show general continuity in the overlapped region, although a slight altitude defference of about 2 km, between the radar- and the rawinsonde-inferred winds, appears. This difference is also noticed in the simultaneous observation with rawinsonde, which will be discussed in the next section. The magnitude of wind shear noted in the 15- to 19-km region in the antenna beam direction is about 0.08 $m\ s^{-1}\ km^{-1}$, corresponding to a horizontal wind shear of 5 $m\ s^{-1}\ km^{-1}$. The wind above 21 km seems to be roughly constant with altitude, the equivalent southwest wind being about 18 $m\ s^{-1}$. The overall altitude profile inferred by the present observation coincides well with the results of the December 6-8 observation.

Figure 3.14 shows the temporal variation of radial velocity at each altitude. In order to remove random fluctuating components the velocity data estimated every 15 s are smoothed by a low-pass numerical filter with a cuttoff period of 3 min. This figure suggests that the dominant periodicity as well as the amplitude of the short-period oscillations changes with altitude. In the region below 17 km there appears the evidence of an

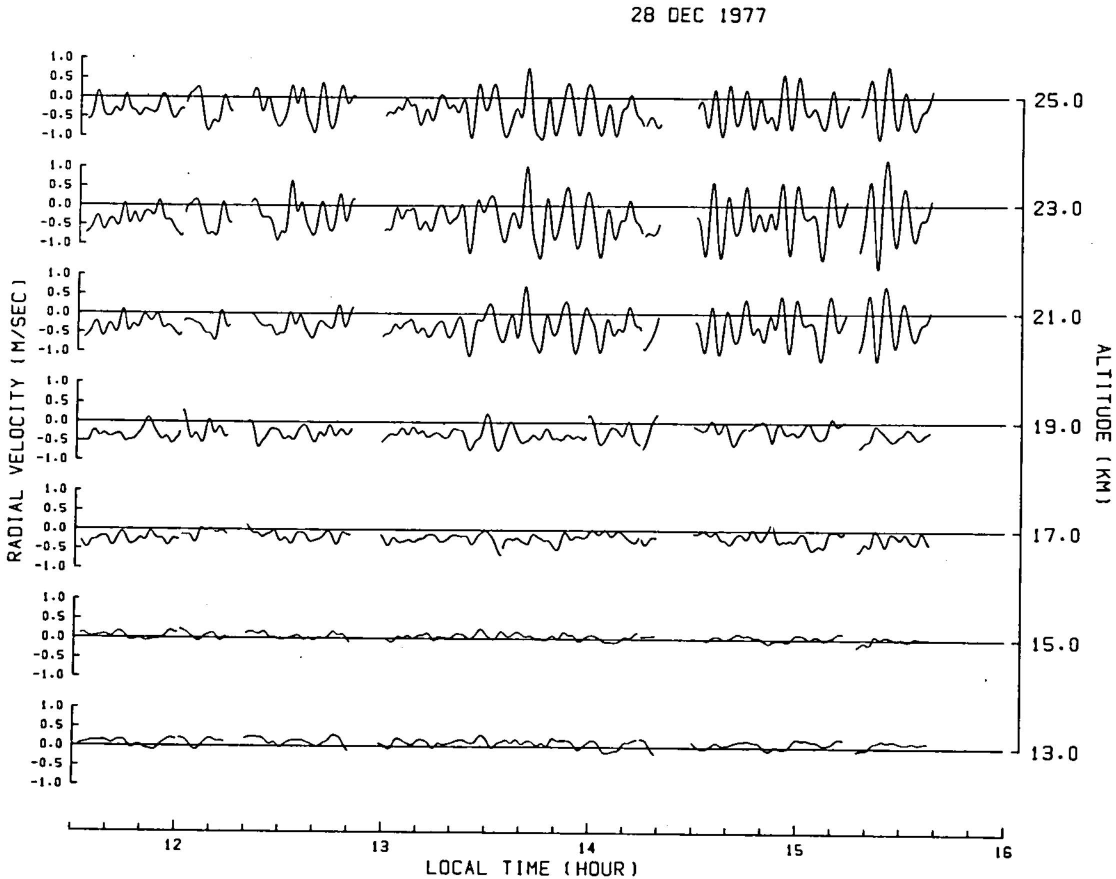

Figure 3.14. Temporal variation of the radial velocity (upward positive) observed in the east-south region.

approximate 10-min-period oscillation with a small amplitude of the order of 0.1 m s^{-1}. On the other hand, a marked velocity oscillation having a period of several minutes and a relatively large amplitude of 1 m s^{-1} predominates in the region above 21 km.

This is confirmed by Figure 3.15, which shows the power spectra of the velocity oscillation estimated by the Blackman-Tukey method. Note that the spectral density is given in decibels with a relative reference level, so as to cover the whole altitude range considered. It is clear that the most dominant periodicity changes significantly between above and below the 17-19 km region, around where the tropopause in the tropical region seems to exist (e.g., Gossard and Hooke, 1975). The periodicity is approximately 5 min in the 21- to 25-km region, whereas about 11 min in the 13- to 15-km region.

Figure 3.15 also indicates the coexistence of 10- to 12-min-period oscillations in the region above 19 km. It is suggested that these oscillations may be related to the tropospheric 11-min oscillation, however, they show no consistent height variations of amplitude and phase that indicate their vertical propagation through the troposphere.

The spectra obtained at 17 and 19 km seem to be spread over a wide frequency range. This confirms the conjecture that the wind field is relatively turbulent at these two altitudes.

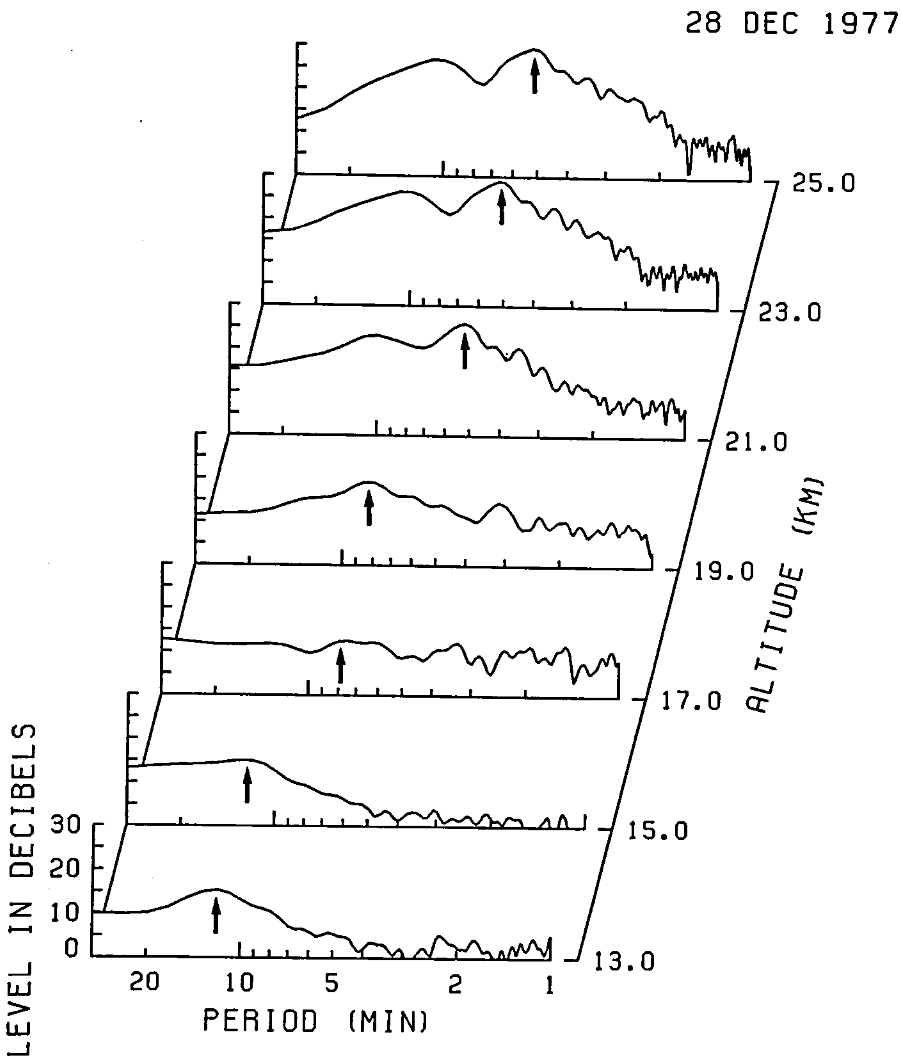

Figure 3.15. Power spectra of radial velocities in the whole observation period obtained in west-north region. The most dominant periods are indicated by heavy arrows.

3.4.4. Discussions

For the tropical atmosphere, the potential temperature is approximately 350 K at 15 km and 500 K at 20 km, giving Brunt-Väisälä periods of 9 and 4 minutes, respectively (e.g., Gossard and Hooke, 1975). The observational results suggest that dominant periodicities are very near the Brunt-Väisälä periods in the respective atmosphere. These oscillations can not be readily concluded to be the actual Brunt-Väisälä oscillation, however, without considering Doppler shift due to the background flow. Intrinsic frequency, or the wave frequency relative to the background flow, will become considerably different from an apparent frequency observed by a ground-based radar, in case the Doppler shift is large. Brunt-Väisälä oscillations coherently excited by a stationary source of scale L are Doppler-shifted by V/L Hz in a flow of speed V. The Doppler shift is negligibly small if $T_B \ll L/V$ where T_B is the Brunt-Väisälä period. Since the observed values of V are about 20 m s^{-1} and T_B is around 300-600 s, the Brunt-Väisälä oscillation excited on a scale much larger than 5-10 km would not be significantly influenced by Doppler shift.

These buoyancy oscillations have a 'deep wave' structure of the short horizontal wavelength when compared with the vertical wavelength (Hines, 1960). Fukao *et al.* (1981a) reported that in the lower stratosphere the distance of correlation appears to be less than the order of 1 km in the horizontal direction, while it is more than 5 km in the vertical direction.

Among radial velocities observed in the four scattering regions, appreciable phase differences are often observed. In the following, the phase difference associated with the horizontal variation of the buoyancy oscillation is discussed.

First, radial velocities are reestimated in every 5 s with the aforementioned procedure. Then, cross correlations between two different scattering regions are computed every 15 s based on data over consecutive 4-min intervals. The correlation coefficient and phase (or time lag) are determined by matching a polynomial of degree 2, in a least mean square sence, to the computed cross correlation. Data with a correlation coefficient estimated to be less than 0.7 are omitted. The time window of 4 min is so short that the phases in different wave packets which are visible in Figure 3.14 do not cancel each other.

A typical temporal variation of the phase is shown in Figure 3.16, given in the time lag of the radial velocity in the east-north region measured from that in the east-south region. These two scattering regions are aligned north and south so that a positive time lag corresponds to the northward phase trace speed, i.e., the horizontal speed with which the planes of constant phase move northward. As is shown in Figure 3.16, an appreciable phase difference, one that varies with time, is generally noticed among different beams.

The phase variation shown in Figure 3.16 is slightly different among different altitudes. This might be due to propagating internal gravity waves observed by Rüster et al. (1978) in the lower stratosphere and Miller et al. (1978) in the mesosphere. The time lags thus determined at the four scattering regions can be used to estimate horizontal phase trace speed at each altitude. The broken curve in Figure 3.13 is a projection onto the beam direction of the mean of the phase trace speed thus determined. A fairly good coincidence between the mean Doppler (solid curve) and the mean phase trace (broken curve) speeds is

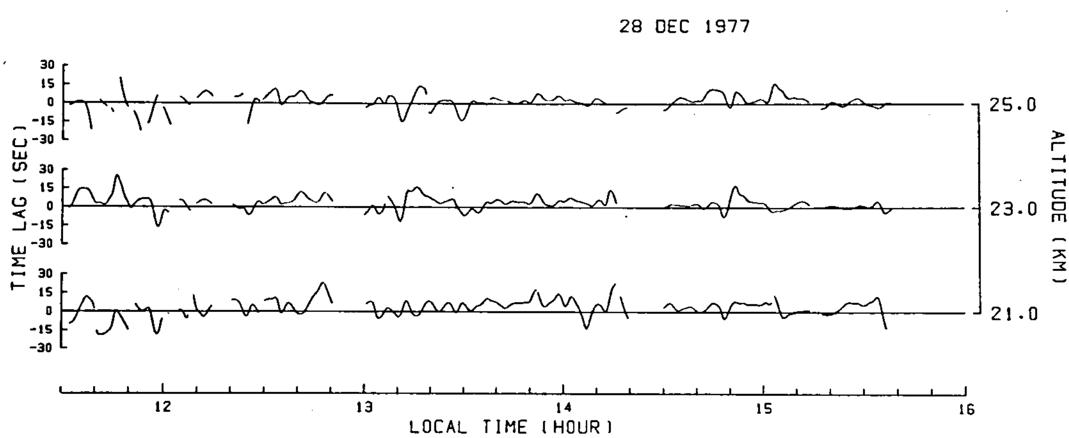

Figure 3.16. Temporal variation of the time lags of the radial velocities observed in the east-north and west-south regions. Positive time lag corresponds to the northward velocity.

found at the whole altitude except for the 17- to 19-km region. This could possibly indicate that the dominant buoyancy oscillations are, on the average, convected with the mean horizontal wind. The difference noted at 17 and 19 km might be caused by the turbulent velocity fluctuations, the horizontal scale of which is suggested to be less than 100 m.

The spatial coherence of the echo power provides a clue to structures of the regions with high reflectivity. It is known that the scattering from the lower troposphere have a good spatial coherence for a horizontal distance as large as a few tens of meters (Röttger and Vincent, 1978). In the present observational setup, the cross-correlation analysis of the echo power yields the mean correlation that increases from about 0.2 at 13 km to 0.6 at 25 km. Thus horizontal distances of the spatial coherence at these altitudes seems to lie, on the average, in the range of a few tens of meters to near 100 m, but has to be precisely conformed in future observations.

3.5 MEAN WIND AND TIDAL WAVE OBSERVATIONS

High-power radars can continuously measure middle atmospheric wind systems and waves on various time scales. Fukao et al. (1978) discussed stratospheric winds observed by the Jicamarca radar during a 24-hour period on 23-24 May 1974. The mean wind field measured at that time is similar to the monthly mean winds determined by rawinsondes launched from the Lima-Callao airport. A 1-5 m s^{-1} diurnal oscillation of the zonal wind was observed with downward phase progression. The amplitude of this oscillation is several times larger than that of the theoretical solar diurnal migrating tide, but oscillations of this order are expected from non-migrating diurnal tides (e.g., Wallace and Tadd, 1974).

In this section, we present observational results of mean wind and tidal oscillations. We discuss two sets of data obained at Jicamarca on 3-4 October and 6-8 December 1977. During the course of these observations, the shear zone marking the leading edge of the westerly regime of the quasi-biennial wind oscillation is expected to descend to around 20-25 km (I. Hirota, private communication). Radar-determined winds will be compared with winds obtained by simultaneous rawinsonde measurements (Fukao _et al._, 1981a).

3.5.1 Observational technique

In order to obtain the vector components of the wind velocity, the entire antenna is divided into three separate sections. A full aperture of one of the two arrays is used on the vertical beam, while two half apertures of the other array are assigned to the westward and southward beams, respectively. These off-vertical beams have zenith angles of 3.45°. The vertical beam used in the 1974 experiment has been shown to be offset from true zenith by 0.36° and, consequently, the inferred vertical velocities seem to be significantly contaminated by horizontal winds (Fukao _et al._, 1978). Fleisch (1976) adjusted the vertical beam to within 0.01° of the zenith, on the basis of theoretical calculations and radio source calibrations (Fleisch, 1980). This adjustment improves considerably the accuracy of both the horizontal and vertical velocities.

During the expedition, only four multiplexer channels that permit simultaneous processing of only two receiver outputs are available. The outputs of receivers for the westward and southward beams are therefore alternately switched on every 28 ms through a coaxial relay. Taking the switching time into consideration, the number of samples available in each of the off-vertical beams is less than a half of that of the vertical beam. Consequently, the overall detectability of the off-vertical beam is 9 dB inferior to that of the vertical beam.

Altitude and time parameters of the current observations are given in Table 3.2. The data discussed here are taken from an altitude range of 20 to 33 km. Below this range the data appears seriously affected by ground clutter and receiver recovery effects, while above 33 km the signal falls below the noise level. Spread-F irregularities are on occasion sufficiently active so as to contaminate the stratospheric echoes, as at 19-21 LT on 6

Table 3.2. Parameters of the stratospheric wind observation

Date and time	11 LT 3 October- 11 LT 4 October 1977*	12 LT 6 December- 12 LT 8 December 1977
Height range	21.0-33.0 km	20.0-32.5 km
Height interval	3.0 km	2.5 km
Integration time	0.25 s	0.44 s

*Fragmentary data are available in the period from 17 LT on 4 October to 10 LT on 5 October 1977.

December and from 19 LT on 7 December to 01 LT on 8 December. No wind velocities are available during these times. Systematic malfunctions prevented operation of the radar from 03 to 08 LT on 8 December. Similarly, a planned second day of the October observation was limited by multiplexer failure to fragmentary data of 1-2 hours after 07 LT on 4 October 1977.

Wind velocities are obtained through the following procedure. First, the autocorrelation function (ACF) is calculated approximately once per minute from 160 (or 256) coherently integrated samples for the December (or October) observation. The ACF is then weighted with a Hamming window function and transformed by FFT to yield the corresponding power spectrum.

Finally, the mean Doppler shift or radial velocity is determined through a calculation of the first moment of the power spectrum. Three radial velocities thus estimated are combined to give three orthogonal components of wind velocity: zonal (eastward), meridional (northward) and vertical (upward).

Extents of ground-clutter contamination considerably vary between the vertical and off-vertical beams. The contamination is not so serious in the vertical beam with relatively low sidelobe levels, and it can readily be eliminated by subtracting d.c. bias of the coherently integrated samples. On the other hand, the case is quite different for the off-vertical beams that they make a sacrifice of the low sidelobe levels in order to tilt the respective beam positions of half aperture arrays. Echoes received from the off-vertical beams are thus significantly clutter-contaminated, and that needs more sophisticated processing for removal. Therefore, the clutter contaminating off-vertical echoes is removed after the power spectrum is estimated. The clutter spectral component is expected to be symmetrical about zero Doppler shift (or the transmit frequency), and hence the easiest way for its elimination may be to remove the symmetrical portion of the power specrtum. Since in practice it is distorted by statistical or random fluctuations, some averaging of spectra is needed to reduce the fluctuations to acceptable levels. In the present analysis, 25 spectra (about 30 minutes) are averaged before the symmetrical portions of the spectra (clutter and sky noise) are removed. Radial velocities thus determined approximately every 30 minutes will be used for the analysis of mean winds and tidal oscillations in the following sections.

It should be noted that the removal of the symmetrical portion of the spectrum also removes some of the signal component, particularly when the mean Doppler shift is small. The error induced in the velocity estimation is negligible provided the mean Doppler shift (d) is larger than the half-power spectral width (w). As d becomes smaller than w, the error increases to 20% for d=0.5w and 50% for d=0.36w.

3.5.2 Mean wind

Mean profiles of the zonal, meridional and vertical wind velocities are obtained by averaging over the entire period of a given observation (Figures 3.17a-c). Three features of interest are: (1) The westerly which dominates the zonal wind near 25-30 km appears to grow during the course of the present observation. This is consistent with downward phase progression of the westerly regime of the quasi-biennial oscillation expected during this period (I. Hirota, private communication). (2) The average meridional wind is several m s^{-1} northward. Since the December meridional wind appreciably differs from the October value, a contribution from mixed Rossby-gravity waves is suggested. Such waves are known to be more prevalent in the westerly portion of the quasi-biennial oscillation (Wallace, 1973). (3) The mean vertical wind contains an upward component of approximately 1 cm s^{-1}. This is several times larger than the vertical velocities expected from mixed Rossby-gravity waves. While an offset of the radar beam from true zenith could result in horizontal wind contamination of vertical velocities, this is unlikely in view of the radio-source calibration mentioned earlier. Furthermore, the vertical structure of the observed velocities is inconsistent with contamination from the measured horizontal winds.

Temporal wind variation during the December observation is shown in Figures 3.18a-c. Each point in these figures represents

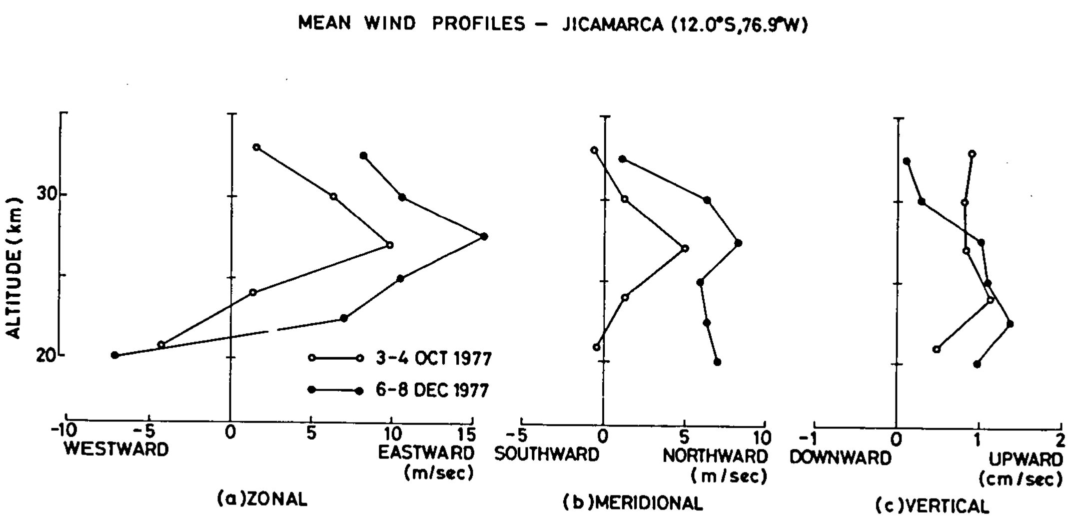

Figure 3.17. Mean wind velocities versus altitude. The circles and dots, respectively, indicate the average values observed on 3-4 October and 6-8 December 1977. (a) Zonal (eastward positive), (b) meridional (northward positive) and (c) vertical (upward positive).

a 30-minute average velocity. Diurnal tidal oscillations do not dominate the wind fields in the present observation, in contrast to the May 1974 result (Fukao et al., 1978). Both the October and December observations indicate the existence of substantial long-period waves with periods in excess of 48 hours.

One method of determining long-period components is to least-mean-square fit linear combinations of various sinusoids to the data. For the current data 24- and 12-hour sinusoids are used in conjunction with a sinusoid of period greater than 24 hours. The long-period component is assumed a priori to be monochromatic, although the possibility of the existence of several competing modes cannot be ruled out on the basis of the 24- or 48-hour observation.

The sinusoid fitting is accomplished in the following manner. Having fixed two periods at 24 and 12 hours, a third mode is fitted by changing its period successively in the range from 36 to 120 hours. The fitting is significantly improved through inclusion of a third mode. The minimum variance over the widest altitude range is achieved by the addition of a 4-5 day oscillation. This strongly suggests the presence of mixed Rossby-gravity waves. While the 1977 observation is not ideally suited to examination of waves with periods of longer than 48 hours, it is apparent that substantial oscillations other than tidal modes are present. Future observation will confirm the

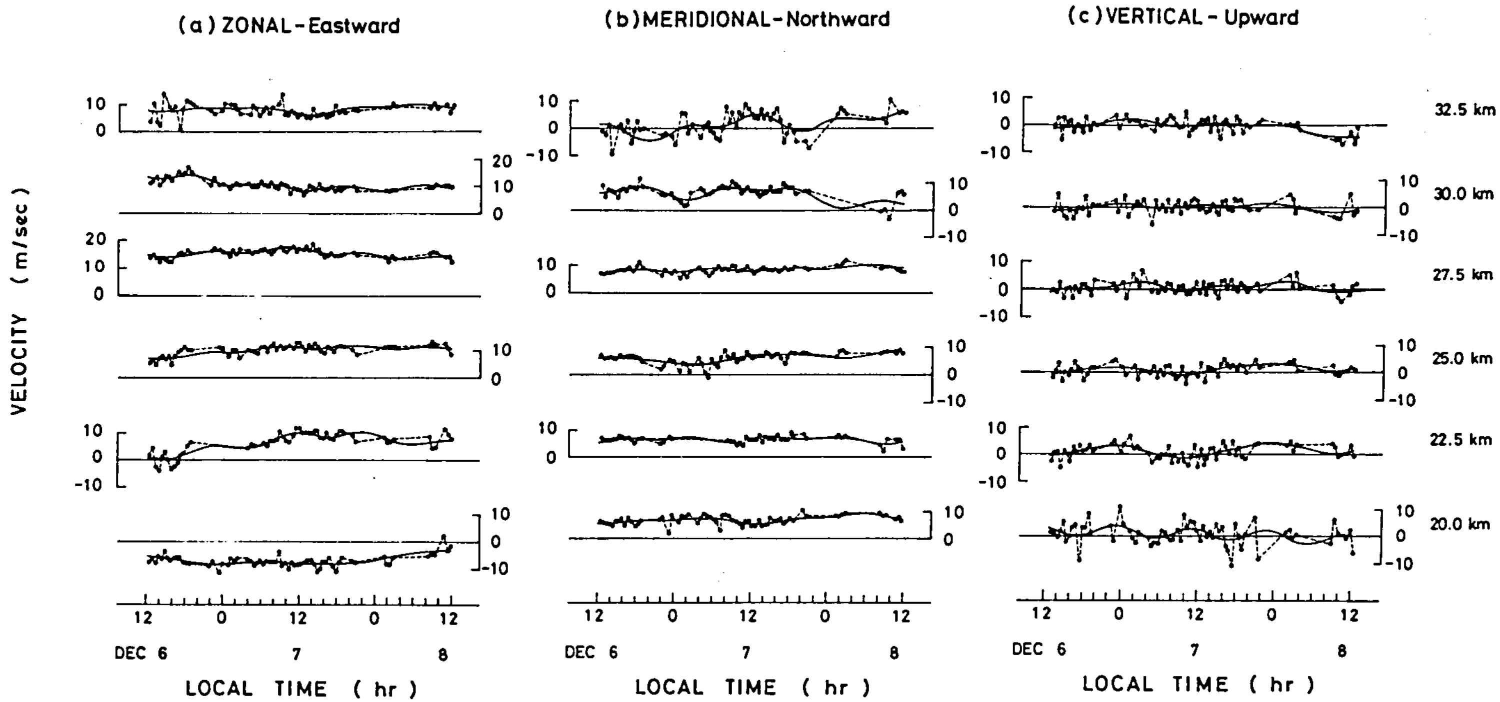

Figure 3.18. Temporal variation (broken lines) of (a) the zonal (eastward), (b) meridional (northward) and (c) vertical (upward) wind velocities observed on 6-8 December 1977. Solid lines give the combination of a 4-day period sinusoid and 24- and 12-hour period sinusoids which fits best to the data.

dominant periods by continuously measuring wind velocities for several days.

The amplitude and phase of the wave with a period which is tentatively put 4 days are shown in Figure 3.19. The phase is expressed as the time of maximum westerly counted from 00 LT on 6 December 1977. A fairly systematic variation of phase with altitude is evident, especially in the zonal and vertical components. The observed downward phase progression indicates upward flux of energy from the troposphere. Vertical wavelengths of 10-15 km are inferred from the vertical and zonal phase profiles, although the wavelength inferred from the meridional phase profile may be on the order of 5 km. The amplitude is generally a few m s^{-1} for both horizontal components and 1 cm s^{-1} for the vertical component.

The long-period component we infer is similar to mixed Rossby-gravity waves in period range as well as zonal and meridional amplitudes. It differs, however, in vertical amplitude and wavelength. This suggests that other modes may be present, and gives further impetus to future suitable observations.

3.5.3 Tidal wind oscillation

Tidal wind oscillations in and above the stratosphere have been reported from a variety of observations, although the detailed behavior exhibits considerable variation. Attempts to

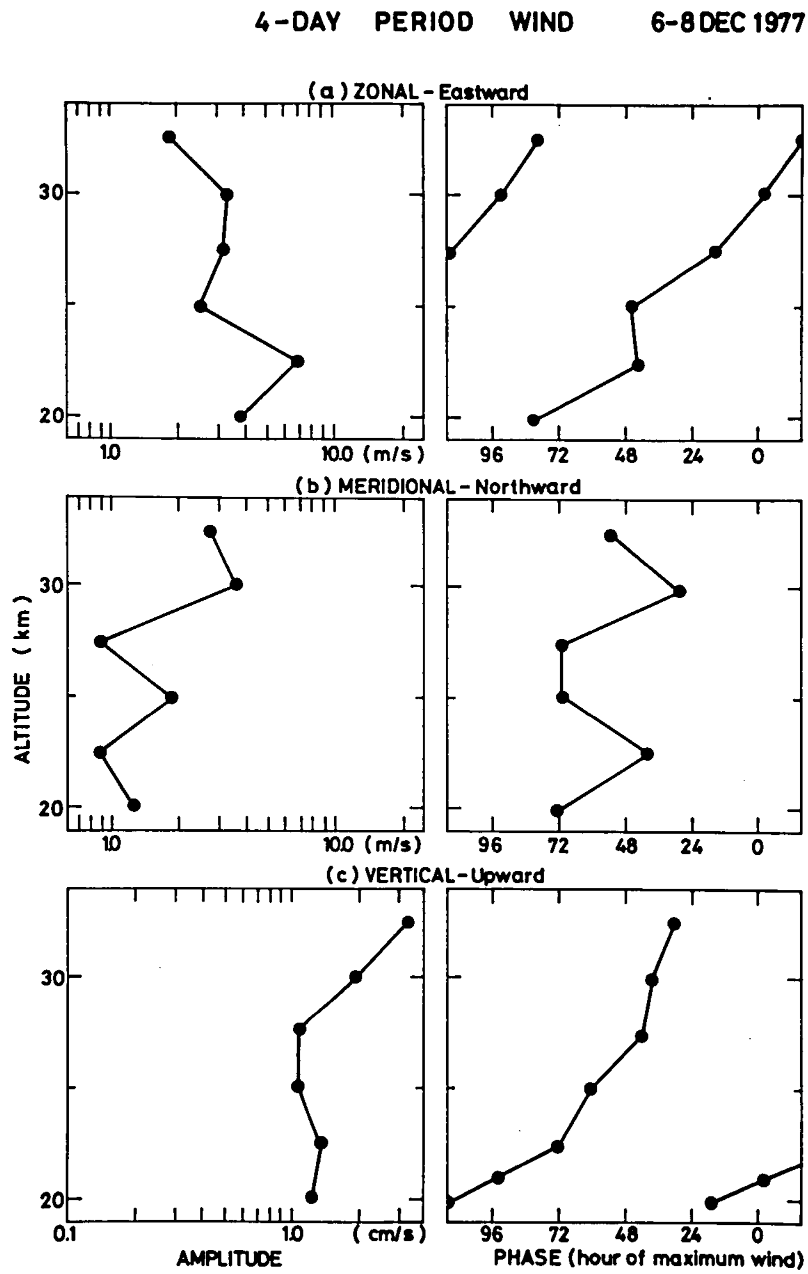

Figure 3.19. Vertical profiles of the amplitude and phase of a 4-day period wind oscillation inferred from a 48-hour observation made on 6-8 December 1977. (a) Zonal (eastward), (b) meridional (northward) and (c) vertical (upward).

compare observed tidal motions in the lower stratosphere with tidal theory are difficult due to the small amplitudes of some components and the simplifying assumptions needed to render the theory tractable.

We now examine the extent to which our results can be explained by current tidal theory. The observed amplitudes and phases are plotted in Figures 3.20 and 3.21.

A. Diurnal wind oscillation: The solid lines in Figures 3.20a-c represent theoretical solar diurnal tides determined by Lindzen (1967; Chapman and Lindzen, 1970) for an isothermal atmosphere in equinoctial conditions. The agreement between observed and theoretical amplitudes and phases of horizontal velocity is quite good considering the simplifying assumptions used in the derivation of the theory. Note the similar trends of phase with altitude. Also of interest is the predominance of the meridional over the zonal amplitude, especially in the December data. This is consistent with theoretical predictions. Finally, the diurnal wind oscillation is larger in October than in December throughout the height range observed. This indicates a substantial seasonal variation of the diurnal wind oscillation.

Figure 3.20a compares current results with equinoctial values of the zonal diurnal wind oscillation obtained in May 1974 (Fukao _et al._, 1978). Meridional and vertical components are not

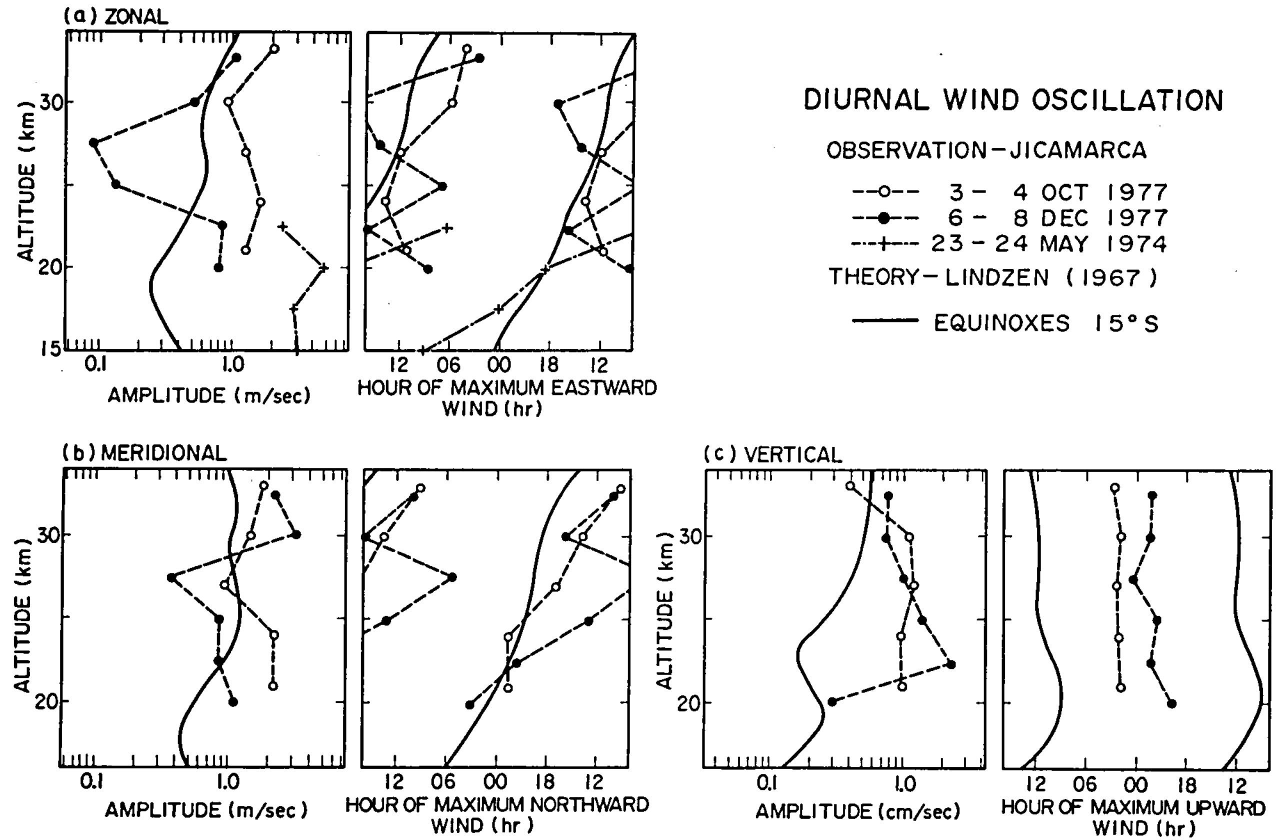

Figure 3.20. Vertical profiles of the amplitude and phase (hour of maximum wind) of the diurnal wind oscillation observed on 3-4 October and 6-8 December 1977. (a) Zonal, (b) meridional and (c) vertical. The crosses in the zonal component denote the result obtained in May 1974 (Fukao et al., 1978). Solid lines are for the theoretical values of the solar diurnal tide at 15 S for the equinoctial conditions (Lindzen, 1967).

available from the 1974 measurement, but the observed zonal values are several times larger than theoretical values. Also, a marked difference is seen in the slopes of phase as a function of altitude. The vertical wavelength deduced from the 1974 phase profile is less than 10 km, while the present October and December phase profiles yield vertical wavelengths of the order of 20 km. Thus, the diurnal wind oscillation of the current observations is most likely of solar origin, while the observed 1974 oscillation appears to be a non-migrating mode probably affected by topographic conditions as noted by Wallace and Tadd (1974).

Considerable differences between observation and theory are evident in the vertical component shown in Figure 3.20c. The observed amplitudes are almost an order of magnitude larger than theoretical values, while the observed and theoretical phases differ by approximately 12 hours. This antiphase is also seen in the vertical component of the diurnal tidal wind measured during the Diurnal Experiment of meteorological rockets in the equatorial stratosphere (Weisman and Olivero, 1979).

B. Semidiurnal wind oscillation: The theoretical values for the solar semidiurnal tide in summer and at equinoxes (Lindzen and Hong, 1974) are shown by the solid lines in Figures 3.21a-c. Unlike the case of diurnal horizontal velocity, there are noticeable differences between the observation and theory. The principal source of disagreement concerns amplitudes; the measured values of 0.5 to 1.0 m s^{-1} are several times larger than the theoretical values. The theoretically predicted node near 30 km is not observed. Of course, the 3 km height resolution of the radar observation does not permit determination of detailed structure in height profiles.

The observed prevailing tendency of the phase of semidiurnal oscillation is to remain roughly constant with height. Note that minimal phase variation with height is a fundamental property of the semidiurnal migrating tide (Lindzen and Hong, 1974). This tendency is also noted in the radiosonde data of Wallace and Tadd (1974). The downward phase progression detected by the Arecibo radar (Fukao et al., 1981b) is not noticed in the current observation.

The observed amplitude of the vertical wind semidiurnal oscillation is one order greater than theoretical values in magnitude. This result is consistent with the recent analysis of meteorological rocket data by Weisman and Olivelo (1979).

3.5.4 Comparison with rawinsonde measurements

Several wind profiles obtained during the December observation have been compared with winds determined by rawinsondes launched from the Lima-Callao airport (12.0°S, 77.1°W) on the coast some 30 km west of Jicamarca. Similar comparisons

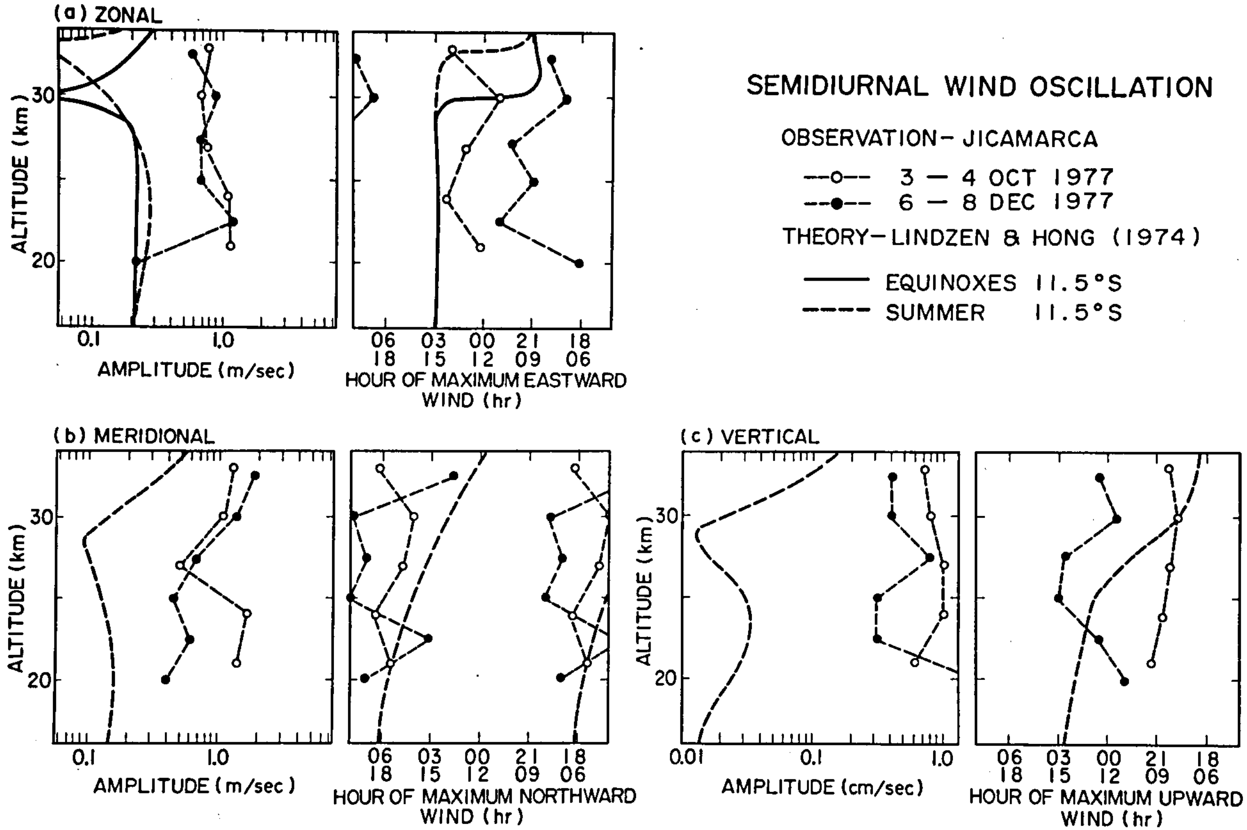

Figure 3.21. Same as Figure 3.20 but for the semidiurnal wind oscillation. Theoretical values of the solar semidiurnal tide at 11.5°S are depicted for the equinoctial and summer conditions by solid and broken lines, respectively (Lindzen and Hong, 1974).

have been performed for several VHF radars in middle and high latitudes. Warnock et al. (1978) have noted at Sunset, Colorado, that close agreement in profiles can generally be expected only in case of rawinsonde ascents quite close to the radar location. Ecklund et al. (1977) further have found good agreement over separations of more than 50 km by using the temporary Poker Flat radar. Excellent agreements were obtained even over separations as great as 100 km by the SOUSY radar (Rüster and Czechowsky, 1980). In the tropical region Fukao et al. (1978) showed that the one-day mean zonal wind in the altitude range of 15 to 22.5 km over Jicamarca did not conflict with the monthly mean value measured by rawinsonde for the same month. To our knowledge, the current observation is the first detailed comparison of simultaneous VHF radar and rawinsonde measurements in the tropical lower stratosphere.

Four comparisons are presented in Figure 3.22. In this figure the rawinsonde values have been averaged over 2 km of altitude. The balloons take approximately 60 minutes to rise to 20 km and 90 minutes to reach 30 km. Thus the radar-determined winds were measured in the 30-minute period from 60 to 90 minutes after launching the balloons. Also, included in the figure is an example of the October observation in which fragmentary radar data are available during the routine rawinsonde observation at 1830 LT. Due to prevailing easterly or northeast winds in the

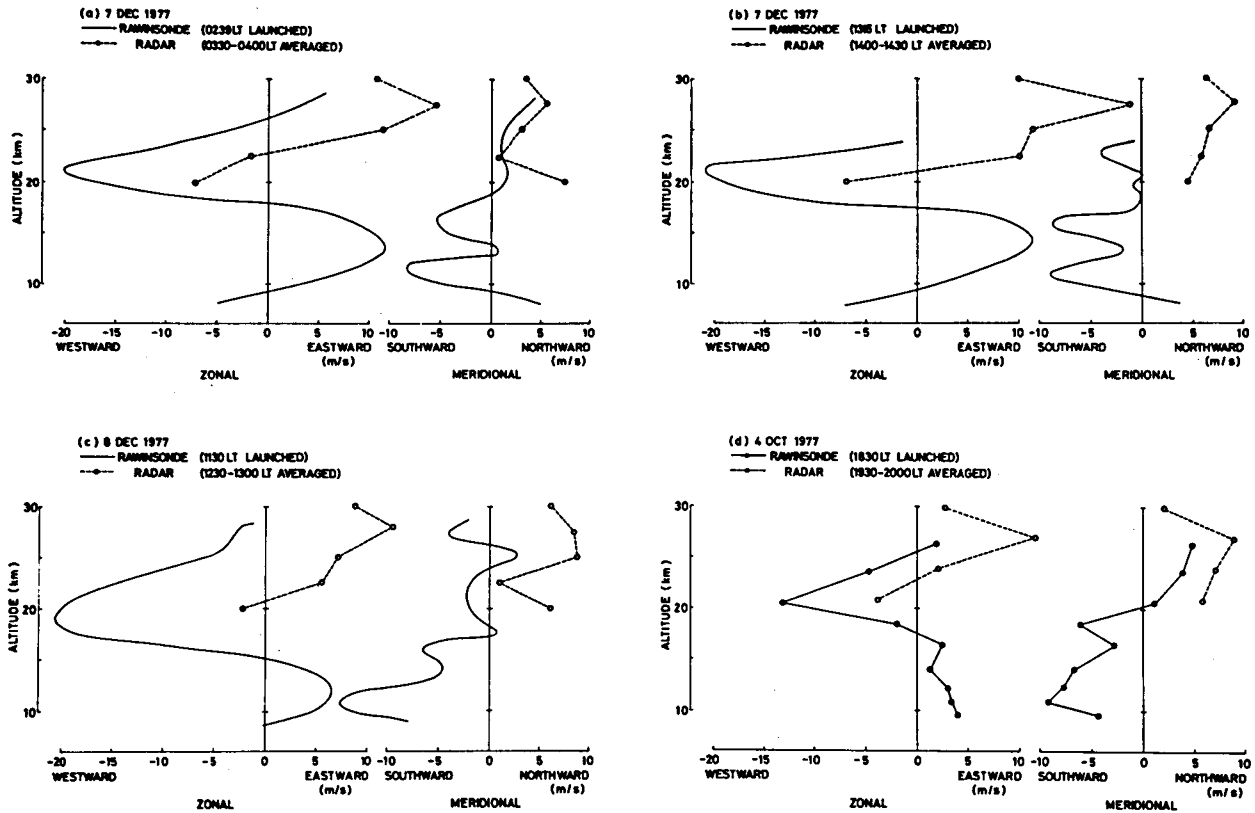

Figure 3.22. Comparison of the radar-inferred zonal and meridional winds with winds observed simultaneously by rawinsonde balloons launched from the Lima-Callao airport at (a) 0239 LT on 7 December, (b) 1315 LT on 7 December, (c) 1130 LT on 8 December and (d) 1830 LT on 4 October 1977.

troposphere the balloons drift in the opposite direction from the radar, resulting in a significant increase in the distance between the radar and the balloons at higher altitudes (see Figure 3.23 for the balloon trajectories). The separation is often several tens of kilometers at an altitude of 25 km. Furthermore, the altitude range for which both rawinsonde and radar measurements are available is limited to a few kilometers. The limitations of these observations may have unfavorable bearing on the present comparison, as discussed by Warnock et al. (1978).

It is evident from Figure 3.22 that the relationship between the radar and rawinsonde zonal wind profiles does not change significantly between the October and December observations. One noteworthy aspect of each observation is a marked shear in the zonal wind with an amplitude of several m s^{-1} per kilometer. The region of transition between westward and eastward flow is found to be 2-3 km lower in the radar-determined profiles than in the rawinsonde profiles.

The meridional wind velocity exhibits greater altitude and time variations than the zonal wind, and the radar- and rawinsonde-inferred profiles show similar tendencies with height. The radar-determined velocities are sometimes offset from the rawinsonde values by several m s^{-1}.

Fleisch (1980) also reported an unusually large discrepancy in wind profiles for the Jicamarca radar, although in some case

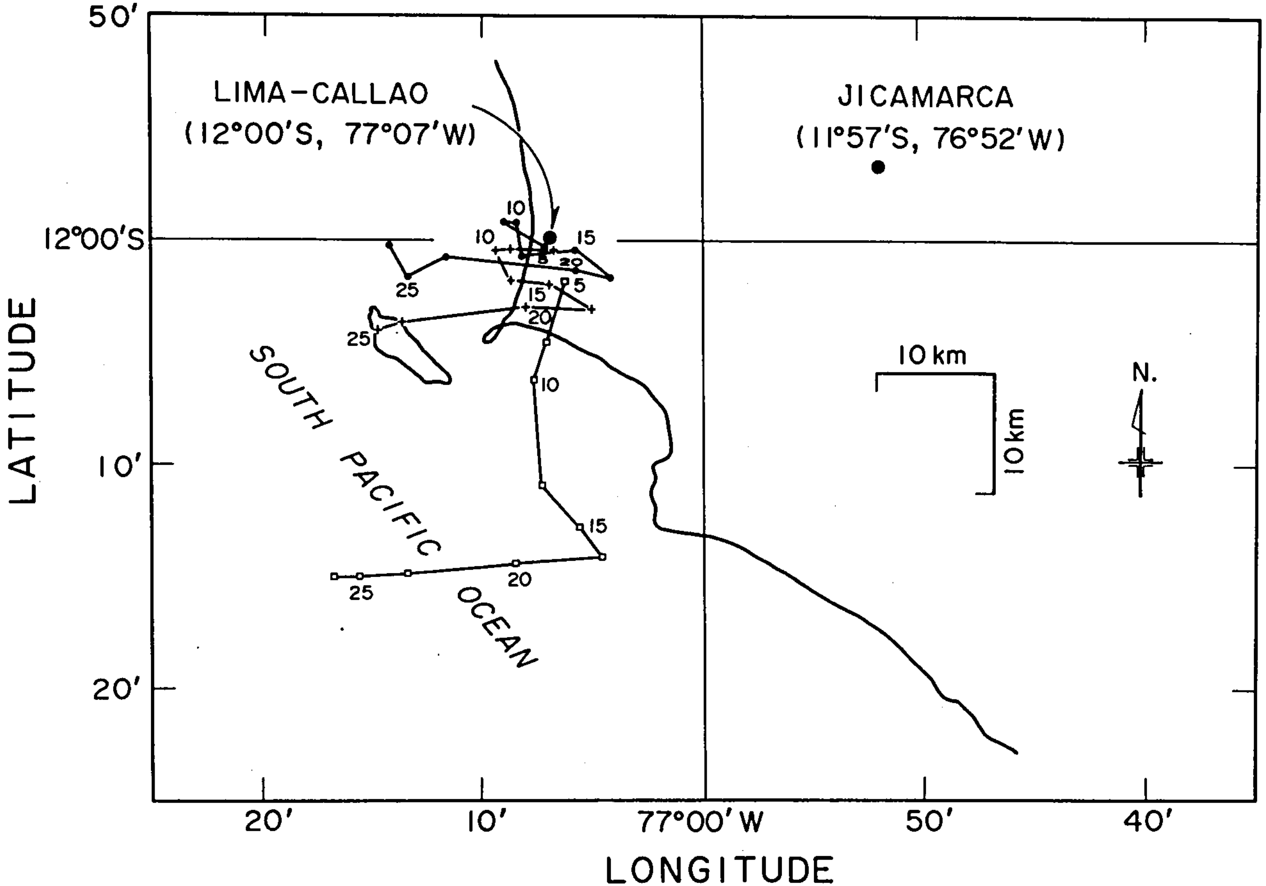

Figure 3.23. A map showing locations of the Jicamarca radar and the Lima-Callao airport, and hodographs of balloon ascents on 7-8 December 1977. Altitude is marked every 5 km along each balloon trajectory.

the correlation was fairly good. A few important possibilities need to be mentioned for the discrepancy. First, the errors associated with rawinsonde measurements become quite large above around 10 km (Records, 1975). Second, the height resolution of the present observations was about 3 km, providing a volume-averaged wind measurement. Improved altitude resolution is very important in future observations. The possibility that this discrepancy is caused by radar malfunction or errors in data reduction has been examined carefully, but this is considered unlikely.

Chapter 4.

SUMMARY AND CONCLUDING REMARKS

The main conclusions of the present work are summarized as follows;

A. Radar signal processing

[1] Formulation for radar signals backscattered from atmospheric refractive index fluctuations with the radar ambiguity function is made in order to provide a consistent description of radar resolution properties.

[2] Performance of the phase-coded pulse compression for MST measurement is studied. Complementary code is superior to the Barker code if the following condition is satisfied; the target Doppler shift ω_d be less than $0.071(2\pi)/T$ or the target spectral width ω_H be less than $0.034(2\pi)/T$ where T is the interpulse period.

[3] Multiple compressed pulse method and its performance are investigated for thermosphere measurements. Pulse compression is effective only when the condition $(\Delta h)^2 < (N/S)_o(\gamma+1)/(\gamma p)$ is satisfied where Δh is the range resolution, γ the compression

ratio and p the number of pulses. A larger number of pulses always improves the time resolution if other practical conditions permit.

[4] Widely-used periodogram of radar signals is expressed with the four-dimensional (space-time) spectral density function of anisotropic fluctuations. This defines the radar filtering function in both space and time. As a results, the effect of finite scattering volume can be extended from the conventional one-dimensional case to the three-dimensional (spatial) case. It is found that an aspect sensitivity of scattered echo power can take place even in the case of a weak refractive index fluctuation with anisotropic structures.

B. *Observational results*

[5] The depolarization properties of MST radar echoes were first measured with circular polarizations. The depolarization ratio exhibits a marked negative correlation with the echo power; the time of the correlation is about 10 min order in the mesosphere, whereas it is a few to several tens seconds in the lower stratosphere.

[6] The dominant short-period oscillations observed are largely buoyancy or Brunt-Väisälä oscillations. The dominant periodicity is about 5 min in the lower stratosphere and 11 min in the upper troposphere. These oscillations are, on the average,

convected with the mean horizontal winds.

[7] Positive correlation between the echo power and the signal correlation time is generally observed. This confirms that the echo comes from stable atmospheric structures. Around the tropopause, however, these features were not observed, suggesting the dominance of turbulent scatter.

[8] By the long-time radar measurements, long-period atmospheric waves were also observed. The amplitude and phase of the diurnal component observed match fairly well with the theoretical values of the solar diurnal migrating tide, whereas the semidiurnal component shows some discrepancies with respect to the theory. Existence of a long-period wave with a period exceeding two days was aslo indicated.

REFERENCES

Balsley, B. B., and K. S. Gage (1980), The MST radar technique: Potential for middle atmospheric studies, Pure Appl. Geophys., 118, 452-493.

Barrick, D. B. (1980), Accuracy of parameter extraction from sample-averaged sea-echo Doppler spectra, IEEE Trans. Antennas Propagat., 28, 1-10.

Bartlett, F. R. S. (1978), An introduction to stochastic processes, Cambridge University Press, London.

Beer, T. (1978), Tropical waves, Rev. Geophys. Space Phys., 16, 567-582.

Belrose, J. S. (1970), Radio wave probing by the partial reflection of radio waves (from heights below 100 km), J. Atmos. Terr. Phys., 32, 567-596.

Berkowitz, R. S. (1965), Modern radar, 565 pp., John Wiley, New York.

Bickel, S. H. (1965), Some invariant properties of the polarization scattering matrix, Proc. IEEE, 53, 1070-1072.

Bickel, S. H., and R. H. T. Bates (1965), Effects of magneto-ionic propagation on the polarization scattering matrix, Proc. IEEE, 53, 1089-1090.

Bickel, S. H., and J. F. A. Ormsby (1965), Error analysis, calibration and the polarization scattering matrix, Proc. IEEE, 53, 1087-1089.

Booker, H. G., and W. E. Gordon (1950), Theory of radio scattering in the troposphere, Proc. IRE, 38, 401-412.

Chapman, S., and R. S. Lindzen (1970), Atmospheric tides, 200 pp., D. Reidel, Dordrecht, Holland.

Cook, C. E., and M. Bernfeld (1967), Radar signals - An introduction to theory and application, Academic Press, New York.

Crane, R. K. (1976), Spectra of ionospheric scintillation, J. Geophys. Res., 81, 2041-2050.

Crane, R. K. (1977), Ionospheric scintillation, Proc. IEEE, 65, 180-199.

Crane, R. K. (1980), A review of radar observations of turbulence in the lower stratosphere, Radio Sci., 15, 177-194.

Cunnold, D. M. (1975), Vertical transport coefficients in the mesosphere obtained from radar observations, J. Atmos. Sci., 32, 2191-2200.

de Wolf, D. A. (1975), Propagation regimes for turbulent atmosphere, Radio Sci., 10, 53-57.

Deley, D. W. (1970), Waveform design, Chap. 3 of Radar Handbook, M. I. Skolnik (ed.), McGraw-Hill, New York.

Dougherty, J. P., and D. T. Farley (1960), A theory of incoherent scattering of radio waves by a plasma, Proc. Roy. Soc., A259, 79-99.

Evans, J. V. (1969), Theory and practice of ionospheric study by Thomson scatter radar, Proc. IEEE, 57, 496-530. Evans, J. V. (1975), High-power radar studies of the ionosphere, Proc. IEEE, 63, 1636-1650.

Evans, J. V. (1978), Incoherent scatter contributions to studies of the dynamics of the lower thermosphere, Rev. Geophys. Space Phys., 16, 195-216.

Fante, R. L. (1975), Electromagnetic beam propagation in turbulent media, Proc. IEEE, 63, 1669-1692.

Fante, R. L. (1980), Electromagnetic beam propagation in turbulent media: An update, Proc. IEEE, 68, 1424-1443.

Farley, D. T. (1965), Faraday rotation measurements using incoherent scatter, Radio Sci., 4, 143-152.

Farley, D. T. (1969), Incoherent scatter correlation function measurements, Radio Sci., 4, 935-953.

Farley, D. T. (1972), Multi-pulse incoherent-scatter correlation function measurements, Radio Sci., 7, 661-666.

Friend, A. W. (1949), Theory and practice of tropospheric sounding by radar, Proc. IRE, 37, 116-138.

Fukao, S., and K. Wakasugi (1976), Correlation function measurements for incoherent scatter radar, Rept. Ionos. Space Res. Japan, 30, 95-101.

Fukao, S., and K. Wakasugi (1977), Improvement in resolutions of IS radar measurements with multiple coded pulses, Trans IECE Japan, 60-B, 720-727.

Fukao, S., S. Kato, S. Yokoi, R. M. Harper, R. F. Woodman, and W. E. Gordon (1978), One full-day radar measurements of lower stratospheric winds over Jicamarca, J. Atmos. Terr. Phys., 40, 1331-1337.

Fukao, S., T. Sato, S. Kato, R. M. Harper, R. F. Woodman, and W. E. Gordon (1979), Mesospheric winds and waves over Jicamarca on May 23-24, 1974, J. Geophys. Res., 84, 4379-4386.

Fukao, S., T. Sato, I. Hirota, and S. Kato (1980a), A Preliminary radar observation of long-period waves in the tropical mesosphere over Jicamarca, J. Geophys. Res., 85, 1955-1957.

Fukao, S., T. Sato, R. M. Harper, and S. Kato (1980b), Radio wave scattering from the the tropical mesosphere observed with the Jicamarca radar, Radio Sci., 15, 447-457.

Fukao, S., K. Wakasugi, and S. Kato (1980c), Radar measurement of short-period atmospheric waves and related scattering properties at the altitude of 13-25 km over Jicamarca, Radio Sci., 15, 431-438.

Fukao, S., K. Wakasugi, and S. Kato (1980d), Depolarization properties of the mesospheric backscattering seen by a high-powered VHF radar, Trans. IECE Japan, 63-B, 825-830.

Fukao, S., S. Kato, T. Aso, M. Sasada, and T. Makihira (1980e), Middle and upper atmosphere radar (MUR) under design in Japan, Radio Sci., 15, 225-232.

Fukao, S., K. Aoki; K. Wakasugi, T. Tsuda, S. Kato, D. A. Fleisch (1981a), Some further results on the lower stratospheric winds and waves over Jicamarca, accepted J. Geophys. Res.

Fukao, S., T. Sato, N. Yamazaki, S. Kato and R. M. Harper (1981b), Radar measurement of tidal winds at stratospheric heights over Arecibo, accepted Geophys. Res. Lett.

Gage, K. S., and J. L. Green (1978), Evidence for specular reflection from monostatic VHF radar observations of the stratosphere, Radio Sci., 13, 991-1001.

Gage, K. S., and J. L. Green (1979), Tropopause detection by partial specular reflection with very-high-frequency radar, Science, 203, 1238-1240.

Golay, M. J. E. (1961), Complementary series, IRE Trans. Inf. Theory, IT-7, 82-87.

Gossard, E. E., and W. E. Hooke (1975), Waves in the Atmosphere, 456 pp., Elsevier, New York.

Graves, C. D. (1956), Radar polarization power scattering matrix, Proc. IEEE, 44, 248-252.

Hardy, K. R., and I. Katz (1969), Probing the clear atmosphere with high power, high resolution radars, Proc. IEEE, 57, 468-480.

Harper, R. M., and W. E. Gordon (1980), A review of radar studies of the middle atmosphere, Radio Sci., 15, 195-212.

Harris, F. J. (1976), On the use of windows for harmonic analysis with the descrete Fourier transformation, Proc. IEEE, 66, 51-83.

Hines, C. O. (1960), Internal atmospheric gravity waves at ionospheric heights, Can. J. Phys., 38, 1441-1481.

Ioannidis, G. A., and D. T. Farley (1974), High resolution D-region measurements at Arecibo, Radio Sci., 9, 151-157.

Ishimaru, A. (1978), Wave propagation and scattering in random media, vols. 1 and 2, Academic Press, New York.

Kato, S. (1980), Dynamics of the upper atmosphere, 233 pp., D. Reidel, Dordrecht, Holland.

Kavah, M. and G. R. Cooper, (1976), An empirical investigation of the properties of the autoregressive spectral estimator, IEEE Trans. Inf. Theory, IT-22, 313-323.

Lindzen, R. S. (1967), Thermally driven diurnal tide in the atmosphere, Quart. J. Roy. Meteorol. Soc., 93, 18-42.

Lindzen, R. S., and S.-S. Hong (1974), Effects of mean winds and horizontal temperature gradients on solar and lunar semidiurnal tides in the atmosphere, J. Atmos. Sci., 31, 1421-1466.

Liu, C. H., and K. C. Yeh (1980), Scattering of VHF and UHF radar signals from the turbulent air, Radio Sci., 15, 277-282.

Long, M. W. (1975), Radar reflectivity of land and sea, 366p pp., Lexington Books, Lexington, Mass.

Miller, K. L., S. A. Bowhill, K. P. Gibbs, and I. I. Countryman (1978), First measurements of mesospheric vertical velocities by VHF radar at temperate latitudes, Geophys. Res. Lett., 5, 939-942.

Monin, A. S., and A. M. Yaglom (1971), Statistical fluid mechanics, MIT Press, Cambridge, Mass.

Nathanson, F. E. (1969), Radar design principles, 626 pp., McGraw-Hill, New York.

Noonkester V. R. and J. H. Richter (1980), FM-CW radar sensing of the lower atmosphere, Radio Sci., 15, 337-354.

Ogura, H., and Y. Yoshida (1981), Spectral analysis and subtraction of noise in radar signals, IEEE Trans. Aerosp. & Electron. Syst., AES-17, 62-71.

Papoulis, A. (1977), Signal analysis, 431 pp., McGraw-Hill, New York.

Plobert-Jones, J. R. (1962), The radar equation in meteorology, Quart. J. Roy. Meteorol. Soc., 88, 485-495.

Rihaczek, A. W. (1964), Radar resolution properties of pulse trains, Proc. IEEE, 52, 164-153.

Rihaczek, A. W. (1965), Radar signal design for target resolution, Proc. IEEE, 53, 116-128.

Rihaczek, A. W. (1969), Principles of High-resolution radar, 498 pp., McGraw-Hill, New York.

Rihaczek, A. W. (1971), Radar waveform selection-A simplified approach, IEEE Trans. Aerosp. & Electron. Syst., AES-6, 1078-1086.

Rihaczek, A. W., and R. M. Golden (1971), Range sidelobe suppression for Barker codes, IEEE Trans. Aerosp. & Electron. Syst., AES-7, 1087-1092.

Röttger, J., and C. H. Liu (1978), Partial reflection and scattering of VHF radar signals from the clear atmosphere, Geophys. Res. Lett., 5, 357-360.

Röttger, J., and R. A. Vincent (1978), VHF radar studies of tropospheric velocities and irregularities using spaced antenna technique, Geophys. Res. Lett., 5, 917-920.

Röttger, J., P. K. Rastogi, and R. F. Woodman (1979), High-resolution VHF radar observations of turbulence structures in the mesosphere, Geophys. Res. Lett., 6, 617-620.

Rüster,R. and R. F. Woodman (1976), Radar-measurements in the tropo-, strato- and mesosphere, Proceedings of the 17th radar meteorological conference, 354-358.

Rüster,R., J. Röttger, and R. A. Vincent (1978), Radar measurements of waves in the lower stratosphere, Geophys. Res. Lett., 5, 119-122.

Rüster, R. and J. Klostermeyer (1980), Radar measurements of waves during a jet stream passage, Geophys. Res. Lett., 7.

Skolnik, M. I. (1980), Introduction to radar system, 581 pp., McGraw-Hill, New York.

Tatarskii, V. I. (1971), The effect of turbulent atmosphere on wave propagation, National Technical Information Service, Springfield, Va.

Tennekes, H., and J. L. Lumley (1972), A first course in turbulence, 300 pp., MIT Press, Cambridge, Mass.

Ulrych, T. J. and T. N. Bishop (1975), Maximum-entropy spectral analysis and autoregressive decomposition, Rev. Geophys. Space Sci., 13, 183-220.

Valley, G. C. (1975), Backscattering of wideband signals from turbulent slabs, Radio Sci., 10, 453-459.

VanZandt, T. E., J. L. Green, K. S. Gage and W. L. Clark (1978), Vertical profiles of refractivity turbulence structure constant: Comparison of observations by the Sunset radar with a new theoretical model, Radio Sci., 13, 819-829.

VanZandt, T. E., J. L. Green, and W. L. Clark (1979), Buoyancy waves in the troposphere: Doppler radar observations and a theoretical model, Geophys. Res. Lett., 6, 429-432.

Vincent, R. A., and J. Röttger (1980), Spaced antenna VHF radar observations of tropospheric velocities and irregularities, Radio Sci., 15, 319-336.

Wakasugi, K., S. Fukao, and S. Kato (1980), Depolarization of a 50-MHz radio wave backscattered from the middle atmosphere, Radio Sci., 15, 439-446.

Wallace, J. M. (1973), General circulation of the tropical lower stratosphere, Rev. Geophys. Space Phys., 11, 191-222.

Wallace, J. M., and R. F. Tadd (1974), Some further results concerning the vertical structure of atmospheric tidal motions within the lowest 30 km, Mon. Weather Rev., 102, 795-803.

Wheelon, A. D. (1972), Backscattering by turbulent irregularities: A new analytical description, Proc. IEEE, 60, 252-265.

Woodman, R. F., and A. Guillén (1974), Radar observation of winds and turbulence in the stratosphere and mesosphere, J. Atmos. Sci., 31, 493-505.

Yeh, K. C., and C. H. Liu (1974), Acoustic-gravity waves in the upper atmosphere, Rev. Geophys. Space Phys., 12, 193-216.

Zamlutti, C. J., and D. T. Farley (1975), Incoherent scatter multi-pulse measurements, Radio Sci., 10, 573-580.

Zamlutti, C. J. (1980), Design of Barker coded multiple pulse experiments, J. Atmos. Terr. Phys., 42, 975-982.

Reference is also made to the following unpublished material:

Fleisch D. A. (1976), Stratospheric scattering of radio waves and the Jicamarca radio telescope, M. S. Dissertation, Rice University.

Fleisch D. A. (1980), Jicamarca radar measurements of winds and turbulence in the stratosphere, Ph.D. Dissertation, Rice University.

Ochs, G. R. (1965), The large 50 Mc/s dipole array at Jicamarca radar observatory, Rept. 8772, National Bur. of Stand., Boulder, Colo.

Records, W. L. (1974), FOF rawinsonde observation activities, Atmospheric Technology, NCAR, Boulder, Colorado.